5-1-2012

Deciphering the Evolution of Ore Fluids at The Batu Hijau Copper-~Gold Porphyry Deposit, Sumbawa, Indonesia

Jordan Thomas Armstrong
University of Nevada, Las Vegas, jarmstrong108@gmail.com

Repository Citation

DECIPHERING THE EVOLUTION OF ORE FLUIDS AT THE BATU HIJAU COPPER-

GOLD PORPHYRY DEPOSIT, SUMBAWA, INDONESIA

by

Jordan Thomas Armstrong

Bachelor of Science
Auburn University
2008

A dissertation submitted in partial fulfillment
of the requirements for the

Master of Science in Geoscience

Department of Geoscience
College of Sciences
The Graduate College

University of Nevada, Las Vegas
May 2012

We recommend the thesis prepared under our supervision by

Jordan Thomas Armstrong

entitled

Deciphering the Evolution of Ore Fluids at the Batu Hijau Copper-Gold Porphyry Deposit, Sumbawa, Indonesia

be accepted in partial fulfillment of the requirements for the degree of

Master of Science in Geoscience
Department of Geoscience

Jean Cline, Committee Chair

Adam Simon, Committee Member

Rodney V. Metcalf, Committee Member

Barbara Luke, Graduate College Representative

Ronald Smith, Ph. D., Vice President for Research and Graduate Studies
and Dean of the Graduate College

May 2012

ABSTRACT

**Deciphering the Evolution of Ore Fluids at the Batu Hijau Copper-Gold
Porphyry Deposit, Sumbawa, Indonesia**

by

Jordan Armstrong

Dr. Jean S. Cline, Examination Committee Chair
Professor of Geology
University of Nevada, Las Vegas

Fluid inclusions contained within quartz veins from the Batu Hijau Cu-Au porphyry deposit in Indonesia were analyzed to track the evolution of fluid temperature, pressure, and composition during the formation of the deposit to better understand the formation of this and other Cu-Au porphyry deposits in order aid future exploration. A combination of petrography, microthermometry, synchrotron x-ray fluorescence, and laser ablation-inductively coupled plasma-mass spectrometry were used to determine the temperature, pressure, and compositional aspects of the deposit.

Four types of fluid inclusions were recognized at Batu Hijau based on the volume percent of the vapor bubble; inclusions were classified as VB35, VB20H, VB60, and VB85 type inclusions. A high temperature, non-reactive fluid trapped in VB60 inclusions was introduced to the system first, was associated with only minor ore mineral precipitation, and was likely linked to high temperature alteration. A second, lower temperature, highly reactive fluid trapped in VB35 inclusions was then introduced to the system and was likely responsible for the majority of ore mineral precipitation as well as lower temperature alteration assemblages. This

second fluid became immiscible during its ascent to the surface, forming a highly reactive brine and a non-reactive vapor, trapped in VB20H and VB85 inclusions, respectively.

While these two fluids seem temporally distinct, future studies investigating the exact timing of ore fluid introduction, and the association of ore fluids pulses to magmatic intrusions is required to full understand the temporal relationships of fluids at Batu Hijau. If fluid inclusions can be petrographically linked to distinct intrusion events, a complete four-dimensional model for fluid evolution can be completed, providing a valuable new tool to aid in the exploration of Cu-Au porphyry deposits.

ACKNOWLEDGMENTS

TABLE OF CONTENTS

LIST OF TABLES

LIST OF FIGURES

CHAPTER 1

INTRODUCTION

The Batu Hijau porphyry Cu-Au deposit is a world-class island arc type porphyry deposit, located on the southwestern portion of Sumbawa Island, Nusa Tenggara Barat Province, Indonesia. This 12 km by 6 km district contains an estimated 914 million tonnes of ore at an average grade of 0.53% Cu and 0.40 g/t Au (Garwin, 2002; Arif and Baker, 2004), and is one of the largest and richest porphyry Cu-Au deposits in Asia.

Ore fluids produced distinct quartz ± sulfide veins and veinlets that cross cut the tonalite intrusions and their surrounding host rocks. Within these veins, fluid inclusions trapped in quartz contain ore fluids, which represent fluids moving through the deposit during the time of its formation. The ore fluids in the fluid inclusions are key to defining the temperature and pressure conditions under which the deposit formed, and defining the geochemistry of the hydrothermal system, which was responsible for the distribution Cu and Au within the deposit.

Preliminary fluid inclusion studies have suggested that deposit formation temperatures ranged from 280 to over 700 °C. Based on the coexistence of magnetite-bornite ± chalcocite, Garwin (2000) suggested that the earliest veins at Batu Hijau likely formed at > 500–700 °C (cf. Simon *et al.*, 2000). A preliminary fluid inclusion study by Garwin (2000) on inclusions in halite-bearing transitional veins produced homogenization temperatures that ranged from about 450 to 500 °C. These temperatures are consistent with phase equilibria temperature estimates based on a chalcopyrite ± bornite vein mineralogy (Simon *et al.*, 2000).

1

Homogenization temperatures of < 400 °C were obtained by Garwin (2000) for late pyrite-bearing veins. A fluid inclusion study conducted by Imai and Ohno (2005) documented homogenization temperatures ranging from 280 to 454 °C, significantly lower than temperatures obtained by Garwin (2000). This temperature is similar to Au saturation temperatures for bornite (~300 °C) and chalcopyrite (250 °C) (Kesler *et al.*, 2002; Arif & Baker, 2004).

A detailed fluid inclusion microthermometry study to clarify processes of ore formation is warranted. Microthermometric data on well-characterized fluid inclusions with appropriate pressure corrections can provide the temperatures and pressures at which the deposit formed. Additional qualitative and quantitative data from synchrotron x-ray fluorescence (SXRF) and laser ablation inductively coupled plasma mass spectrometry (LA-ICP-MS), respectively, can document and quantify major and trace element concentrations. Such data will contribute to a model describing the transport of metals by hydrothermal fluids, and the precipitation of Cu- and Au-bearing minerals.

CHAPTER 2

GEOLOGIC BACKGROUND

The island of Sumbawa, situated adjacent to the margin of the Sunda continental shelf and lying within the Sunda-Banda magmatic arc (Figure 1), is comprised of an Early Miocene to Holocene volcanic arc complex overlying approximately 14 to 23 km of oceanic crust (Hamilton, 1979; Barberi *et al.*, 1987). The southwestern portion of Sumbawa Island, where Batu Hijau is located (Figure 2), is comprised of Early Tertiary, low-K, calc-alkaline to weakly alkaline andesitic volcanic and volcaniclastic rocks (Clode *et al.*, 1999). These include andesitic tuff, breccia, fine-grained volcaniclastic sandstones and mudstones, and porphyritic andesite that make up the pre-mineralization rocks of the Batu Hijau district. This andesitic volcaniclastic rock succession was intruded by at least three distinct hypabyssal andesites, at least four equigranular quartz diorite plutons, and three successive tonalite intrusions, which formed the dike and stock complex that forms the core of the Batu Hijau Cu-Au deposit (Clode *et al.*, 1999; Garwin, 2002). Figure 3 shows a cross-section through the core of the Batu Hijau deposit; rock units in this figure, and all subsequent figures, are simplified, and the various andesitic and dioritic units are not differentiated. Clode *et al.* (1999) identified three tonalite intrusions: the Old Tonalite, Intermediate Tonalite, and Young Tonalite based on their relative ages to one another from cross-cutting relationships. These tonalite porphyry stocks were emplaced at the contact between the quartz diorite and andesitic volcaniclastic succession (Clode *et al.*, 1999). The emplacement of Intermediate and Young Tonalite destroyed and over-printed most of what may

3

have been Old Tonalite. Only small remnants of Old Tonalite, situated around the edges of the Intermediate Tonalite intrusion, remain, and are not large enough to appear in Figure 3 and all subsequent figures. Emplacement of the tonalite porphyry complex was rapid, with the three tonalite pulses occurring between 3.76 ± 0.12 Ma to 3.67 ± 0.10 Ma, as dated on zircons using U-Pb SHRIMP dating (Fletcher *et al.*, 2000; Garwin, 2000).

Clode *et al.* (1999) and Garwin (2000; 2002) hypothesized that most mineralization is genetically related to the Old and Intermediate Tonalites, with the majority of mineralization associated with ore fluids derived from the Old Tonalite. Higher Cu and Au grades, commonly > 1% Cu and > 1.0 g/t Au, are spatially associated with the Old Tonalite and its adjacent host rocks (Clode *et al.*, 1999). Copper and Au grades decrease in the bulk of the Intermediate Tonalite and its surrounding host rock (<1% Cu and <1.0 g/t Au), and very low grades are present in the Young Tonalite (<0.3% Cu and <0.5 g/t Au) (Clode *et al.*, 1999). A strong positive correlation exists between quartz vein density and Cu and Au grades, with the highest vein density being associated with the Old Tonalite (Clode *et al.*, 1999).

Hydrothermal alteration and mineralization of the tonalite porphyry complex and surrounding host rocks formed during five distinct stages termed Early, Transitional, Late, Very Late, and Zeolite (Mitchell *et al.*, 1998). Early alteration and mineralization are related to the intrusion of all tonalites (Clode *et al.*, 1999), while transitional and later stages of alteration and mineralization postdate the tonalite intrusions and overprint earlier alteration and mineralization (Clode *et al.*, 1999).

Hydrothermal alteration assemblages at Batu Hijau are characteristic of porphyry Cu-Au deposits in island arcs (Sillitoe, 1990). A central potassic alteration zone formed by prograde hydrothermal activity grades outward into a zone of extensive propylitic alteration (Meldrum *et al.*, 1994). Widespread fracture-controlled intermediate argillic alteration containing chlorite, and phyllic alteration without chlorite, variably overprinted this prograde alteration envelope. Retrograde alteration is characterized by sericite (Meldrum *et al.*, 1994). A late sodic alteration assemblage has been identified overprinting earlier potassic, propylitic, intermediate argillic, and phyllic alteration in drill core (Meldrum *et al.*, 1994). At the surface, argillic and advanced argillic alteration are present (Meldrum *et al.*, 1994).

Four main categories of quartz veins, A, B, C, and D veins, are present at Batu Hijau (Clode *et al.*, 1999). Formed during the early alteration stage, A veins are typically thin (less than 1 cm thick), have irregular edges rather than straight, are composed of fine-grained granular quartz, are typically not banded, and lack a center-line (Figure 4a). Included within with the "A" family of veins are AB veins that are slightly thicker, up to 2 cm. AB veins represent a transition to B veins that contain a bornite ± chalcopyrite-filled centerline (Clode *et al.*, 1999) (Figure 4b). Formed throughout the transitional alteration stage, B veins are associated with lower Cu-Au grades than the A veins (Clode *et al.*, 1999). B veins are typically near 2 cm in thickness and have vuggy centerlines occupied by chalcopyrite and bornite (Clode *et al.*, 1999) (Figure 4c). B veins commonly have a banded texture and are characterized by the inward growth of coarse quartz crystals with euhedral crystal

faces toward the centerline of the vein (Clode *et al.*, 1999). C veins also formed during transitional alteration stages, and are typically thin and completely composed of chalcopyrite ± bornite (Clode *et al.*, 1999). D veins contain abundant coarse pyrite and lesser quartz (Arif & Baker, 2004), are related to late stage alteration, and are generally 0.5–2 cm thick (Clode *et al.*, 1999) (Figure 4d). D veins are readily identified by their large size and extensive orange and yellow oxidized feldspar alteration halos.

CHAPTER 3

METHODS

<u>Sample Selection</u>

During two field seasons at the Batu Hijau mine, 186 samples were collected from drill core spanning 14 drill holes. A majority of samples (157) were collected from drill core referenced to an East-West oriented cross section (090°). An additional 13 and 16 samples were collected from drill core referenced to radial cross sections orientated at 040° and 080°, respectively.

Sampling was aided by Newmont drill logs, and aimed at providing samples of the Old, Intermediate, and Young Tonalites, along with their surrounding host rocks from across the deposit. Lithologic contacts between tonalite units were a priority during sampling, as were samples of various vein types including A, AB, B, C, and D veins. Attention focused on localities that displayed high quartz vein density, increasing the likelihood of crosscutting vein relationships. Sampling also focused on areas with high Cu and Au assay values, and areas that displayed diversity in Cu-Fe sulfide minerals.

Specific areas targeted for sampling, identified by mine geologists, included the 'barren core', the 'western flank', and the 'central porphyry zone'. The 'barren core' is the deep, central portion of the intrusive complex, mostly comprised of the Intermediate Tonalite. It has been hypothesized that this location could provide fluid inclusions that sampled "parental" ore fluids based on the proximity to the underlying magma chamber that sits below the deposit. The 'barren core' at Batu Hijau generally contains low Cu and Au, and ore fluids that traveled through this

region are though to have transported metals. If correct, fluid inclusions from this region would provide data on the deepest available ore fluids and a baseline to evaluate fluid evolution across the system.

The 'western flank' was of interest due to its unusually high Au/Cu ratios. Au/Cu ratios of three-to-one (ppm Au/weight percent Cu) are commonplace in this region, whereas one-to-one Au/Cu ratios are present in the remainder of the deposit. The 'western flank' was primarily sampled above and surrounding the 'barren core', where Au and Cu grades begin to increase.

The 'central porphyry zone' is the part of the deposit that comprises the majority of the economic deposit in the mid and shallow levels of the deposit, and refers to the remainder of the deposit not occupied by the two previously mentioned sampling areas. It was sampled vertically and horizontally to obtain samples that could provide a three dimensional view of ore fluids across the system. Sample locations ranged from deep in the system, just above the 'barren core', to shallow samples within 100 meters of the paleosurface.

Samples selected from drill core were halved, described, and photographed at the mine site. Samples were labeled with drill hole number, footage, and Au and Cu grades obtained from drill logs.

Macroscopic & Microscopic Petrography

Core samples were examined to identify samples that could provide fluid inclusions and fluid inclusion assemblages to determine ore fluid evolution within the system. To accurately identify ore minerals, fluid inclusion assemblages, and

vein types, doubly polished thick sections were prepared from 53 samples. Samples that showed vein truncations at lithologic contacts or cross cutting vein relationships or that showed any other relevant textural features were preferred. Transmitted and reflected light microscopy were conducted on Nikon Optiphot and Olympus BX60 polarized light microscopes.

Vein relationships were further examined with the aid of microscopy, allowing vein types to be described in detail, and the nature of cross cutting relationships to be determined. Cathodoluminescence (CL) was not used in this study as previous attempts to identify different generations of quartz using this technique identified only a single CL signal (J. Cline, Personal Communication, 2009). Previously described mineral assemblages and vein characteristics (Proffett, 1998; Clode *et al.*, 1999) were used to accurately identify previously described vein types and sub-types. Quartz structures and textures, such as the orientation of quartz crystal growth in vein, along with the law of superposition and vein offsets were used to determine vein paragenesis and the nature of crosscutting relationships.

<center>Fluid Inclusion Petrography</center>

Fluid inclusions contain small samples of an ancient hydrothermal system. By analyzing fluid inclusions across a hydrothermal system, changes in temperature, pressure, and composition through time and space can be tracked.

Most inclusions selected for analyses comprise fluid inclusions assemblages (FIAs), which trapped a hydrothermal fluid at the same time, and approximately the

same pressure and temperature conditions. Inclusions that comprise FIAs have consistent phase relationships, should homogenize at about the same temperature, and should provide consistent compositional and salinity data (Goldstein & Reynolds, 1994). Assemblages were identified as primary (P), secondary (S), and pseudo-secondary (PS) based on the classification of Roedder (1984), Bodnar et al. (1985), and Goldstein & Reynolds (1994), or unknown (U) (J. Cline, Personal Communication, 2011). Primary FIAs formed during the precipitation of the host mineral contain fluids that precipitated the host mineral, and can be identified by their presence within mineral growth zones (Goldstein & Reynolds, 1994). FIAs that trapped fluids within healed microfractures or deformation structures are referred to as secondary (Goldstein & Reynolds, 1994). Secondary FIAs crosscut some or all mineral growth zones and are characterized by a curvi-planar morphology (Goldstein & Reynolds, 1994). Pseudo-secondary FIAs are those that share a similar morphology with secondary FIAs, but are truncated at a growth zone in the host mineral crystal (Goldstein & Reynolds, 1994). Unknown FIAs are those for which an origin cannot be determined (J. Cline, Personal Communication, 2011). In addition to FIAs, a limited number of isolated, non-FIA inclusions were selected for SXRF analyses.

Individual fluid inclusions and fluid inclusion assemblages were categorized and labeled based on their relative liquid to vapor ratios, and labels indicate the approximate volume percent occupied by the vapor bubble on a scale of 0 to 100%. Other inclusion characteristics noted during petrography include: the presence or absence of halite or other translucent daughter crystals, the presence or absence of

opaque daughter crystals and their abundance, the size of inclusions measured parallel to their longest dimension, and the vein type containing the inclusion. Fluid inclusion and FIA locations were photographed and described.

Fluid inclusions analyzed by LA-ICP-MS or SXRF had to meet additional analytical requirements. Inclusions were required to be 10 μm or larger along their longest dimension. Shallow inclusions were also necessary for both SXRF and LA-ICP-MS analyses. For SXRF analyses, inclusions chosen were generally within 5–12 μm of the thick section surface, and rarely exceeded a depth of 15 μm. Inclusions selected for LA-ICP-MS analyses were generally 5–15 μm deep, and fluid inclusion depth never exceeded the longest measured dimension of the inclusion.   Inclusions large enough for SXRF analyses tended to be single isolated inclusions, usually of unknown origin, and rarely of secondary origin.   The host mineral crystal surrounding the inclusion was required to be free of other fluid or mineral inclusions that would obstruct data collection. Inclusions that appeared to be necked or show any other indications of post-entrapment deformation or disturbance were avoided. Fluid inclusions selected for LA-ICP-MS analyses were always part of a fluid inclusion assemblage.

Also important to the interpretation of fluid inclusions data are the spatial relationships of analyzed inclusions to the hydrothermal system. Targeted fluid inclusions represent a multi-dimensional volume within the deposit ranging from deep to shallow, and laterally across the system.

Microthermometry

Microthermometry was employed on a total of 324 inclusions to determine homogenization temperatures and salinities, and minimum trapping temperatures were calculated for individual fluid inclusions and fluid inclusion assemblages. Heating and freezing measurements were preformed on a Linkam THMSG 600 heating and freezing stage on an Olympus BX60 petrographic microscope, controlled via Linksys32 software. Freezing analyses were performed first, and observations were made on multiple fluid inclusions simultaneously, noting final ice melting temperature, clathrate melting temperature, and hydro halite melting temperature.   Ice melting temperatures (Tm) to 0.1 °C were collected by cycling in order to assure complete ice melting.   Samples were then heated in 10 °C incremental steps to determine homogenization temperatures.   Halite melting temperatures (Tm_H) were also collected.

To preserve fluid inclusion integrity for later LA-ICP-MS analysis, inclusions were generally not heated above 500° C, as inclusions tended to decrepitate above 475° C. Vapor-rich inclusions were heated incrementally until a liquid phase was no longer visible within the inclusion; these temperatures represent a minimum homogenization temperature for all vapor-rich inclusions as exact temperatures of homogenization to vapor cannot be accurate determined (Sterner, 1992).

Synchrotron X-Ray Diffraction (SXRF)

SXRF analyses were conducted at Beamline L at the Hamburger Synchrotronstrahlungslabor (HASYLAB) at Deutsches Elektronen-Synchrotron

(DESY), Hamburg, Germany by Dr. Karen Appel.   A 4.5 GeV positron beam was deflected by a magnet with a 12.12 m bending magnet and provides a continuous spectrum with a critical energy of 16.6 KeV. For the measurements, 30.5 KeV was selected with a double multilayer monochromator for the first measurements; detection was accomplished by the use of a Si (Li) detector. With this set-up, elements with atomic number up to 51 can be detected via K-shell excitation, while lighter elements are detected by L-shell excitation. As not much information was gained from elements with atomic number between 51 and 39, energies were changed to 17 KeV in the next step thus allowing detection of elements with Z up to 38 via K-shell excitation. This set up employed a silicon drift detector, which can process higher count rates and is optimized for energies below 20 KeV, thus enabling faster measurements.

The spot size diameter of the incident photon beam was either 5 μm^2 or 15 μm^2. Step sizes of the elemental mappings were adjusted to the spot size and were 5 μm^2 and 10 μm^2, respectively (Appel, personal communication, 2011). Pixel size was 10 square micrometers for all inclusions. Analytical times between 15 and 60 seconds per point were used, and the number of points was determined by the fluid inclusion size and the resolution of the beam (Rickers, 2006). To ensure that the entire fluid inclusion was included in each measurement, an exaggeration factor of at least 3-4 times horizontally and at least 2-2.5 times vertically beyond the fluid inclusion was used (Rickers, 2006). Elemental distribution maps were aligned with a photomicrograph of each analyzed fluid inclusion to better display the distribution of an element within a single fluid inclusion.

<u>Laser Ablation–Inductively Coupled Plasma–Mass Spectrometry (LA-ICP-MS)</u>

The primary tool used to quantify the composition of fluid inclusions was laser ablation-inductively coupled plasma-mass spectrometry. LA-ICP-MS analyses were conducted at the Fluids Research Lab at Virginia Tech University using an Agilent 7500ce quadrupole ICP-MS coupled with a Geolas ArF 193nm Eximer laser ablation system; see Table 1 for complete LA-ICP-MS instrument and data parameters. Transport of ablated material was accomplished with a helium carrier gas. A total of 225 fluid inclusions from 46 fluid inclusion assemblages were ablated and analyzed. Included were 16 individual inclusions previously analyzed by SXRF.

The analytical setup and procedures used are summarized in Figure 5 (Heinrich *et al.*, 2003). Two to five sample chips and NIST610 glass were loaded into a fast purge ablation cell and the system was pumped down. The helium background signal was measured for approximately 60 seconds prior to 40-60 seconds of ablation of NIST standard glass; this process was completed twice prior to the first fluid inclusion ablation. Drilling of the sample began with a small beam size (typically 10 μm), and the beam size was stepped up to the maximum fluid inclusion dimension. The signal was monitored in real time and ablation continued until the entire contents of the inclusion were ablated and analysis of the inclusion was completed. Upon ablation of the last fluid inclusion, analysis of NIST610 glass was repeated to correct for instrument drift.

Data reduction was completed using AMS software. Element signals were integrated from the first element peaks until the signal for Na dropped below the signal for K or the next most abundant element.

CHAPTER 4

PETROGRAPHIC STUDY

Fluid Inclusion Origins

The selection of fluid inclusions for microthermometric, SXRF, and LA-ICP-MS analyses relied on the accurate classification of the origin of fluid inclusion assemblages (FIAs).   All four FIA types, primary inclusions in growth zones, secondary inclusions in healed fractures, pseudo-secondary inclusions in healed fractures terminating at a grown zone, and unknown inclusions with no clear textural features, were identified in quartz veins.

Primary FIAs were surprisingly abundant throughout the deposit and are found in nearly all samples. However, all primary assemblages contained inclusions < 3 μm in size, which were too small for accurate identification of inclusion phases, and observation of phase changes during microthermometric measurements was not possible.   Due to their small size, no primary FIAs were analyzed during this study.

The majority of FIAs identified within the deposit were secondary in origin. Due to abundant fracturing during the formation of porphyry type deposits, healed fractures containing secondary FIAs are common.   Secondary FIAs are present throughout the deposit, and show no bias with respect to location.

Pseudo-secondary FIAs at Batu Hijau were rarely identified, and they were not observed at depths below 850 meters. The lack of definitive growth zones in quartz made identifying pseudo-secondary FIAs difficult.   No observed pseudo-secondary FIA contained inclusions large enough for analyses.

Due to the complex three-dimensional distribution of fluid inclusions, the vast majority of fluid inclusions at Batu Hijau are of unknown origin. Single, isolated inclusions are common in addition to inclusion pairs and small groups of inclusions; the complex three-dimensional distribution of abundant fluid inclusions added to the ambiguity of the origin of many inclusions.

Fluid Inclusion Types

Fluid inclusions and FIA types were classified by the apparent volume percent of their contained vapor bubbles at standard temperature and pressure. Inclusions were divided into one of four categories: VB35, VB20H, VB60, and VB85, where 'VB' stands for 'vapor bubble', the numeric value indicates the approximate volume percent of the inclusion occupied by the vapor bubble, and 'H' indicates the presence of a halite daughter crystal.

VB35 inclusions contain approximately 30 to 45 volume percent vapor; most do not contain daughter crystals (Figure 6a and 6b). Some inclusions contain a small, triangular, opaque daughter crystal, but don't contain translucent daughter crystals. VB35 inclusions commonly form large, planar arrays of small (1-3 μm) secondary inclusions, linear arrays of larger (5-30 μm) secondary FIAs, or isolated inclusions of unknown origin that vary greatly in size (1-55+ μm).

VB20H inclusions are brine inclusions that contain approximately 20 volume percent vapor and 80 volume percent liquid (Figure 6c and 6d), plus a halite daughter crystal. Some brine inclusions contain up to 7 additional translucent and opaque daughter crystals. The second most common translucent daughter crystal in

16

porphyry systems is KCl (sylvite), and a red translucent daughter, probably hematite is present in some inclusions. Additional translucent daughters are present but mineralogy is unknown. VB20H inclusions commonly occur in planar secondary assemblages of between 4 and 20 inclusions, or as individual inclusions of unknown origin. VB20Hs smaller than 5 μm are uncommon and they range in size up to about 60 μm. In several samples, VB20H inclusions were observed to co-exist in the same assemblage with VB85 inclusions.

VB60 inclusions contain approximately 60 volume percent vapor and 40 volume percent liquid, but can range from 55 to 75 volume percent vapor (Figure 6e, 6f and 6g). These inclusions rarely contain halite or other daughter crystals. VB60 inclusions are typically of unknown origin, and less commonly of secondary origin; inclusions range in size from 3 to 20 μm.

VB85 inclusions contain approximately 85 volume percent vapor and 15 volume percent liquid, though the vapor can range from 75 to almost 100 volume percent vapor (Figure 6h and 6i). These inclusions were never observed to contain daughter crystals, and they typically have an unknown origin. They occasionally occur in secondary FIAs, and are also found coexisting in an FIA with VB20H inclusions. VB85 inclusions typically range from 5 to 40 μm, but inclusions as large as 80 μm were rarely observed.

Fluid Inclusions Abundances

Relative abundances of each fluid inclusion type for a given sample location were approximated in A and AB veins present in a thick section and normalized to

100% (Figure 7). VB35 Inclusions are most common deep in the hydrothermal system and become less common at shallow depth; however, they are present throughout the entire system. VB35 inclusions represent 60-70% of all inclusions in A and AB veins in the deepest parts of the system, from 850 m to the deepest samples at 1300 m depth. VB35s show no lateral variation in abundance, though a dramatic change in distribution occurs above 850 m depth. Above this depth, VB35s no longer dominate and generally represent between 10 and 25% of all inclusions observed in A and AB veins. Two exceptions occur at 800 and 660 m depth, where VB35 inclusions comprise 45% and 90% of inclusions found in A and AB veins, respectively.

VB20H inclusions are rare in the deepest part of the system, from 1300 m to 1000 m depth, where they generally comprise less than 10% of inclusions observed in A and AB veins (Figure 7). Above 850 m, VB20Hs are generally, but not always the most abundant inclusion type, comprising 35 to 70% of all inclusions observed in A and AB veins at any one location. VB20H inclusions dominate the upper half of the hydrothermal system along with VB85 inclusions.

VB60 Inclusions are the least abundant inclusions observed in A and AB veins, but they are present throughout the system and in relatively consistent abundances; in only one location, at 180 m depth, do VB60s comprise more than a third of the observed inclusions (Figure 7). VB60 inclusions generally make up less than 18% of observed inclusions at any given location.

VB85 inclusions are abundant in A and AB veins above 850 m depth where they account for 25-50% of observed inclusions (Figure 7). Above 300 m, VB85

inclusions are the most abundant inclusion type in A and AB veins. In the deep part of the system, they typically comprise less than 5% of all inclusions observed in A and AB veins. VB85 inclusions typically mirror the distribution and abundances observed for VB20H inclusions.

It should be noted that VB20H and VB85 inclusions not only have a similar pattern of distribution and abundance at Batu Hijau, but these two inclusion types occur within the same FIAs, suggesting these two inclusion types form an immiscible pair. The observation of coexisting brine and vapor-rich inclusions in multiple secondary FIAs from throughout the deposit stands as evidence for fluid immiscibility at Batu Hijau. Immiscible pairs are observed throughout the deposit; however, they are most abundant above 800 m depth, coinciding with the decrease in abundance of VB35 inclusions and the increase in abundance of VB20H and VB85 inclusions notes previously. The abundance and distribution of fluid inclusion types and immiscible fluid pairs greatly suggests that a fluid became immiscible around 800 m below the surface of the deposit.

CHAPTER 5

MICROTHERMOMETRY

Microthermometric Data

Microthermometric data were collected from 324 fluid inclusions contained in 60 secondary and unknown fluid inclusions assemblages, along with eight isolated inclusions selected for SXRF analyses. Ice melting temperatures in VB35 inclusions ranged from -6.3 to 0 °C, with most final ice melting occurring between -3.0 and 0 °C. Salinities in VB35 inclusions ranged from 0 to 10 weight percent NaCl equivalent, with most salinities under 5 weight percent NaCl equivalent (Figure 8a) (Bodnar & Vityk, 1994). Upon heating, all VB35 inclusions homogenized to liquid. VB35 inclusions show two modes based on homogenization temperature - a lower temperature population between 260 and 330 °C, and a higher temperature population between 360 and 400 °C (Figure 8b).

Upon heating of VB20H inclusions, halite dissolution (Tm_H) occurred between 280 and 370 °C, with an average Tm_H of 311 °C. Salinities ranged from 36 to 48 weight percent NaCl equivalent, with an average salinity of 39.5 weight percent NaCl equivalent (Figure 8c) (Bodnar & Vityk, 1994). VB20H inclusions displayed two types of final homogenization: to the liquid phase, in which homogenization to liquid occurs at temperatures *above* halite melting, and by halite melting (Tm_H), in which homogenization to liquid occurs at temperatures *below* halite melting. VB20H inclusions homogenized to liquid (Th_L) between 310 and 490 °C (Figure 8d); inclusions showing final homogenization to liquid ($Th_L > Tm_H$) generally homogenized between 310 and 430 °C, whereas inclusions showing final

homogenization by halite melting ($Th_L < Tm_H$) generally homogenized between 340 and 490 °C. Average final temperatures of homogenization to liquid and by halite melting are 365 °C and 395 °C, respectively.

Ice melting temperatures for VB60 inclusions ranged from -7 to 0°C, with most final ice melting occurring between -5.0 and 0 °C. Salinities for VB60 inclusions ranged from 0 to 11 weight percent NaCl equivalent (Figure 8e) (Bodnar & Vityk, 1994). During heating, all VB60 inclusion vapor bubbles expanded to fill the inclusion. Accurate vapor bubble homogenization cannot be determined as the exact temperature of filling of the inclusion by vapor cannot be observed accurately (Sterner, 1992). Minimum temperatures based on the apparent disappearance of the last visible liquid were recorded and represent minimum homogenization temperatures. These temperatures ranged from 330 to 490 °C (Figure 8f). Most VB60s appeared to homogenize between 370 and 430 °C; the average minimum homogenization temperature in VB60 inclusions was 400 °C.

Observation of final ice melting temperatures in VB85 inclusions is difficult owing to the small amount of liquid present in the inclusions. Upon freezing, final ice melting was observed in 4 inclusions between -1.4 and -1.1 °C, corresponding to salinities between 1.9 and 2.4 weight percent NaCl equivalent (Figure 8g) (Bodnar & Vityk, 1994). Upon heating, VB85 inclusion vapor bubbles expanded to fill the inclusion. Apparent homogenization generally occurred between 340 and 400 °C, with most VB85s appearing to homogenize above 360 °C (Figure 8h). As with VB60 inclusions temperatures are minimum temperatures.

Hydro halite was observed in 15 VB35 inclusions, with melting temperatures

ranging from -23.3 to -16.0 °C. Clathrate was never observed in any fluid inclusion type, and there was no evidence to support the trapping of CO_2 or CH_4 within fluid inclusions found at Batu Hijau.

Microthermometry Discussion

In order to determine the temperature at which hydrothermal fluids were trapped within the Batu Hijau system, pressure corrections must be applied to the homogenization temperatures, which are minimum trapping temperatures for each inclusion. Inclusions may have been trapped anywhere along a constant density isochore that extends to higher temperatures and pressures from the recorded homogenization temperature and pressure. Trapping temperatures can be determined for individual inclusions if the pressure at which the hydrothermal fluids were trapped is known or can be approximated. The trapping temperature is the temperature at which the constant density isochore for each inclusion intersects the pressure of inclusion trapping, on a pressure-temperature diagram. Because the thickness of rock above the Batu Hijau deposit is known, and because Batu Hijau is a geologically young deposit that has experienced little post-formation erosion, pressures can be approximated from sample depths. Using a reconstructed cross section of the deposit (Figure 3), and assuming lithostatic pressure, inclusion trapping pressures were approximated from sample depth for each inclusion.

Constant Density Isochors

Inclusion densities and isochors for each fluid inclusion were determined

using the SoWat mathematical model (Driesner and Heinrich, 2006; Driesner, 2008). By inputting homogenization temperature, salinity, and volumetric constraints based on phase relationships, isochors can be regressed based on the equation $V_{Solution}(T, P, X_{NaCl}) = V_{H2O}(n_1 + n_2\ T, P)$ (Driesner, 2007); where volume, temperature, pressure, and molar volume are defined by V, T, P, and X, respectively (Driesner, 2007). The parameters n_1 and n_2 are simple functions of pressure and composition (Driesner, 2007). Constant density isochors for VB35 inclusions were generated and plotted relative to a liquid-vapor curve for a fluid of 5 weight percent NaCl equivalent based on determined salinities for most VB35 inclusions. Figure 9 shows two distributions of isochors, corresponding to homogenization temperature. Lower salinity (<1.0 weight percent NaCl equivalent) inclusions that have homogenization temperatures that range from about 240 to 350 °C correspond to higher densities (0.7 to 0.8 g/cm^3), whereas higher salinity inclusions (2-3 weight percent NaCl equivalent) have homogenization temperatures that range from about 370 to 415 °C and correspond to lower overall densities (0.5 to 0.65 g/cm^3).

Constant density isochors for VB20H inclusions were plotted relative to a liquid-vapor curve for a fluid of 45 weight percent NaCl equivalent based on determined salinities for most VB20H inclusions (Figure 10). Constant density isochors representing VB20H inclusions with homogenization temperatures from 305 to 490 °C range in density from 0.899 to 1.2 g/cm^3. VB20H inclusions are further distinguished based on mode of homogenization; inclusions that homogenized to liquid had densities between 0.89 and 1.10 g/cm^3, while inclusions homogenizing by halite melting had densities between 1.12 – 2.0 g/cm^3.

Constant density isochors for VB60 inclusions with homogenization temperatures from 390 to 500°C range from 0.3 – 0.52 g/cm^3 are shown in Figure 11. Isochors could not be determined for VB85 inclusions using the SoWat model, indicating that the minimum homogenization temperatures estimated for these inclusions were not accurate.

Inclusions Depths & Pressures

Samples were collected from 1300 m to about 150 m in depth below the current surface.   Assuming lithostatic pressure, these depths correspond to pressures between 75 and 325 bars (Burnham, 1984) (Figure 3).   Trapping pressures for VB35 inclusions based on inclusion depth (Figure 7) ranged from 325 bars in the deepest part of the system (1300 m), to less than 115 bars about 425 m below the surface. Trapping pressures for most VB20H inclusions ranged from 225 to 115 bars. Trapping pressures for most VB60 inclusions ranged from 325 to 115 bars. Trapping pressures for most VB85 inclusions were 160 bars or less.

Trapping Temperatures

Based on the intersection of each constant density isochore with the trapping pressure determined from sample depths, trapping temperatures were determined for individual fluid inclusions.   Trapping temperatures for 99 VB35 inclusions ranged between 248 and 396 °C (Table 2).   VB35 inclusions show two populations based on trapping temperature: a lower temperature population between 248 and 324 °C (58 inclusions), and a higher temperature population between 375 and 396

°C (31 inclusions).

In the deepest part of the deposit at 1300 m depth (Figure 12c), VB35 trapping temperatures ranged from about 287 to 396 °C. Most inclusions were trapped between 330 and 396 °C.

Between 600 and 1000 m depth (Figure 12b), trapping temperatures ranged from 248 to 387 °C; Trapping temperatures are slightly cooler when compared to VB35 inclusions from deeper in the deposit. Trapping temperatures in the center of the intrusive complex at these depths ranged from 248 to 386 °C; trapping temperatures in the flanks of the deposit showed a similar range.

In the shallow part of the system, above 600 m (Figure 12a), trapping temperatures ranged from 276 to 324 °C, indicating that somewhat cooler fluids were trapped at this higher elevation. Trapping temperatures in the center of the complex ranged from 284 to 321 °C, with most inclusions being trapped between 296 and 321 °C. These temperatures were generally higher than trapping temperatures on the flanks that ranged from 276 to 324 °C, with most inclusions being trapped between 276 and 303 °C. Temperatures are relatively consistent from 600 m depth to the shallowest VB35 sample location at 400 m depth.

Trapping temperatures for 23 VB20H inclusions were calculated, and temperatures ranged from 315 to 397 °C (Table 3). Most calculated trapping temperatures for VB20H inclusions were determined for inclusions that exhibit final homogenization to liquid; only a single trapping temperature was calculated for a VB20H inclusion that homogenized by halite melting.

The deepest VB20H inclusions were collected from between 900 and 1000 m

depth, and were trapped between 335 and 370 °C.   The majority of inclusions from this part of the deposit were trapped between 335 and 355 °C. In general, these trapping temperatures are similar to trapping temperatures from VB35 inclusions from the same location. Between 625 and 800 m depth, trapping temperatures ranged from 315 to 397 °C, however most were trapped between 315 and 335 °C.

In the shallow part of the system only two trapping temperatures were calculated (Figure 12a). These two VB20H inclusions were trapped between 500 and 600 m depth, and recorded trapping temperatures of 340 and 355 °C. The hotter of the two VB20H inclusions was located at 580 m depth and in the center of the intrusive complex, while the cooler inclusion was located a 530 m depth and on the deposit flank. The single VB20H inclusion that homogenized by halite melting was located in this area, and recorded a cooler trapping temperature of 327 °C.

Calculations to determine trapping temperatures for several VB20H inclusions that homogenized by halite melting were not possible because indicated homogenization temperatures were theoretically too high for the indicated trapping pressure. These results suggest two possibilities: 1) these inclusions were trapped at higher pressures, most likely due to local over pressuring, and trapping pressures cannot be calculated, and 2) after trapping, fluid leaked out of the inclusions, resulting in apparent inclusion salinities that do not reflect the actual salinities of the fluid trapped in the inclusions.   As a result, trapping temperatures were determined for only a single inclusion that homogenized by halite melting.

CHAPTER 6

SYNCHROTRON X-RAY FLUORESCENCE

SXRF Data

Twenty-five fluid inclusions from nine different samples and five drill holes were analyzed and low-resolution gray-scale elemental distribution maps were produced. Gray-scale maps were produced for each of the 25 inclusions and eleven analyses provided maps with sufficient detail for interpretation. Data from these eleven analyses were re-reduced to provide the final color elemental distribution maps.

It should be noted that quantitative elemental concentrations couldn't be obtained with SXRF analyses, and elemental distribution maps display relative concentrations of elements, based on the range of concentrations for each element in each inclusion. Because of this, elements in inclusions with low total dissolved components can appear to be highly concentrated.

It should also be noted that orientation of analyses, and thus the orientation of the elemental distribution maps differ from the fluid inclusion photographs by 45°. This difference in orientation can make interpreting the location and association of elemental concentrations difficult. In addition to the difference in orientation, the small size of the analyzed inclusions, combined with the relatively large scanning resolution of the SXRF technique, results in ambiguity when interpreting the location of elemental concentrations within an inclusion. Deciphering elemental distribution between the liquid and vapor phases and correlating elements to solid daughter crystal phases is not possible in all

27

inclusions; however, using the knowledge that some elements, such as Cu, Cl, K, and Ti can commonly be contained within solid phases, daughter crystals can be identified with this technique in some inclusions. In the following sections, no attempt will be made to resolve elemental distributions between the liquid and vapor phases, and elemental concentrations associated with either of these phases will be referred to as being associated with liquid/vapor. Any further interpretation relating to the location and distribution of elements cannot be made with certainty. It is suggested that for future studies, only inclusions exceeding 75 μm should be analyzed with this technique; this technique is thus not preferred for the study of inclusions within most porphyry systems.

While elements up to atomic weights of 82 were evaluated in the analyses, only 16 total elements were identified: Ag, Br, Ca, Cl, Cr, Cu, Fe, Ge, K, Mn, Pb, Sr, Ti, Zn, and Zr. The absence of light elements is due to the absorption of the fluorescence radiation in the top quartz layer and in the air path between sample and detector (Appel, Personal Communication, 2011). Of the 11 evaluated inclusions, 10 were VB20H inclusions and one was a VB60 inclusion; no viable elemental distribution maps were produced for VB35 or VB85 inclusions.

Owing to their ample liquid phases and abundant daughter crystals, the majority of successful SXRF analyses evaluated VB20H fluid inclusions. These inclusions typically have elevated Br, Cu, Fe, Mn, and Zn, and less commonly have elevated K, Mo, and Ti. Iron, Mn, and Zn typically occur together and their signals coincide. Within these inclusions, Cu exhibits two types of associations: 1) Cu is coincident with iron in proximity to a visible opaque daughter crystal (Figure 13);

or 2) Cu is more diffuse, generally coinciding with the liquid/vapor phase of the inclusion (Figure 14) and is not specifically associated with an opaque daughter crystal.

Bromine, Ca, Cr, Ag, Pb, K, and Sr all are elevated coincident with elevated Fe, Mn, and Zn in various VB20H inclusions. Areas of K and Cl enrichment overlap and coincide with solid, translucent daughter crystals (salts), as observed in inclusions BH044 (Figure 13) and BH061 (Figure 15). Titanium is enriched in small, isolated areas contained within the fluid phase of the inclusions (Figures 13 and 15). Molybdenum shows two distinct patterns of distribution in VB20H inclusions. The first pattern is as small, enriched areas, coinciding with an observed daughter crystal as in inclusion BH023 (Figure 16). The second pattern shows that the host quartz surrounding the fluid inclusions is enriched in Mo relative to the fluid contained within the inclusion (Figure 13).

Like Mo in BH044, Zr is elevated in the host quartz relative to the fluid inside the fluid inclusion (Figure 13). Germanium shows the opposite behavior, being enriched within the inclusions relative to the surrounding host quartz (Figures 17 and 18).

Due to their low fluid density and lack of daughter crystals, elemental detection in VB60 inclusions proved difficult. Like the VB20H inclusions, Fe, Mn, and Zn are elevated and coincide (Figure 19) and probably reflect the location of the liquid phase, which is in the lower left corner of the inclusion.   As with VB20H inclusions, Br is present and shows the same distribution and relative abundance as Fe, Mn, and Zn (Figure 19). Copper is highly concentrated in a small area that is

adjacent to a zone of elevated Fe (Figure 19) and probably indicates the presence of a Cu-bearing daughter crystal that is not visible in the inclusion, but which is attached to the large vapor bubble.

Elemental distribution maps for VB35 and VB85 fluid inclusions did not distinguish relative concentration differences. An example of a typical elemental distribution map for a VB35 or VB85 type inclusion is shown in Figure 20.

SXRF Discussion

The two distinct locations of Cu within VB20H inclusions indicate differing occurrences of Cu within the fluid inclusions and also indicate varying concentrations of Cu within brines that were trapped by VB20H inclusions. The coincident presence of Cu and Fe with a visible opaque daughter crystal most likely confirms the presence of a Cu-Fe sulfide daughter crystal in the liquid phase. This pattern is present in inclusions BH044 (Figure 13), BH023 (Figure 16), and BH057 (Figure 21), among others. VB20H inclusions that contain a Cu-Fe sulfide daughter crystal confirm that the brine was more concentrated in Cu, Fe, and S than other inclusions that display a more diffuse pattern for Cu that is coincident with the liquid/vapor phase. These inclusions lack a Cu-Fe sulfide daughter and contain lower Cu, Fe, and S.

Signals for Fe, Mn, and Zn coincide in all inclusions where the three elements are present (Figures 13, 15, and 19), suggesting the consistent presence of these metals in the hydrothermal brines. These signals coincide with the liquid/vapor phase of the inclusion, suggesting that these elements are more abundant in high-

density brine fluids. These three elements could also be concentrated in a Fe-Mn-Zn bearing salt and/or daughter crystal; however, the diffuse nature of the signals suggests that these elements are enriched in the hydrothermal fluid. The diffuse nature of elevated Br (Figure 13), Ca (Figures 13 and 14), Cl (Figure 15), and Sr (Figures 13 and 15) and coincidence with elevated Fe, Mn, and Zn suggest these elements are also relatively enriched and in brine liquid/vapor, and were partitioned into the liquid phase during fluid immiscibility and brine formation.

The association of elevated K and Cl (Figures 13 and 15) with salt daughters confirms the observation of sylvite, and indicates the presence of salt daughter crystals including halite and sylvite. It is also likely that some K and Cl are present dissolved within the liquid/vapor phase of these inclusions, and these signals are combined with those derived from solid daughter crystals.

The distribution of Ti is consistent with a small daughter crystal or salt rather than dispersion of dissolved Ti in the liquid/vapor. This is observed in inclusions BH044 (Figure 13), BH061 (Figure 15), BH036 (Figure 17), and BH057 (Figure 21).

Molybdenum appears to show two distribution patterns, but in fact, only one pattern accurately reflects the distribution of Mo within VB20H inclusions. This pattern indicates elevated Mo, most likely in a Mo-bearing (molybdenite) daughter crystal (Figure 16). In the second pattern, Mo exhibits low concentrations within the inclusion as compared to enriched Mo in surrounding host quartz (Figure 13). This pattern is an artifact of the analytical technique (Appel, personal communication, 2011).

Similar to Mo, the apparent Zr enrichment in the host quartz is an artifact of the analysis (Appel, personal communication, 2011), and indicated that dissolved Zr is non-existent in these fluids (Figures 13 and 15). Alternatively, Ge is enriched within the inclusions relative to the surrounding host quartz (Figure 17 and 18), suggesting that some Ge was transported by hydrothermal brines. However, since Ge concentrations are likely to be extremely low in the host quartz, concentrations within the hydrothermal fluids are also probably quite low.

Elemental detection in VB60 inclusions proved to be difficult due to the low density of the fluids and low elemental concentrations dissolved in inclusion fluids; however, one VB60 inclusion was successfully analyzed. The small area of elevated Cu suggests that a non visible Cu-bearing daughter crystal is present, but obscured by the large vapor bubble (Figure 19). Because that area of Cu enrichment does not overlap with elevated Fe, the daughter crystal appears to be an Fe-poor, Cu-bearing daughter crystal. However, the presence of a daughter crystal demonstrates that Cu can be significantly enriched in low-density fluids, in such abundances that Cu-bearing daughter crystals can precipitate from these vapors during cooling and depressurization of the system.

Like the VB20H inclusions, the coincidence of Fe, Mn, and Zn in VB60 inclusions most likely indicates these metals are coincidentally present in the hydrothermal fluid, but do not form daughter crystals. There are no visible daughter crystals in this VB60 inclusion; however, due to the large vapor bubble, solid phases may be difficult to see. Nevertheless, as in VB20H inclusions, the diffuse patterns of Fe, Mn, and Zn distribution suggest they remain dissolved in the fluid

phase (Figure 19). Bromine is also interpreted as dissolved in the fluid, as its relative abundance and distribution coincides with elevated Fe, Mn, and Zn (Figure 19).

Due to small fluid inclusion size, low elemental abundances, lack of daughter crystals, and low fluid densities, elemental distribution maps for VB35 and VB85 inclusions did not reveal elevated elemental concentrations within these inclusions (Figure 20).

CHAPTER 7

LASER ABLATION-INDUCTIVELY COUPLED PLASMA-MASS SPECTROMETRY

LA-ICP-MS Data

Elemental concentrations within fluid inclusions were quantified using LA-ICP-MS analyses. Analyzed elements include: B, Na, K, Ca, Mn, Fe, Zn, As, Rb, Sr, Mo, Ag, Sb, Ba, W, Au, and Pb, and concentrations detected in each analyzed inclusion are listed in Appendix 1.   Limits of detection varied for each element and during each analytical run. Limits of detection varied from > 1 ppm to over 10000 ppm, but were generally between 10 and 1000 ppm. Elemental concentrations that were below limits of detection are denoted with a '-' in Appendix 1; elements that were not included in the analysis are left blank.

Of the 17 elements that were analyzed, some were more commonly detected than others. Arsenic, Ag, Au, B, Mo, Sb, and W were all rarely detected in any fluid inclusions type; where detected, their concentrations were always <450 ppm, with many having concentrations <0.1 ppm. Barium, Rb, and Sr were more commonly detected than the previously mentioned elements, but they typically had low concentrations. Rubidium and Sr concentrations rarely exceeded 200 ppm, while Ba concentrations were typically <400 ppm. VB20H inclusions are an exception and Ba concentrations reached 5031.9 ppm, Rb concentrations reached 765.34 ppm, and Sr concentrations reached 350.41 ppm.   Barium, Rb, and Sr concentrations were consistently low or below detection in VB60 and VB85 inclusions.

Elements that were commonly detected and present in significant concentrations include: Na, K, Ca, Mn, Fe, Zn, Pb, and Cu.   Concentrations for each

analyzed inclusion can be found in Appendix 2; summary data are in Table 4. Concentrations for these elements were highest in VB20H inclusions, which have average concentrations up to an order of magnitude greater than average concentrations in VB35 inclusions, which contained the second highest average concentrations of these elements. Average concentrations in VB35 inclusions were typically less than an order of magnitude greater than average concentrations in VB60 inclusions. Exceptions include Cu, which on average was greater by about a third in VB60 inclusions than in VB35 inclusions and Fe which was higher in VB60 inclusions by about 7%. Average elemental concentrations are the lowest in VB85 inclusions, with some average concentrations as much as two orders of magnitude less than average concentrations in VB60 inclusions. Sodium, Ca, and Cu have the highest average concentrations in VB85 inclusions, with average concentrations between 227.0 and 247.0 ppm. Iron, K, Mn, and Zn were all detected in VB85 inclusions, but at average concentrations of <75.0 ppm. Lead was detected in relatively low concentrations, with an average concentration of <1.0 ppm.

Elemental abundance data from LA-ICP-MS were used to confirm salinities obtained from ice melting and halite dissolution temperatures during microthermometry. Abundances for metal chlorides NaCl, KCl, $FeCl_2$, and CuCl were summed, and calculated salinities are shown for each inclusion in Appendices 2.1-2.4.

X-Y plots of important elements were evaluated to identify and quantify elemental correlations (Figures 22-37). Inclusion types are differentiated by symbol. Linear regression analyses were used to evaluate data for each inclusion type, and the R^2 coefficient of determination between element pairs was calculated (Table 5). A range of degrees of correlation are indicated, with some elements being highly correlated and other elemental pairs being weakly correlated, or not correlated at all. R^2 values are color-coded based on degree of correlation, and categorized as high ($R^2 = 0.70 - 1.0$), moderate ($R^2 = 0.35 - 0.69$), and weak/no correlation ($R^2 = 0.0 - 0.34$).

Some general trends can be observed across all inclusions types. Manganese and Zn, along with Mn and K correlate strongly in all inclusions types (Table 5). Copper, on the other hand, displays weak or no correlation with all elements in VB20H inclusions, and weak to moderate correlation with all elements in VB35 inclusions; however, in VB60 and VB85 inclusions, Cu correlates strongly with all metals. Elements in VB35 and VB20H inclusions generally correlate weakly, while elements in VB60 and VB85 inclusions generally correlate strongly.

In VB35 fluid inclusions, elemental correlations are generally moderate to low (Table 5). Sodium correlates strongly with K (Figure 22), and Mn correlates strongly with K (Figure 23), and with Zn (Figure 24). Copper correlates moderately with K (Figure 25), Mn (Figure 26), Zn (Figure 27), Fe (Figure 28), and Pb (Figure 29). Correlations are weak or absent for Ca with Na (Figure 30), and K (Figure 31);

for Cu with Na (Figure 32), Ca (Figure 33), and Ba (Figure 34); for Mn with Fe (Figure 35) and Pb (Figure 36); and for Zn with Fe (Figure 37).

In VB20H fluid inclusions, most elemental correlations are similarly low (Table 5). High correlations exist for Mn with K (Figure 23) and Zn (Figure 24); for Ca and Na (Figure 30), and Mn and Pb (Figure 36). Manganese and Fe (Figure 35), and Zn and Fe (Figure 37) correlate moderately. Weak or no correlation exists for Cu with K (Figure 25), Mn (Figure 26), Zn (Figure 27), Fe (Figure 28), Pb (Figure 29), Na (Figure 32), Ca (Figure 33), and Ba (Figure 34); Na with K (Figure 22), and Ca with K (Figure 31) also correlate weakly.

In VB60 fluid inclusions, elemental correlations are generally high (Table 5). High correlations exist for Na with K (Figure 22), and Mn with K (Figure 23), and Zn (Figure 24); for Cu with K (Figure 25), Mn (Figure 26), Zn (Figure 27), Fe (Figure 28), Pb (Figure 29), Na (Figure 30), and Ca (Figure 33); for Ca and K (Figure 31); for Mn with Fe (Figure 35) and Pb (Figure 36); and for Zn with Fe (Figure 37). All VB60 plots display a similar pattern: the majority of data plot at relatively high concentrations of both elements, and two to five data points at lower concentrations. Moderate correlations exist for Cu with Na (Figure 32) and Ba (Figure 34). In VB60 inclusions, no elemental pairs had weak correlations.

In VB85 fluid inclusions, elemental correlations are generally high and high correlations exist between Na and K (Figure 22), and Mn with K (Figure 23) and Zn (Figure 24); for Cu with K (Figure 25), Mn (Figure 26), Zn (Figure 27), Fe (Figure 28), Pb (Figure 29), and Ba (Figure 34); for Ca with Na (Figure 30) and K (Figure 31); and for Mn with Fe (Figure 35) and Pb (Figure 36). Moderate correlations exist

37

between Cu with Na (Figure 32) and Ca (Figure 33), and Zn and Fe (Figure 37). In VB85 inclusions, no elemental pairs had weak correlations.

<div style="text-align:center">X/Na Plots</div>

Elemental concentrations measured by LA-ICP-MS were also ratioed by mass to Na concentrations to provide a consistent base for comparison, and inclusions were plotted in order of decreasing Cu/Na mass ratio for each inclusion type.   Each point represents one analysis of a single fluid inclusion.   Analyses for which an element was detected, but was below limits of detection are shown as points below the red line.   Base metals are included in group 1 (Figure 38), typical salt cations and precious metals are included in group 2 (Figure 39), and reactive and rarely detected trace elements are included in group 3 (Figure 40). Copper, a highly reactive element, is plotted with all three groups to show relationships of other elements to Cu.   Concentration ranges are summarized in Table 6. Elements were classified as reactive and non-reactive based on whether their ratios with Na varied by greater than about an order of magnitude, barring outliers, or less than an order of magnitude, respectively (Ulrich et al., 2003). The classification of an element as either reactive or non-reactive is however, subjective. Elemental reactivity can vary across inclusion types for individual elements, and this classification is not always clear cut.

Group 1 elements include Cu, Fe, Mn, Zn, and Pb (Figure 38).   This group includes important base metals that were that were commonly present and, with the exception of Pb, abundant in inclusions throughout the deposit. Mass ratios of

Cu/Na range from 0.001 to 210 (Figures 38-40; Table 6) and Cu was below detection in some VB20H, VB35, and VB60 inclusions, but not in VB85 inclusions. The Cu/Na ratios show a wide range of values for all inclusion types, and ranges from 0.004 to 3.5 in VB20H inclusions, from 0.001 to 10 in VB35 inclusions, and from 0.004 to 30 in VB60 inclusions. In VB85 inclusions, Cu/Na ratios range from 0.025 to 210. The range of values for Cu/Na generally increased from VB20H to VB35 to VB60 to VB85 inclusions. No large gaps or breaks are present across the range of values for Cu/Na for each fluid inclusion type from relatively high to relatively low Cu/Na ratios (Figure 38).

Ratios of Fe/Na range from 0.0007 to 13.0 (Table 6), with the majority of ratios ranging from 0.7 to 3.0 though Fe is below detection in a significant number of inclusions (Figure 38). In general, the Fe/Na ratio varies over several orders of magnitude for each inclusion type, though the majority of analyses show a smaller degree of variation. In VB20H inclusions, Fe/Na ratios range from 0.0007 to 11.0, with most VB20H inclusions ranging from 0.015 to 4.0. There is no correlation between Fe/Na and the presence or absence of hematite daughter crystals in inclusions. In VB35 inclusions Fe/Na ratios range from 0.02 to 11.0, with Fe in many inclusions below detection, and most Fe/Na ratios range from 0.01 to 1.0. Eight VB35 inclusions with opaque daughter crystals had Fe/Na ratios that range from 0.5 to 0.95 with one outlier of 0.06. With decreasing Cu/Na, Fe detection decreased, but Fe was still detected in about half of these inclusions. In VB60 inclusions, Fe/Na ratios range from 0.0015 to 13.0, with Fe in many inclusions below detection. Ratios of Fe/Na in most VB60 inclusions range from 0.01 to 1.0. In

VB85 inclusions, Fe/Na ratios range from 0.009 to 4.0, with Fe in many inclusions below detection. In VB85 inclusions with a high Cu/Na, Fe is rarely detected. Copper and Fe covary to some degree as at moderate values of Cu/Na, Fe/Na ratios range from 0.5 to 1.0, whereas at very low Cu/Na, Fe/Na ratios range from 0.009 to 0.035.

Ratios of Mn/Na range from 0.002 to 6.5 (Table 6) with most ratios from 0.08 to 0.5, and Mn in some inclusions below detection (Figure 38). Compared to most other elements, Mn/Na ratios exhibit relatively consistent ratios. In VB20H inclusions, Mn/Na ratios range from 0.02 to 6.5, Mn in some inclusions is below detection, and Mn/Na ratios in most VB20H inclusions range from 0.09 to 0.55. In VB20H inclusions with low Cu/Na ratios, Mn detection becomes less common. In VB35 inclusions, Mn/Na ratios range from 0.04 to 6.5, with Mn in some inclusions below detection. Ratios in most VB35 inclusions range from 0.04 to 0.3 and Mn is less commonly detected in VB35 inclusions with low Cu/Na ratios. In VB60 inclusions, Mn/Na ratios range from 0.002 to 0.9, with Mn in some inclusions below detection. Ratios in most VB60 inclusions range from 0.095 to 0.3. Unlike VB20H and VB35 inclusions, Mn detection was not linked to Cu/Na ratio in VB60 inclusions. In VB85 inclusions, Mn/Na ratios range from 0.095 to 0.45, with Mn in some inclusions below detection. Manganese was rarely detected in VB85 inclusions with high Cu/Na ratios, but is more commonly present in VB85 inclusions with low Cu/Na ratios.

The ratios of Zn/Na range from 0.002 to 2.0 (Table 6) with Zn/Na in most inclusions ranging from 0.02 to 0.2, and Zn in some inclusions below detection

(Figure 38). In general, Zn/Na ratios are most variable in VB20H inclusions, but most values are more consistent for other inclusion types. In VB20H inclusions, Zn/Na ratios range from 0.0095 to 2.0, with most ranging from 0.04 to 0.4. The Zn/Na ratios in VB20H inclusions are unrelated to Cu/Na ratios.   In VB35 inclusions, Zn/Na ratios range from 0.008 to 2.0, with most Zn/Na ratios ranging from 0.015 to 0.1. Zinc was below detection in two VB35 inclusions, and the Zn/Na ratios in VB35 inclusions are unrelated to the Cu/Na ratio. In VB60 inclusions, Zn/Na ratios range from 0.002 to 0.85, with most Zn/Na ratios ranging from 0.06 to 0.2.   Zinc is below detection in one inclusion, and the Zn/Na ratios generally decreased with decreasing Cu/Na ratio in VB60 inclusions. In VB85 inclusions, Zn/Na ratios range from 0.045 to 0.5, with most Zn/Na ratios ranging from 0.045 to 0.15. Zinc was below detection in four VB85 inclusions. Zinc is rarely detected in VB85 inclusions with high to moderately high Cu/Na ratios, and was more commonly detected in VB85 inclusions with lower Cu/Na ratios.

The ratios of Pb/Na range from 0.0006 to 0.2 (Table 6) with Pb/Na in most inclusions ranging from 0.001 to 0.1, and Pb in some VB35, VB60, and VB85 inclusions below detection (Figure 38). Lead values are low and in general, Pb/Na ratios are fairly consistent, though analyses of VB20H inclusions show somewhat greater variability. In VB20H inclusions, Pb/Na ratios range from 0.001 to 0.2, with most ranging from 0.04 to 0.1. In VB35 inclusions, Pb/Na ratios range from 0.0006 to 0.1, with most ratios ranging from 0.0009 to 0.009, and Pb in some VB35 inclusions below detection. In VB60 inclusions, Pb/Na ratios range from 0.0008 to 0.1, with most ranging from 0.003 to 0.03, and Pb in some VB60 inclusions below

41

detection. In VB85 inclusions, Pb/Na ratios range from 0.002 to 0.02, with Pb in some VB85 inclusions below detection.

Group 2 elements include K, Ca, Mo, Ag, and Au (Figure 39). This group is composed of common salt cations and "precious metals" that were relatively non-reactive and not commonly detected.

Ratios of K/Na range from 0.008 to 9.5 (Table 6), with the majority of inclusions having ratios between about 0.2 and 0.95, and K in with some inclusions below detection (Figure 39). Ratios of K/Na were fairly consistent across all inclusion types. In VB20H inclusions with high Cu/Na ratios, K/Na ratios range from 0.09 to 9.5 and K was detected in all inclusions. In VB20H inclusions with moderate to low Cu/Na ratios, K/Na ratios range from 0.15 to 9.0, with most K/Na ratios ranging from 0.15 and 1.0; K in some inclusions is below detection. In VB35 inclusions, K/Na ranges from 0.08 to 7.0, with most ratios ranging from 0.2 to 0.8. However, K was below detection in more than half of VB35 inclusions. In VB60 inclusions, K/Na ratios range from 0.008 to 1.0, with most ranging from 0.1 to 1.0. As in VB35 inclusions, K in more than half of VB60 inclusions was below detection. In VB85 inclusions, K/Na ratios range from 0.05 to 8.0, with most ranging from 0.2 to 0.9. K/Na ratios decrease as Cu/Na ratios decrease.

Ratios of Ca/Na range from 0.00085 to 7.0 (Table 6) with Ca in some inclusions below detection (Figure 39). Most Ca/Na ratios range from 0.02 to about 1.0. Calcium has a very large range of ratios, indicating its reactivity; however, ratios are relatively similar across all inclusions types. In VB20H inclusions, Ca/Na ratios ranged from 0.0008 to 5.0, and Ca was detected in all but 1 VB20H inclusion. In

42

VB35 inclusions, Ca/Na ratios range from 0.015 to 9.0, and Ca was detected in less than half of VB35 inclusions. In VB60 inclusions, the Ca/Na ratios range from 0.005 to 1.0, decrease with decreasing Cu/Na ratios, and Ca below detection is more common at very low Cu/Na ratios. In VB85 inclusions, Ca/Na ratios range from 0.07 to 3.0, and Ca was not detected in VB85 inclusions with high Cu/Na ratios; however, relatively high Ca/Na ratios were quantified for inclusions with low Cu/Na ratios.

Ratios of Mo/Na range from 0.002 to 0.0075 (Table 6) and Mo was detected in only three VB20H, one VB35, and six VB85 inclusions (Figure 39). Ratios of Mo/Na in three VB20H inclusions range from 0.004 to 0.005 and Mo was only detected in VB20H inclusions with high Cu/Na ratios. A Mo/Na ratio of 0.0065 was detected in one VB35 inclusion with moderately high Cu/Na. Molybdenum was below detection in all VB60 inclusions. Ratios of Mo/Na in six VB85 inclusions range from 0.002 to 0.0075. One group of three VB85 inclusions has Mo/Na ratios that range from 0.002 to 0.0035, while a second group of three inclusions have ratios that range from 0.007 to 0.0075. All VB85 inclusions in which Mo was detected have low Cu/Na ratios. All other analyses indicate was below detection.

Ratios of Ag/Na range from 0.0045 to 0.0008 (Table 6) and Ag was only detected in four VB20H and two VB85 inclusions (Figure 39). In VB20H inclusions, Ag/Na ratios range from 0.0005 to 0.00055. Silver was detected in three VB20H inclusions with high Cu/Na ratios, and one VB20H inclusions with a moderate Cu/Na ratio. In VB85 inclusions, Ag/Na are 0.0004 and 0.00085. Silver was detected in inclusions with low Cu/Na. In all other analyses, Ag was below detection.

Gold was detected above the limits of detection in one VB35 inclusion (Table 6). This inclusion had an Au/Na ratio of ~0.0001 and a moderate Cu/Na ratio (Figure 39).

Group 3 elements include As, Ba, Sr, W, B, Li, and Rb (Figure 40). This group includes relatively reactive trace elements and elements that were only rarely detected. Arsenic with an As/Na ratio of 0.006 was only detected in one LA-ICP-MS analysis in a high Cu VB85 inclusion (Table 6).

Ratios of Ba/Na range from 0.00007 to 0.18 (Table 6) with Ba in a number of inclusions below detection (Figure 40). Ratios of Ba/Na are commonly between 0.001 and 0.02. In general, Ba/Na ratios exhibit a range of values for all inclusion types, and are most variable in VB20H inclusions. In these inclusions the Ba/Na ratios range from 0.00007 to 0.18, and most inclusions ranged from 0.002 to 0.018. Ratios of Ba/Na are more consistent at lower Cu/Na ratios, with Ba/Na ratios ranging from 0.006 to 0.01. In VB35 inclusions, Ba/Na ratios range from 0.0008 and 0.04, with some inclusions below detection limits, and most ratios ranging from 0.001 to 0.008. In VB60 inclusions, Ba/Na ratios range from 0.00008 to 0.065, with some inclusions below detection limits, and most ratios ranging from 0.002 to 0.009. In VB85 inclusions, Ba/Na ratios range from 0.001 to 0.07, with some inclusions below detection limits, and most ratios ranging from 0.004 to 0.03. Barium was primarily detected in low-Cu/Na VB85 inclusions.

Ratios of Sr/Na range from 0.000045 to 0.03 (Table 6) with Sr in some inclusions below detection (Figure 40). In general Sr/Na ratios show significant variability in VB20H inclusions and lesser variability in other inclusion types. In

VB20H inclusions, Sr/Na ratios range from 0.00006 to 0.03. In VB35 inclusions, Sr/Na ratios were more consistent and range from 0.0004 to 0.0085, with some inclusions below detection limits. In VB60 inclusions, Sr/Na ratios range from 0.0015 to 0.015, with some inclusions below detection limits. VB60 inclusions with lower Sr/Na ratios coincide with inclusions with lower Cu/Na ratios. In VB85 inclusions, Sr/Na ratios range from 0.0015 to 0.02, with some inclusions below detection limits. Ratios of Sr/Na in VB85 inclusions had the smallest range of any inclusions type, and Sr was not detected in inclusions with high Cu/Na ratio.

Tungsten was only detected in a few VB20H and VB85 inclusions (Table 6). In VB20H inclusions, W/Na ratios range from 0.000095 to 0.0008, and in VB85 inclusions W/Na ratios range from 0.008 to 0.0045 (Figure 40). Tungsten was detected in VB20H inclusions with high and moderately high Cu/Na ratios VB20H's. Tungsten was detected in VB85 inclusions with moderate to low Cu/Na ratios.

Ratios of B/Na range from 0.0009 to 0.055 (Table 6) with B in many inclusions being below detection (Figure 40). No regular pattern of distribution was observed for any inclusion type, and only a few inclusions of all inclusions types contained B. Most analyses that were below detection were from VB85 inclusions; B was only detected in VB85 inclusions with moderate to low-Cu/Na ratios.

Lithium was only detected in 3 VB20H fluid inclusions and was below detection in all other inclusion types (Table 6). Ratios of Li/Na in these three inclusions ranged from 0.0003 to 0.02 (Figure 40).

Ratios of Rb/Na range from 0.0005 to 0.07 (Table 6), with Rb in with some inclusions below detection (Figure 40). In VB20H inclusions, Rb/Na ratios are quite

45

variable and range from 0.0006 to 0.07. In VB35 inclusions, Rb/Na ratios range

from 0.0005 to 0.001, and Rb was below detection in most VB35 inclusions with

high Cu/Na ratios. In VB60 inclusions, Rb was only detected in two inclusions: one

VB60 inclusion with a moderate Cu/Na ratio, and one VB60 inclusion with a low

Cu/Na ratio, and ratios range from 0.00095 to 0.001. In VB85 inclusions, Rb/Na

ratios range from 0.0008 to 0.0025. Rubidium was only detected in VB85 inclusions

with low Cu/Na ratios. The largest range of Rb/Na ratios is present in VB20H

inclusions; ratios are more consistent in VB35, VB60, and VB85 inclusions, but

values above detection are rare relative to VB20H inclusions.

<u>Discussion of X-Y and X/Na Plots</u>

Degrees of correlation were calculated and expressed as R^2 values for

elemental pairs examined by the X-Y plots for each inclusions type. The degrees of

correlation can be used to interpret the reactivity of the elements within the various

fluids at Batu Hijau. In general, consistently low R^2 values for elements in a

particular inclusion type indicate that that element was reactive, and reacted with

wall rocks and was variably removed from the fluid as it moved through the

hydrothermal fluid (Ulrich *et al.*, 2001). Alternatively, consistently high R^2 values

for elements in a particular inclusion type indicate that the element was non-

reactive, and remained in the fluid as the fluid moved upward through the

hydrothermal system. Elements that have R^2 values indicating moderate correlation

behave as moderately reactive elements. Inspection of Table 6 indicates that most

elements in fluids trapped in VB60 and VB85 inclusions were non reactive.

Alternatively, Cu, Na, K, and Ca in VB20H fluids were reactive and variably lost to or removed from wall rocks. Similarly, Cu, Na, K, Ca, Ba, and to a lesser degree Fe and Pb in VB35 fluids were reactive and were variably lost to or removed from wall rocks.

Copper most frequently exhibits low and moderate R^2 values indicating that Cu in VB35 and VB20H fluids was highly reactive and lost to wall rocks through fluid-rock reaction and precipitation of Cu-Fe sulfides. Iron is reactive or moderately reactive and was likely lost to wall rocks with Cu during the precipitation of magnetite and Cu-Fe sulfides such as chalcopyrite, bornite, and diginite, along with minor pyrite. However, Fe is somewhat less reactive in VB20H fluids, indicating that wall rock reactions and precipitation involving Fe may have decreased after fluid immiscibility generated the VB20H fluid. Potassium, observed to be reactive, is likely associated with early potassic alteration and the formation of secondary K feldspar and biotite, and later and cooler phyllic alteration and the formation of sericite. Barium can be lost to wall rocks as a substitute for other cations in feldspars (Ulrich *et al.*, 2001). High R^2 values for Mn, Zn, and Pb indicate that these elements were relatively non-reactive, were relatively unaffected by wall-rock reactions or mineral precipitation, and were transported through the system in VB35 and VB20H fluids. These results and interpretations are supported by a lack of minerals containing these elements in the sampled parts of the deposit.

In the non-reactive VB60 and VB85 fluids, nearly all element pairs have high degrees of correlation, indicating that wall-rock reactions and precipitation was uncommon as these low density fluids with generally lower concentrations of

47

metals and other elements moved through the deposit. Not all element pairs, however, had high degrees of correlation. In both VB60 and VB85 fluids, Cu displays moderate reactivity with some elements, suggesting that Cu and possibly to a lesser degree Ba and Na were precipitating from these fluids. In addition, Fe in VB85 fluids was likely reacting with wall rocks and/or precipitating with Cu in Cu-Fe sulfides, although these reactions were likely minor in comparison to those associated with VB35 and VB20H fluids.

The degree of reactivity of elements is also indicated on Figures 38 through 40, in which elements are ratioed to Na. Reactive elements include Cu, Fe, Ca, K, and Sr and Ba; variations in the concentrations of these elements are the result of wall rock reactions and mineral precipitation as fluids moved through the deposit. Non-reactive elements include Pb, Mn, Zn, Mo, Au, Ag, B, Rb, W, As, and Li. Elemental concentrations and ratios with sodium remain generally consistent while temperature, pressure, and concentrations of reactive elements vary, suggesting that lesser to no wall rock reactions or mineral precipitation occurred involving these elements.

<u>Spatial distribution of Cu Concentrations in Fluid Inclusions</u>

Concentrations were quantified for a number of elements using LA-ICP-MS analyses; however, the main element of interest at Batu Hijau is Cu. Average Cu concentrations of FIAs were plotted on a cross-section through the deposit for each inclusion type (Figures 41-44), (PT Newmont Nusa Tenggara, private communication, 2009). Using whole rock Cu assay data along an east-west cross

48

section of the deposit, a comparison between Cu concentrations obtained from LA-ICP-MS and whole rock analyses can be made (Figures 45-48), (PT Newmont Nusa Tenggara, private communication, 2009).

Figures 41 through 44 illustrate the spatial distribution of Cu concentrations (ppm) in the various types of fluid inclusions throughout the deposit. In the following discussion, the deposit is divided into three regions based on depth: the deep system (1300 to 1000 m depth), the mid system (1000 to 600 m depth), and the shallow system (600 to 0 m depth).

Copper concentrations in VB35 FIAs in the deep system are variable and range from 0.6 to 5900 ppm Cu (Figure 41). A single VB35 inclusion contains 0.6 ppm Cu, while a nearby VB35 FIA averages 5900 ppm Cu. In the mid system, Cu concentrations in VB35 FIAs have averages that range from 12 to >14000 ppm, but most FIAs average a few thousand ppm Cu (1500 – 4200 ppm). In general, the highest Cu concentrations determined for VB35 FIAs are found in the mid system, though these concentrations are quite variable. Copper concentrations are significantly lower in VB35 FIA averages in the shallow system, where FIAs range from 125 to 2635 ppm. Five of six FIAs averaged less than 850 ppm; the lowest average Cu concentration in an FIA was 125 ppm. A single FIA averaged a Cu concentration of about 2600 ppm.

Due to the lack of suitable FIAs to analyze, no VB20H FIAs were analyzed from the deep system. Average FIA Cu concentrations from the mid system range from 519 to 24106 ppm (Figure 42). Four FIAs originating from the deeper portion of the mid system averaged between 500 and 1550 ppm, except for a single FIA that

contained an average Cu concentration in excess of 24000 ppm. In the higher part of the mid system, Cu concentrations were higher, averaging 2200 to 5500 ppm. Average Cu concentrations in VB20H FIAs from the shallow system range from 170 to 50643 ppm. VB20H FIAs near the high center of the intrusive complex have the highest average Cu concentrations detected in all VB20H inclusions, with five FIAs averaging between 11700 and 50600 ppm. Average Cu concentrations were significantly lower in two FIAs with average Cu concentrations of 460 and 7800 ppm. VB20H FIAs from the intrusion flanks have average Cu concentrations as low as 170 ppm, and averages as high as 6300 ppm.

Due to the lack of suitable FIAs to analyze, no VB60 FIAs from the deep part of the system were analyzed. Average FIA Cu concentrations from VB60 FIAs from the mid system range from 0.08 to nearly 12000 ppm (Figure 43). The four deepest FIAs have higher average Cu concentrations of 1400, 4600, 9500, and 12000 ppm, whereas the shallower FIAs all have average Cu concentrations below 370 ppm, with the exception of two FIAs with average concentrations of 5200 ppm and 7400 ppm. In the shallow part of the system, an FIA from the deep left flank has an average Cu concentrations of 39 ppm, while the upper right flank has one analyzed FIA, with an average Cu concentration of 6700 ppm.

VB85 FIAs have the lowest overall average Cu concentrations, and only samples from the shallow system were analyzed. All samples have relatively low concentrations with FIA average Cu not exceeding 700 ppm (Figure 44). The highest average Cu concentrations (450 – 700 ppm) come from the central portion of the shallow system, whereas adjacent FIAs have Cu concentrations below 15 ppm.

<u>Copper concentrations and their relation to known Cu grades</u>

Figures 45 through 48 illustrate ore zones with whole rock Cu grades from drill core across the deposit, allowing Cu concentrations in inclusions fluids to be compared with Cu concentrations in the deposit. In general, moving from the deep system to the levels of the ore body in the higher part of the system, Cu concentrations in ore fluids decrease as Cu grades in the rock increase to > 0.50 wt%. Areas that contain elevated Cu concentrations in inclusion fluids typically coincide with areas of low Cu grade, typically less than 0.50 wt% Cu, within the rock, and vice versa, although VB20H inclusions show a somewhat different pattern.

VB35 FIAs with the highest average Cu concentrations are located below 900 m depth and have Cu assays that indicate less than 0.50 wt% Cu in the rocks; Cu concentrations in the fluids range from 0 to >14000 ppm, with more than half of FIAs averaging more than 1500 ppm Cu (Figure 45). Above 900 m depth, average Cu concentrations in VB35 FIAs are lower when compared to VB35 FIAs from the deep system, ranging from 125 to 2600 ppm, with all but one FIA averaging below 850 ppm Cu. These FIAs coincide with areas of >0.50 wt% Cu; one VB35 FIA with relatively low average Cu concentration of 350 ppm coincides with an area of >1.50 wt% Cu.

Copper concentrations in VB20H FIAs and inclusions are elevated throughout the deposit when compared to other fluid inclusion types; however, FIA Cu concentrations are consistently higher above 900 m, where Cu grades, based on whole rock assay, are above 0.50 wt%. This pattern is different from that observed for VB35 FIAs. The deepest FIAs comprised of VB20H inclusions originate from

51

between 900 and 1000 m depth, and coincide with Cu grades of <0.50 wt% according to whole rock assays (Figure 46). These VB20H FIAs, from between 900 an 1000 m dept, have variable average Cu concentrations that range from 520 to 24000 ppm; three VB20H FIAs have average Cu concentrations of 520, 1515, and 1550 ppm, while another VB20H FIA has an average Cu concentration of over 24000 ppm. Above 900 m depth, average Cu concentrations in VB20H FIAs are generally higher than FIAs from below 900 m. Average Cu concentrations in these FIAs range from 170 to above 50000 ppm, with all but five FIAs averaging more than 5000 ppm Cu. The locations of these FIAs generally coincide with Cu grades of >0.50 wt%, and commonly coincide with areas of >1.50 wt% Cu.

VB60 FIAs show a similar pattern as VB35 FIAs, where high average Cu concentrations in FIAs coincide with areas of low Cu grades, and low average Cu concentrations in FIAs coincide with high Cu grade in the rock. The highest average Cu concentrations in VB60 FIAs are found below 900 m depth, and coincide with areas of <0.50 wt% Cu (Figure 47). Average Cu concentrations from VB60 FIAs from below 900 m depth ranged from 1400 to 12000 ppm, with three FIAs averaging >4600 ppm Cu. Above 900 m, average Cu concentrations in VB60 FIAs are noticeably lower; average Cu concentrations reach 7400 ppm, but averages in most FIAs are below 400 ppm.

VB85 FIAs have average low Cu concentrations, whereas Cu grades from whole rock assays are generally high. All VB85 FIAs that were analyzed by LA-ICP-MS were sampled from <600 m depth, and all FIAs have average Cu concentrations <700 ppm (Figure 48). The location of all VB85 FIA samples coincides with areas of

>0.50 wt% Cu grade. Two FIAs with average Cu concentrations of 0.97 and 63.3 ppm coincide with areas containing >1.50 wt% Cu.

In VB35, VB60, and VB85 type inclusions, an inverse relationship is observed between Cu concentration within ore fluids and Cu grade based on whole rock assay; where Cu concentration in the fluid is high, Cu grade in the rock is low, and vice versa. This relationship suggests a link between ore fluids responsible for the transport of Cu and Cu grades found in the rocks of Batu Hijau. A majority of Cu remained dissolved while these fluids were deep in the system, and this Cu was transported into the shallow part of the system where precipitation occurred. The pattern of Cu distribution in VB20H inclusions differs from the pattern observed in the other types of fluid inclusions. In VB20H inclusions Cu concentrations generally increase as the fluid moves up through the system; however, Cu concentrations are significant throughout the system. This suggests that a large amount of Cu was transported in VB20H fluids, enough to precipitate significant amounts of Cu within the rocks while still transporting Cu dissolved in ore fluids.

<u>Absence of Au in LA-ICP-MS results</u>

While Batu Hijau is known to produce a large amount of Au alongside Cu, Au is seemingly absent from the ore fluids based on LA-ICP-MS analyses of both fluid inclusion and solid Cu-Fe sulfide minerals. Gold was detected in a single VB35 inclusion at a concentration of 1.14 ppm, Au was below detection limits in all other analyses. The question arises: based on known Cu and Au grades and limits of detection, should Au be detected in the fluids? Based on an average bulk grade of

0.53 % Cu and 0.40 g/t Au (Garwin, 2002; Arif and Baker, 2004), Cu and Au were ratio'd to get a bulk Cu/Au ratio in ppm. Using this ratio and the average Cu concentration of 2695 ppm in VB35 inclusions, a theoretical average Au concentration of 0.20 ppm was calculated for VB35 inclusions. Limits of detection for Au varied for every LA-ICP-MS analysis; however, most limits of detection for Au were at or above the calculated theoretical Au concentration. The similarity between these limits of detection and the relatively low theoretical Au concentration may explain why Au was only rarely detected in the fluids from Batu Hijau.

CHAPTER 8

MODEL FOR DEPOSIT FORMATION

Two compositionally similar fluids associated with the emplacement of Pliocene tonalites at the center of the Batu Hijau system have been identified. Based on reconstructed trapping temperatures and elemental concentrations, primarily those of Cu, the first fluid pulse was trapped by VB60 inclusions found throughout the deposit. A second, cooler and denser but compositionally similar fluid was initially trapped in VB35 inclusions and subsequently separated into immiscible vapor and brine that were trapped in VB85 and VB20H inclusions, respectively. The relationship between the two fluids is not completely understood, but it is hypothesized that the two fluids are genetically related based on their similar elemental compositions derived from SXRF and LA-ICP-MS analyses. Based on elevated fluid temperatures, consistent Cu concentrations, and the general non-reactivity of metals, the fluid trapped by VB60 inclusions is interpreted to be the earlier of the two fluids.

Due to the lack of primary inclusions large enough for quantitative analysis, and the ambiguity of most crosscutting relationships, these fluids have not been linked to a specific tonalite intrusion. Previous workers (Clode et al., 1999; Proffett, mine report, 1999; Garwin, 2000, 2002) noted that elevated Cu and Au are spatially associated particularly with the old tonalite, but also with the intermediate tonalite, and the majority of Cu and Au mineralization is likely related to these two intrusive events.

Fluid 1: VB60 Inclusions

High temperature, low density fluids trapped by VB60 inclusions exsolved from a crystallizing intrusion and flooded the ore system. Homogenization temperatures in VB60 inclusions are the highest relative to all other inclusions types with the lowest recorded minimum temperature being 385 °C; minimum homogenization temperatures for VB60 inclusions were recorded up to 500 °C. These temperatures are minimum temperatures, as homogenization temperatures in vapor-rich inclusions can be underestimated by up to 500 °C (Sterner, 1992). Such high temperature fluids would have accompanied and perhaps have been responsible for, early high temperature potassic alteration in the central part of the intrusive system. Although X-Y plots indicated that all elements in VB60 inclusion fluids were non reactive, the K/Na plot does did show some variability for K.

Generally high Cu concentrations along with the high homogenization temperatures in VB60 inclusions support the interpretation that these fluids were early and part of the ore system. Most VB60 inclusions contain >1000 ppm Cu, many inclusions contain >4500 ppm Cu, and in some inclusions Cu concentrations approach 12000 ppm. The highest Cu concentrations in VB60 fluid inclusions coincide with areas of low Cu grade based on Newmont whole rock assay. In these areas, Cu concentrations in inclusions based on LA-ICP-MS analyses show that Cu remained dissolved in the ore fluid as quartz precipitated and trapped VB60 fluid inclusions. This pattern is observed throughout the deposit. The apparent lack of Cu precipitation from this fluid is likely due to the high temperatures of fluids, but

could also be a result of a decrease in porosity and permeability as quartz precipitated and formed veins. The lowest homogenization temperature determined for VB60 inclusions at Batu Hijau is just below the ideal temperature of Cu precipitation observed at Bajo de la Alumbrera (400 °C), while most homogenization temperatures exceed this temperature (Ulrich et al., 2002; Heinrich, 2003).

Of 18 pairs of elements evaluated with X-Y plots, R^2 values approaching 1.00 exist for all but two. This suggests that almost all elements, including Cu, were non reactive and remained dissolved within the VB60-forming ore fluid, and fluid-rock reactions and precipitation of elements from the fluids were minimal. R^2 values for Cu, however, are slightly lower than R^2 values for other elements including base metals and typical salt cations, suggesting that some Cu may have been lost to veins, while the majority of Cu remained dissolved in the ore fluid.

Fluid 2: VB35, VB20H, and VB85 Inclusions

A second fluid that was modified by changes in system pressure and temperature was trapped by three inclusion types: VB35, VB20H, and VB85. The second fluid, initially trapped by VB35 inclusions, encountered conditions that led to immiscibility and the fluid separated to form brine, trapped by VB20H inclusions, and vapor, trapped by VB85 inclusions (Figure 49).

Based on cooler fluid temperatures, high Cu concentrations, and evidence for increased fluid-rock reaction and metal precipitation, this second fluid is interpreted to have been the main ore-forming fluid at Batu Hijau. In the deepest

part of the system, between 1300 and 850 m depth, trapping temperatures for VB35 inclusions are between 120 and 250 °C cooler than minimum homogenization temperatures for VB60 inclusions. Because homogenization temperatures may have been underestimated by as much as 500 °C (Sterner, 1992) for VB60 inclusions, the temperature difference between these two fluids may have been even greater. A significant temperature change is observed in VB35 inclusions at around 850 m depth. VB35 trapping temperatures above this elevation are on average 50 °C lower than VB35 inclusions from below this depth; in some inclusions, this difference in trapping temperature can be as much as 120 °C.

R^2 values from LA-ICP-MS analyses for VB35 inclusions were highly variable, indicating that some elements were reactive while others were not. Manganese, Zn, and Pb, were non-reactive and remained dissolved in the VB35 fluids during transport. Consistent base metal compositions are also evident in all inclusions analyzed by SXRF, which shows strong correlations between Mn, Pb, and Zn. These base metals likely remained dissolved in the ore fluids to be precipitated at cooler temperatures and shallower depths in the base metal deposits that are observed within the Batu Hijau mining district (Garwin, 2000). Potassium, Ca, Fe and Cu are reactive, suggesting that these elements reacted with wall rocks and precipitated or were scavenged by the fluid to varying degrees. Potassium and Fe likely took part in wall rock reactions to form K feldspar, biotite, and sericite, and to precipitate Fe-bearing sulfides, respectively. Calcium was probably scavenged from wall rocks as primary plagioclase feldspars were altered. The reactivity of Cu is likely due to Cu

precipitation associated with the formation of Cu-Fe sulfides such as chalcopyrite, bornite, and diginite.

Deposit wide immiscibility of the VB35 fluid to form the VB20H brine and VB85 vapor phases appears to be depth-controlled, and occurred dominantly at a depth of about 850 m below the surface. While all inclusion types can be found throughout the entirety of the deposit, there is a significant change at this depth, characterized by a transition from VB35-dominated inclusions below 850 m, to VB20H- and VB85-dominated inclusions above 850 m in A and AB veins. This distribution suggests that the buoyant VB35 fluid became immiscible largely due to decreasing pressure during upward migration through the system. The consistent depth of immiscibility suggests that decreasing pressure was the primary cause of immiscibility as the fluid rose. This interpretation is more likely than immiscibility in response to depressurization from local fracturing events across the deposit, which would not be related to a single depth.

Figure 49 shows a H_2O-NaCl phase diagram illustrating the approximate pressure, temperature, and salinity conditions for fluids from each inclusion type at Batu Hijau, with VB60's shown in orange, VB35's shown in red, and VB20H's shown in green, with error bars representing the variability in salinity. A range of pressure, temperature, and salinity conditions occur for all inclusion types, so the position of each point represents average conditions for the bulk of fluids and represents a possible fluid evolution pathway.   VB60 fluids, with minimum trapping temperatures of about 400 °C, are plotted at the base of a line extended up to a theoretical maximum trapping temperature of about 1000 °C (Sterner, 1992). A

second pathway exhibits a decrease in temperature and pressure for VB35 fluids shown by the red arrow.   Depressurization of the VB35 fluid led to immiscibility and the formation of VB20H and VB85 inclusions; the difference in density and salinity between these two inclusion types is represented by the location of the VB20H fluid and a dashed green line extending toward the location of VB85 fluids. VB85 inclusions were not plotted on this figure due to their existence at conditions that are outside the realm of currently available experimental data.

The immiscibility of VB35 fluids formed fluids trapped by VB20H and VB85 inclusions that differ greatly from one another. VB85 inclusions were Cu-poor, and analyses indicated <700 ppm Cu in these fluids in the deposit. Conversely, VB20H inclusions contained abundant Cu, and were relatively enriched in Cu above the 850 m immiscibility horizon when compared to VB20H inclusions from below 850 m depth; high Cu concentrations in VB20H fluids coincide with areas of high Cu grade based on whole rock assay, contrasting in the pattern observed for VB35 inclusions. Significant cooling of VB20H fluids is not observed, with all trapping temperature falling between 315 and 400 °C. This temperature range is equal to and below the temperature at which Cu precipitation occurred at within the Bajo de la Alumbrera deposit (Ulrich et al., 2002 Heinrich, 2003). As the ratio of the generated volume of liquid to vapor is not known, the amount of Cu transported by each subsequent phase cannot be determined.

Fluid compositions in VB20H inclusions are variable when compared to the compositionally non-reactive fluid that was fluid trapped by earlier VB60 inclusions, and generally mirror VB35 fluids with respect to the reactivity of elements during

transport. R^2 values for VB20H inclusions are slightly lower than for VB35 inclusions, suggesting a fluid that is somewhat more reactive than its parental VB35 fluid, especially with respect to Cu. Similar to VB35 fluids, Mn, Zn, and Pb in the VB20H brine are non-reactive, suggesting these elements did not precipitate during transport through the system. Potassium, Ca, Fe, and Cu are all reactive, suggesting that these elements were part of wall rock reactions and precipitation; K, Ca, and Fe were likely part of wall rock reactions responsible for the formation of sericite, K feldspar, and biotite, the scavenging of Ca from altering plagioclase feldspars, and the precipitation of Fe-bearing sulfide minerals, respectively, while Cu precipitated in Cu-Fe sulfides.

R² values for VB85 inclusions indicate a fluid that is compositionally consistent, and generally mirrors VB60 fluids with respect to reactivity. This fluid was relatively non-reactive and fluid-rock reaction did not cause significant metal precipitation; however, while Cu in VB85 fluids is largely non-reactive, the moderately high R^2 values suggest that some Cu was likely lost to precipitation of Cu-Fe sulfides.

CHAPTER 9

CONCLUSIONS

Ore fluids at Batu Hijau likely formed in two stages. An initial high temperature, compositionally consistent fluid precipitated only minor Cu and was trapped in VB60 fluid inclusions. This fluid was followed by a cooler, denser, but compositionally similar fluid that was much more reactive and contributed significantly to wall-rock reaction and mineral precipitation, and was responsible for the formation of VB35 inclusions. This second fluid became immiscible during its ascent toward the surface, resulting in the formation of brine and vapor phases, trapped by VB20H and VB85 inclusions, respectively. This brine phase mirrors the reactivity of its parental VB35-forming fluid, and it is likely that these two fluids were responsible for the bulk of Cu precipitated at Batu Hijau.

Table 1. LA-ICP-MS instrument and data parameters

Excimer 193–nm ArF laser GeoLasPro	
Output Energy	150 mJ
Energy Density on sample	$\sim 7-10$ J/cm^2
Repetition Rate	5 Hz
Pit Size	Between x and x ⬚m
Ablation Cell Volume	~ 1.5 cm^3
Cell Gas Flow (He)	~ 1 L/min

Agilent 7500ce quadrupole ICP–MS	
Auxiliary gas flow	1.03 l/min Ar
RF power	1500 V
Detector Mode	Dual 8 orders of magnitude linear dynamic range
Quadrupole Settling Time	2 ms

Data acquisition parameters	
Sweeps per reading	1
Reading per replicate	$200-300$
Replicates	1
Dwell time per isotope	10 ms
Points per peak	1 per measurement
External Standard	NIST610 glass

Table 2. Calculated trapping temperatures for VB35 inclusions

Drill Hole	FIA	Temp (°C)	Drill Hole	FIA	Temp (°C)	Drill Hole	FIA	Temp (°C)
SBD265 1341.8	BH001	390	SBD257 905.7	FIA062-1	386	SBD21 500.3	FIA055-3	284
SBD265 1341.8	BH002	396	SBD257 905.7	FIA062-2	274	SBD21 500.3	FIA055-4	296
SBD265 1341.8	BH003	396	SBD257 905.7	FIA062-3	286	SBD21 500.3	FIA055-5	297
SBD265 1341.8	FIA020-1	286	SBD257 905.7	FIA062-4	387	SBD14 433.1	FIA013-1	301
SBD265 1341.8	FIA020-2	288	SBD257 905.7	FIA062-5	386	SBD14 433.1	FIA013-2	290
SBD265 1341.8	FIA020-3	293	SBD257 905.7	FIA063-1	274	SBD14 433.1	FIA013-3	276
SBD265 1341.8	FIA020-4	287	SBD257 905.7	FIA063-2	275	SBD14 433.1	FIA013-4	302
SBD265 1341.8	FIA021-1	367	SBD257 905.7	FIA063-3	270	SBD14 433.1	FIA013-5	286
SBD265 1341.8	FIA021-2	350	SBD257 905.7	FIA063-4	276	SBD21 484.9	FIA007-1	298
SBD265 1341.8	FIA021-3	360	SBD257 905.7	FIA063-5	269	SBD21 484.9	FIA007-2	299
SBD265 1341.8	FIA021-4	358	SBD257 905.7	FIA067-1	278	SBD21 484.9	FIA007-3	299
SBD265 1341.8	FIA021-5	334	SBD257 905.7	FIA067-2	281	SBD21 484.9	FIA007-4	321
SBD265 1341.8	FIA021-6	347	SBD257 905.7	FIA067-3	376	SBD21 484.9	FIA007-5	319
SBD265 1341.8	FIA021-7	353	SBD257 905.7	FIA067-4	377	SBD21 484.9	FIA007-6	309
SBD257 853.1	FIA042-2	370	SBD257 905.7	FIA067-5	376	SBD21 484.9	FIA007-7	314
SBD257 853.1	FIA043-1	324	SBD257 905.7	FIA067-6	380	SBD21 484.9	FIA007-8	318
SBD257 853.1	FIA044-2	380	SBD257 905.7	FIA067-7	375	SBD15 480.2	FIA056-1	324
SBD257 853.1	FIA047-1	371	SBD257 905.7	FIA067-8	382	SBD15 480.2	FIA057-1	287
SBD257 853.1	FIA047-2	384	SBD257 905.7	FIA067-10	380	SBD15 480.2	FIA057-2	292
SBD257 853.1	FIA047-3	382	SBD257 905.7	FIA067-11	375	SBD15 480.2	FIA057-3	293
SBD257 853.1	FIA047-4	381	SBD49 655.8	FIA027-1	285	SBD15 480.2	FIA057-4	285
SBD257 853.1	FIA047-5	382	SBD49 655.8	FIA027-2	294	SBD15 480.2	FIA057-5	286
SBD257 853.1	FIA047-6	386	SBD49 655.8	FIA027-3	296	SBD15 480.2	FIA057-6	294
SBD257 853.1	FIA047-7	382	SBD49 655.8	FIA027-4	295	SBD15 480.2	FIA058-1	303
SBD257 853.1	FIA050-1	382	SBD49 655.8	FIA027-5	295	SBD15 480.2	FIA058-2	300
SBD257 853.1	FIA050-2	380	SBD49 655.8	FIA027-6	295	SBD15 480.2	FIA058-3	301
SBD257 853.1	FIA050-3	382	SBD49 540.2	FIA036-1	261	SBD15 480.2	FIA058-4	314
SBD257 853.1	FIA050-4	381	SBD49 540.2	FIA036-2	261			
SBD257 853.1	FIA050-5	381	SBD49 540.2	FIA036-3	263			
SBD257 853.1	FIA050-6	382	SBD49 540.2	FIA036-4	265			
SBD257 853.1	FIA050-7	382	SBD49 540.2	FIA036-5	375			
SBD257 853.1	FIA050-8	328	SBD49 540.2	FIA036-6	281			
SBD257 905.7	FIA061-1	248	SBD49 540.2	FIA036-7	280			
SBD257 905.7	FIA061-2	248	SBD49 540.2	FIA036-8	270			
SBD257 905.7	FIA061-3	248	SBD21 500.3	FIA055-1	300			
SBD257 905.7	FIA061-4	248	SBD21 500.3	FIA055-2	300			

6

Table 3. Calculated trapping temperatures for VB20H inclusions

Drill Hole	FIA	Temp (°C)
SBD257 853.1	FIA029-3	370
SBD257 853.1	FIA049-1	354
SBD257 853.1	FIA049-2	340
SBD257 853.1	FIA049-3	350
SBD257 905.7	FIA064-1	347
SBD257 905.7	FIA064-2	355
SBD257 905.7	FIA064-3	349
SBD257 905.7	FIA064-4	335
SBD86 781.4	FIA023-1	397
SBD86 781.4	FIA023-3	359
SBD86 781.4	FIA023-2	373
SBD86 781.4	FIA023-4	315
SBD86 781.4	FIA025-1	324
SBD86 781.4	FIA025-2	324
SBD86 781.4	FIA025-3	335
SBD86 781.4	FIA025-4	335
SBD86 781.4	FIA025-5	329
SBD86 781.4	FIA025-6	318
SBD86 781.4	FIA025-7	323
SBD49 635.1	FIA038-1	316
SBD49 540.2	FIA034-1	381
SBD14 449.9	FIA006-1	340
SBD21 500.3	FIA054-1	355

Table 4. Summary of LA-ICP-MS Data

		ppm B	ppm Na	ppm K	ppm Ca	ppm Mn	ppm Fe	ppm Cu	ppm Zn	ppm As
VB35	low	-	0.67	0.18	7.11	0.04	0.41	0.60	0.02	-
	high	0.02	74386.39	37145.51	10632.98	5439.34	17453.88	20858.34	3054.18	-
	average	-	12877.02	3374.59	1357.90	1330.17	2927.26	2696.25	763.37	-
	median	-	6477.32	601.23	248.95	824.69	673.46	407.24	252.67	-
VB20H	low	63.42	1054.04	1194.93	55.20	699.07	41.34	37.03	172.39	-
	high	448.62	176387.93	127263.96	25937.48	29375.78	161505.70	143645.37	17280.10	25.59
	average	183.71	70367.04	32796.86	5295.36	10287.49	56470.27	11084.55	4559.20	-
	median	111.41	68750.84	26873.62	3324.39	8801.38	59151.79	2929.65	3718.26	-
VB60	low	0.00	0.32	0.04	0.01	0.01	0.06	0.05	0.01	-
	high	0.06	33941.80	4419.12	3130.38	2645.28	19462.67	19128.46	2008.86	-
	average	0.02	10352.69	1175.68	445.72	713.45	3139.01	3588.19	448.71	-
	median	0.00	5539.40	524.27	92.75	262.02	852.85	1699.68	341.49	-
VB85	low	0.00	0.04	0.13	0.01	0.00	0.09	0.17	0.02	-
	high	31.20	827.47	378.43	774.45	144.99	289.55	834.50	62.99	0.00
	average	7.24	247.04	74.38	227.17	20.80	69.75	240.66	18.90	-
	median	1.15	208.15	34.68	57.72	0.49	6.06	20.63	19.79	-

		ppm Rb	ppm Sr	ppm Mo	ppm Ag	ppm Ba	ppm W	ppm Au	ppm Pb
VB35	low	0.32	0.18	-	-	0.00	-	-	0.00
	high	5.32	132.50	0.00	-	116.31	-	1.14	229.76
	average	2.47	23.68	-	-	31.06	-	-	51.43
	median	2.10	5.64	-	-	14.99	-	-	19.29
VB20H	low	4.04	5.71	214.92	18.30	6.82	7.18	-	16.77
	high	765.34	350.41	148.61	28.78	5031.90	32.77	-	1314.97
	average	113.96	70.93	179.90	24.33	510.76	15.89	-	388.90
	median	78.61	54.34	176.17	25.13	275.45	11.80	-	364.94
VB60	low	0.00	0.00	-	-	0.00	-	-	0.00
	high	7.89	33.34	-	-	56.97	-	-	90.11
	average	3.95	7.83	-	-	18.98	-	-	33.18
	median	3.95	5.16	-	-	14.94	-	-	22.56
VB85	low	0.00	0.00	0.00	0.00	0.00	0.00	-	0.00
	high	0.35	7.81	0.52	0.00	5.48	0.07	-	3.21
	average	0.09	2.25	0.10	0.00	1.25	0.03	-	0.90
	median	0.01	0.75	0.01	0.00	1.12	0.02		0.05

Table 5. Summary of R² correlation coefficient values for element pairs in Figures 23 through 38

	VB35	VB60	VB85	VB20H
Ca-Na	0.12	0.75	0.93	0.74
Ca-K	0.17	0.89	0.75	0.22
Na-K	0.85	0.88	0.84	0.10
Zn-Fe	0.00	0.85	0.60	0.44
Mn-Fe	0.00	0.95	0.96	0.41
Mn-Zn	0.96	0.96	0.99	0.92
Mn-Pb	0.28	0.93	1.00	0.88
Mn-K	0.93	0.98	0.89	0.71
Cu-K	0.42	0.76	0.83	0.12
Cu-Ca	0.12	0.71	0.67	0.01
Cu-Mn	0.39	0.82	0.82	0.13
Cu-Zn	0.45	0.82	0.77	0.17
Cu-Fe	0.36	0.81	0.80	0.01
Cu-Pb	0.50	0.73	0.87	0.22
Cu-Ba	0.33	0.60	0.84	0.04
Cu-Na	0.24	0.51	0.48	0.20

0.00 - 0.34	Weak/No correlation
0.35 - 0.69	Moderate correlation
0.70 - 1.00	High correlation

Table 6. Ranges of ratios of elements to Na; elements are grouped according to element type, behavior, and abundance in analyzed inclusions

Group 1	Cu	Fe	Mn	Zn	Pb
Total Range	0.001 to 210	0.0007 to 13.0	0.002 to 6.5	0.002 to 2.0	0.0006 to 0.2
Mean Range	0.025 to 3	0.7 to 3.0	0.08 to 0.5	0.02 to 0.2	0.001 to 0.1
Range in:					
VB20H	0.004 to 3.5	0.0007 to 11.0	0.02 to 6.5	0.0095 to 2.0	0.001 to 0.2
VB35	0.001 to 10	0.02 to 11.0	0.04 to 6.5	0.008 to 2.0	0.0006 to 0.1
VB60	0.004 to 30	0.0015 to 13.0	0.002 to 0.9	0.002 to 0.85	0.0008 to 0.1
VB85	0.025 to 210	0.009 to 4.0	0.095 to 0.45	0.045 to 0.5	0.002 to 0.02

Group 2	K	Ca	Mo	Ag	Au
Total Range	0.008 to 9.5	0.00085 to 7.0	0.002 to 0.0075	0.0045 to 0.0008	-
Mean Range	0.2 to 0.95	0.02 to 1.0	-	-	-
Range in:					-
VB20H	0.09 to 9.5	0.0008 to 5.0	0.004 to 0.005	0.0005 to 0.00055	
VB35	0.08 to 7.0	0.015 to 9.0	0.0065	-	0.0001
VB60	0.008 to 1.0	0.005 to 1.0	-	-	-
VB85	0.05 to 8.0	0.07 to 3.0	0.002 to 0.0075	0.0004 to 0.00085	-

| Group 3	As	Ba	Sr	W	B	Li	Rb
Total Range	-	0.00007 to 0.18	0.000045 to 0.03	0.000095 to 0.0045	0.0009 to 0.06	0.0003 to 0.02	0.0005 to 0.07
Mean Range	-	0.001 to 0.02	-	-	-	-	-
Range in:							
VB20H	-	0.00007 to 0.18	0.00006 to 0.03	0.000095 to 0.0008	0.0009 to 0.04	0.0003 to 0.02	0.0006 to 0.07
VB35	-	0.0008 to 0.04	0.0004 to 0.0085	-	0.04 to 0.06	-	0.0005 to 0.001
VB60	-	0.00008 to 0.065	0.0015 to 0.015	-	0.0009 to 0.015	-	0.00095 to 0.001
VB85	0.006	0.001 to 0.07	0.0015 to 0.02	0.008 to 0.0045	0.0015 to 0.03	-	0.0008 to 0.0025
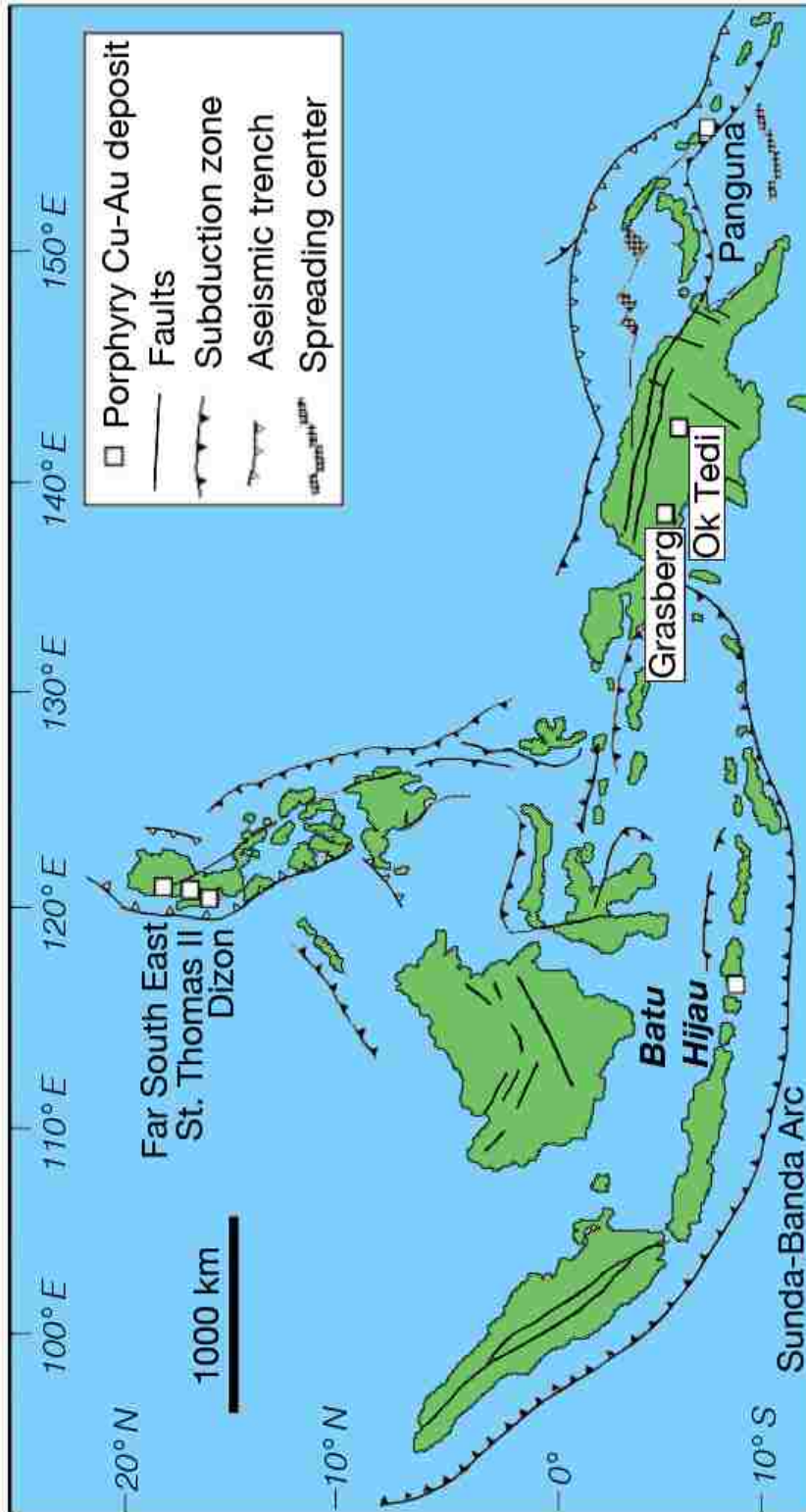
Figure 1 The location of Batu Hijau and other major porphyry Cu–Au deposits in Indonesia, Southeast Asia (modified from Corbett and Leach, 1998; Arif & Barker, 2004).
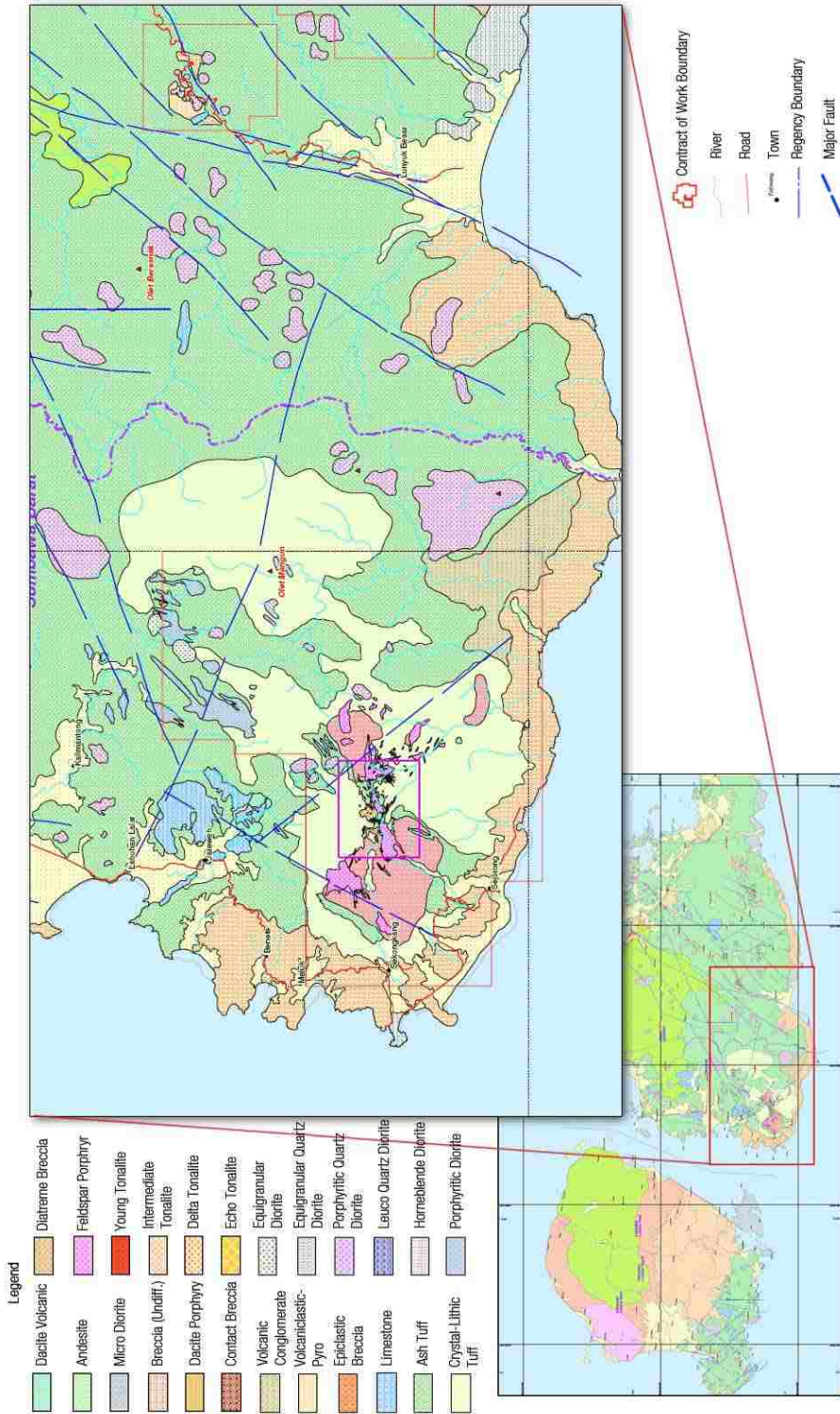
Figure 2 Geologic map of southwestern Sumbawa Island, Indonesia. The Batu Hijau mining district is contained within the smaller pink box (modified from PT Newmont Nusa Tenggara Regional Geology Map, 2005)
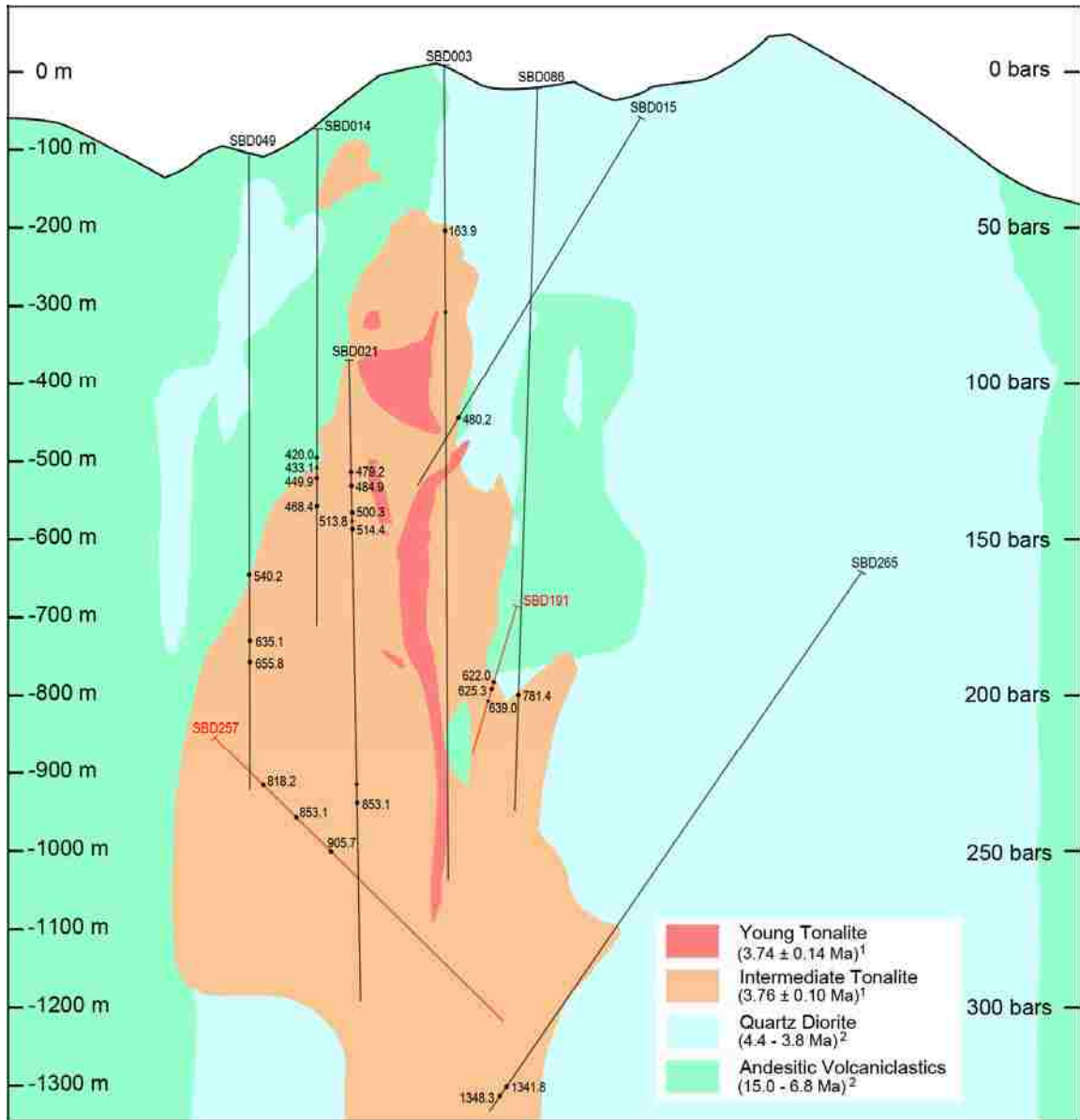
Figure 3 Simplified East-West geologic cross section through the Batu Hijau Deposit. Sampled drill holes are marked and labeled. Orientations of drill holes depicted in black are coincident with the orientation of the cross section. Drill holes depicted in red are approximate, as they have been projected into this section. Pressures assume lithostatic pressure. Rock unit ages are based on data from Fletcher et al., 2000[1]; Garwin, 2002[2] (modified from PT Newmont Nusa Tenggara, 2009).

71
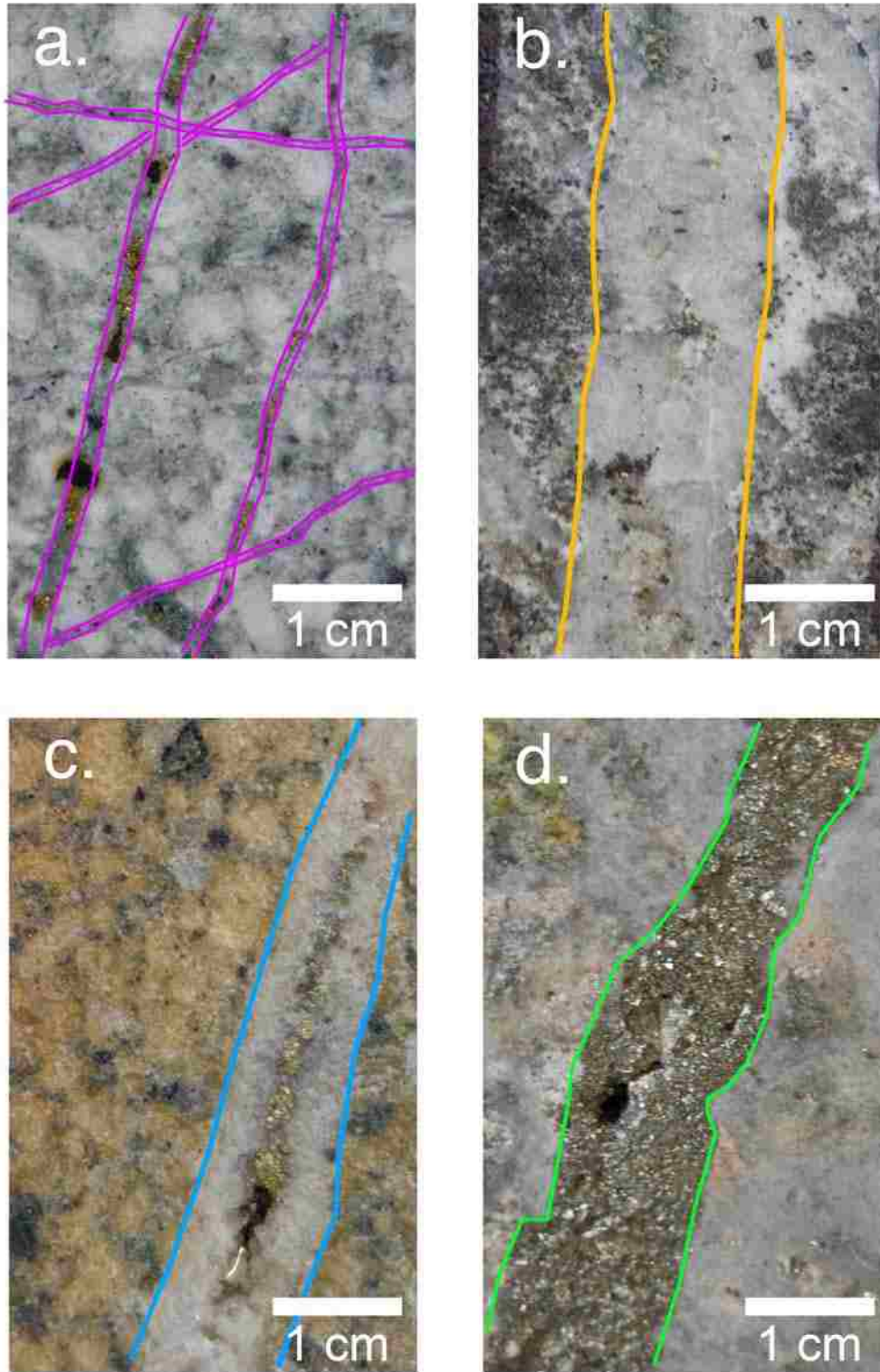
Figure 4 Various vein types in the Batu Hijau deposit. a. A veins containing quartz + chalcopyrite + magnetite, b. AB vein containing quartz + feldspar + chalcopyrite + bornite, c. B vein displaying characteristic centerline chalcopyrite mineralization, d. Pyrite.
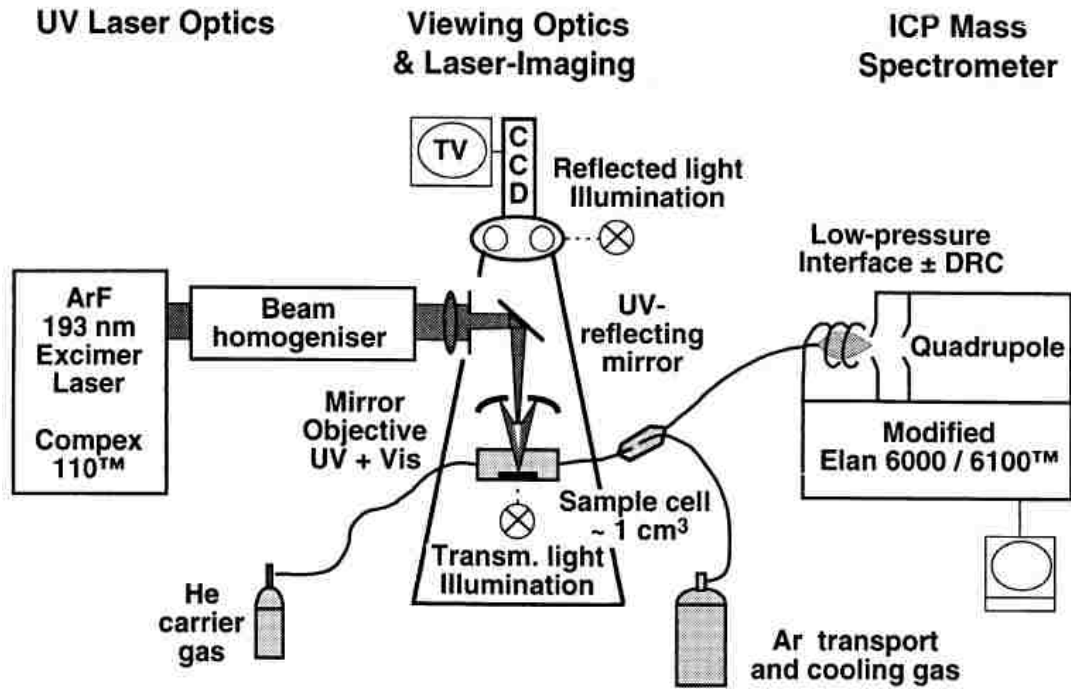
Figure 5 Schematic view of the LA-ICP-MS instrument developed at ETH Zürich, employed at the VT Fluids Research Lab (Heinrich et al., 2003).
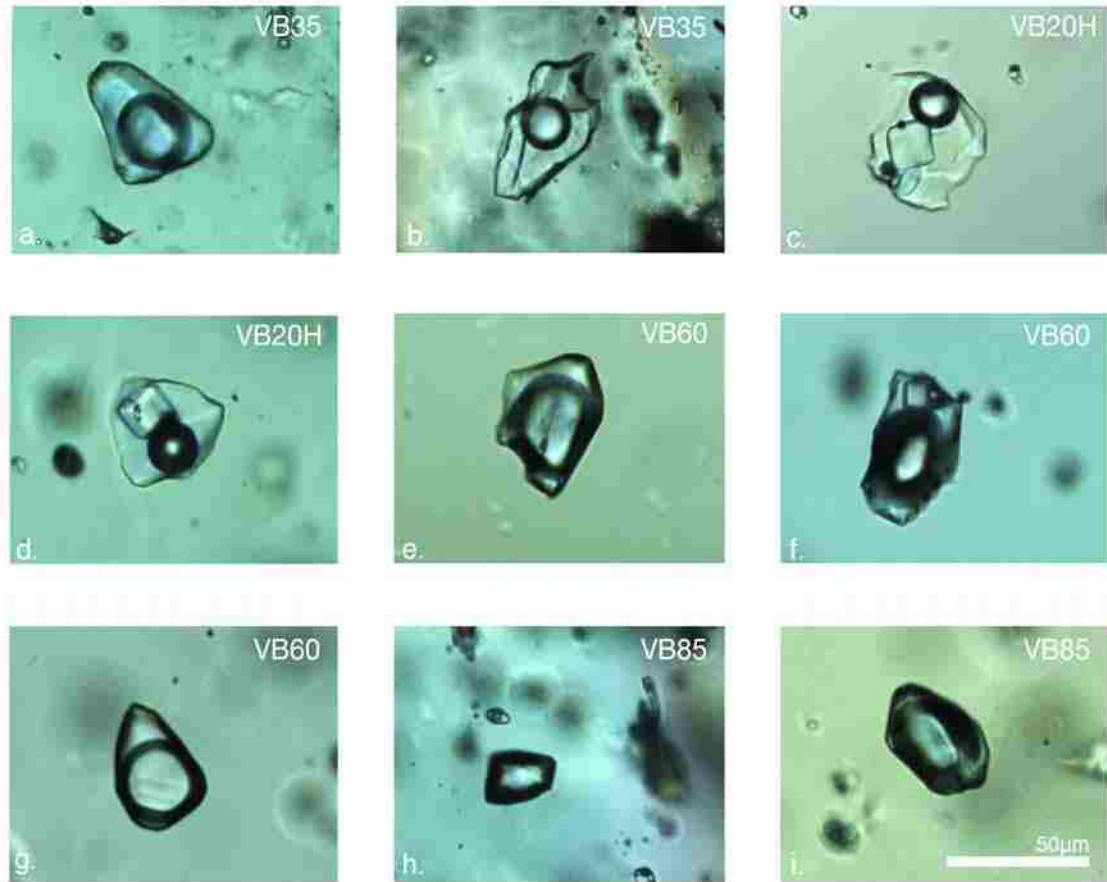
Figure 6 Photomicrographs of the various fluid inclusions found at Batu Hijau. a. VB35 inclusion with approximately 45 volume percent vapor bubble, b. VB35 inclusion with approximately 30 volume percent vapor bubble, c. VB20H inclusion with multiple daughter crystals including halite, sylvite, and two unidentified opaque daughter crystals, d. VB20H inclusion with large halite and smaller unknown opaque daughter crystal, e. VB60 inclusion with opaque daughter crystal, f. VB60 inclusion with halite and opaque daughter crystal, g. VB60 inclusion with no daughter crystals, h. VB85 inclusion with nearly 100 volume percent vapor bubble, i. VB85 inclusion with approximately 85 volume percent vapor bubble.
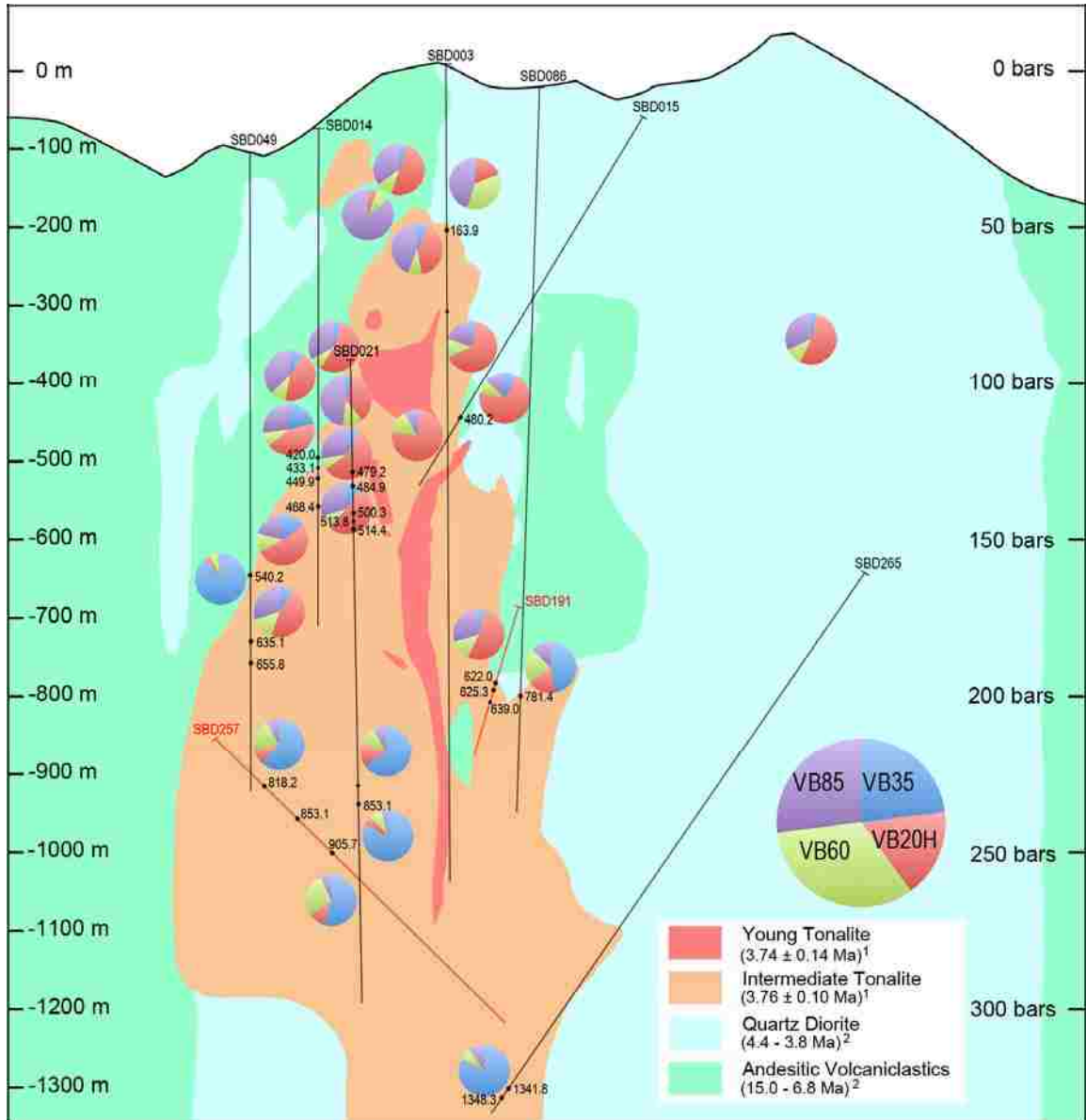
Figure 7 East-west cross section of the Batu Hijau deposit displaying relative abundances of fluid inclusion types in A & AB veins at various locations. Pie chart colors represent the four fluid inclusion types: VB35 (blue), VB20H (red), VB60 (green), and VB85 (purple). All abundances are normalized to 100%.
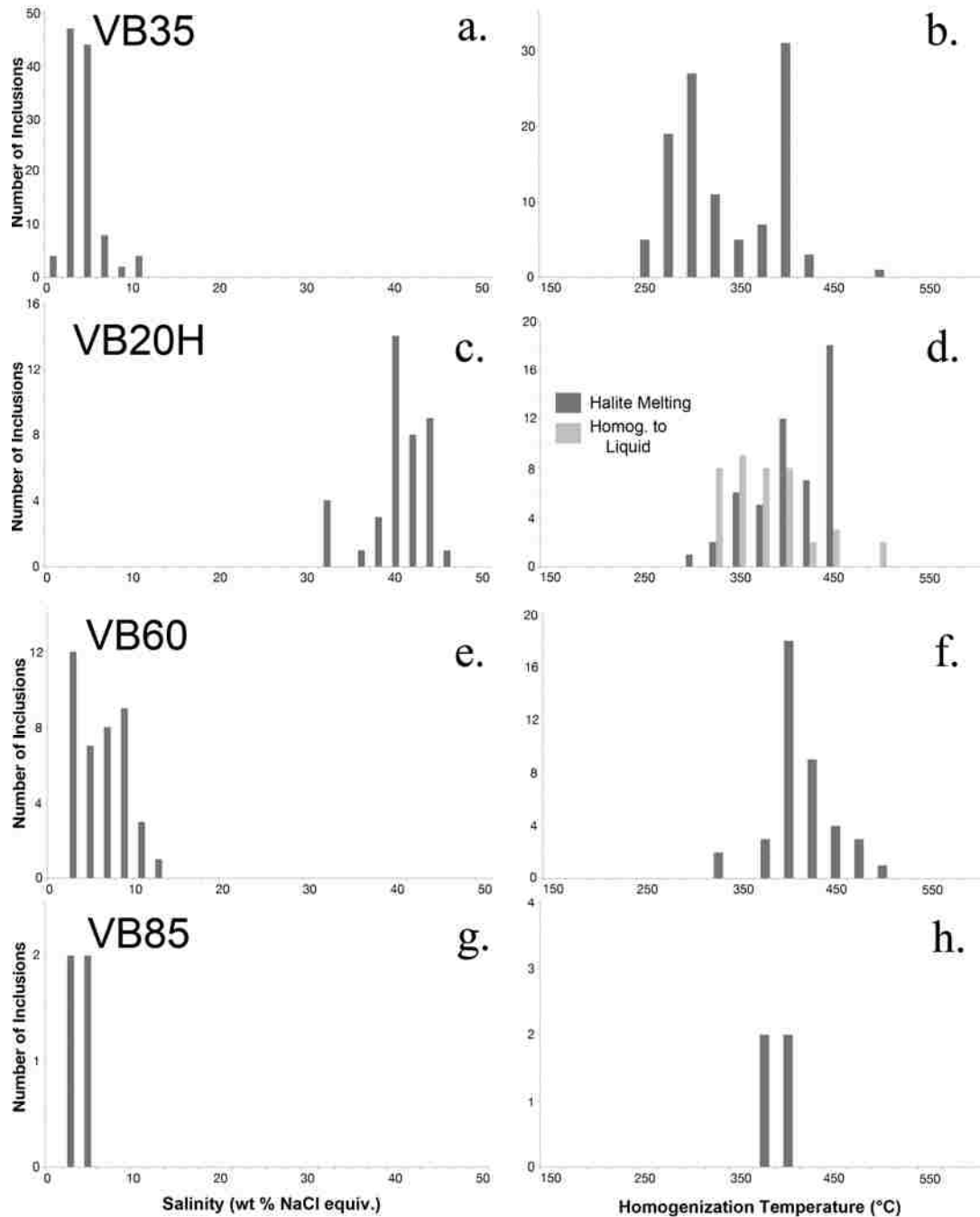
Figure 8 Stacked histograms for salinity in weight percent NaCl equivalent (left) and homogenization temperature (right) for each inclusion type: a. Salinities for VB35 inclusions, b. Homogenization temperatures to liquid for VB35 inclusions, c. Salinities for VB20H inclusions, d. Homogenization temperatures to liquid for VB20H inclusions. VB20H inclusions that homogenized by halite melting are shown in dark gray, and those that homogenized to liquid are shown in light gray, e. Salinities for VB60 inclusions, f. Minimum homogenization temperatures to vapor for VB60 inclusions, g. Salinities for VB85 inclusions, and h. Minimum homogenization temperatures for VB85 inclusions.
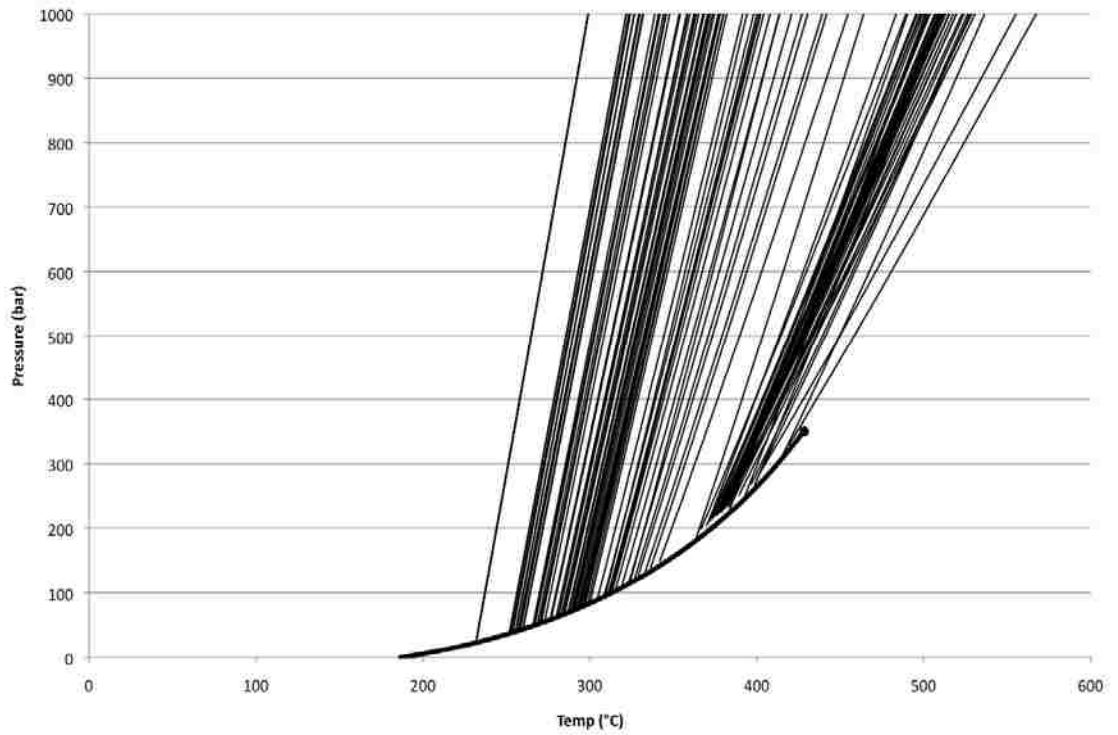
Figure 9 Constant density isochors for VB35 inclusions. Liquid-vapor curve is for a fluid of 5 weight percent NaCl equivalent. Individual black lines extending from liquid-vapor curve are isochors for individual VB35 fluid inclusions. The temperature at the base of each isochore is the homogenization temperature of each inclusion to liquid. The isochore represents a line of constant density and the inclusion could have been trapped anywhere along this line.
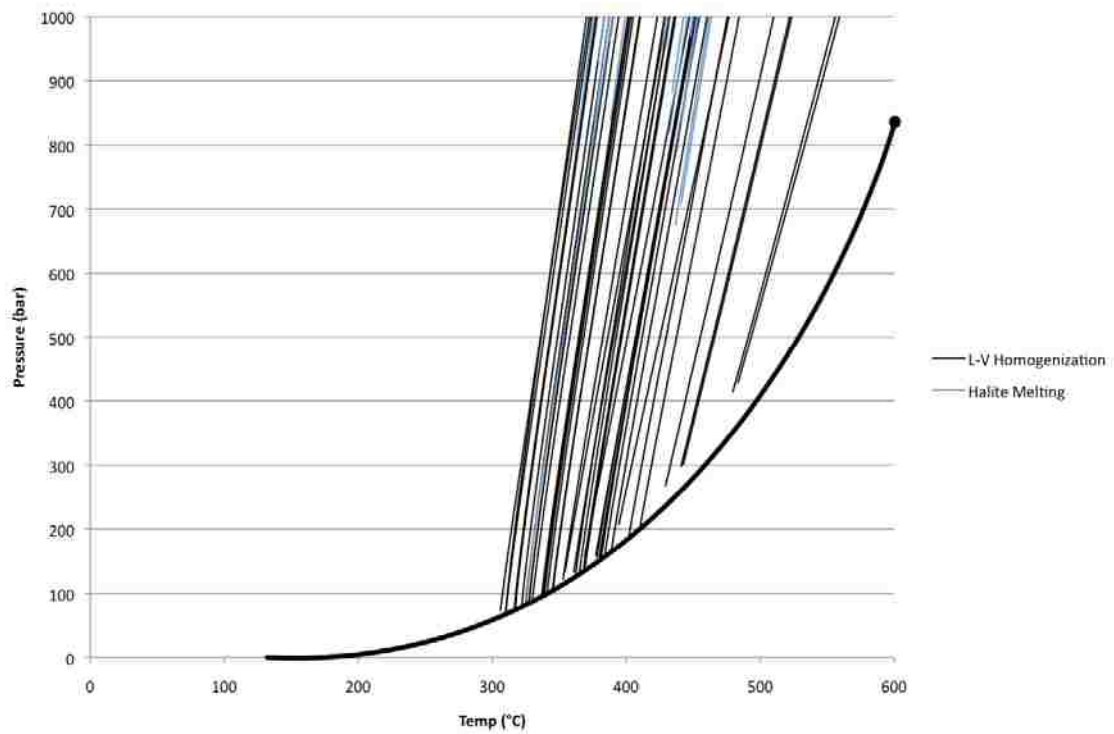
Figure 10 Constant density isochors for VB20H inclusions. Liquid-vapor curve is for a fluid of 45 weight percent NaCl equivalent. Individual isochors extending from liquid-vapor curve correspond to individual VB20H fluid inclusions. The temperature at the base of each isochore is the homogenization temperature of each inclusion to liquid. Inclusions are differentiated by mode of homogenization; inclusions homogenizing to liquid are in black, while inclusions homogenizing by halite melting are shown in blue. Isochors that do not meet the liquid-vapor curve have salinities other than 45 weight percent NaCl equivalent.
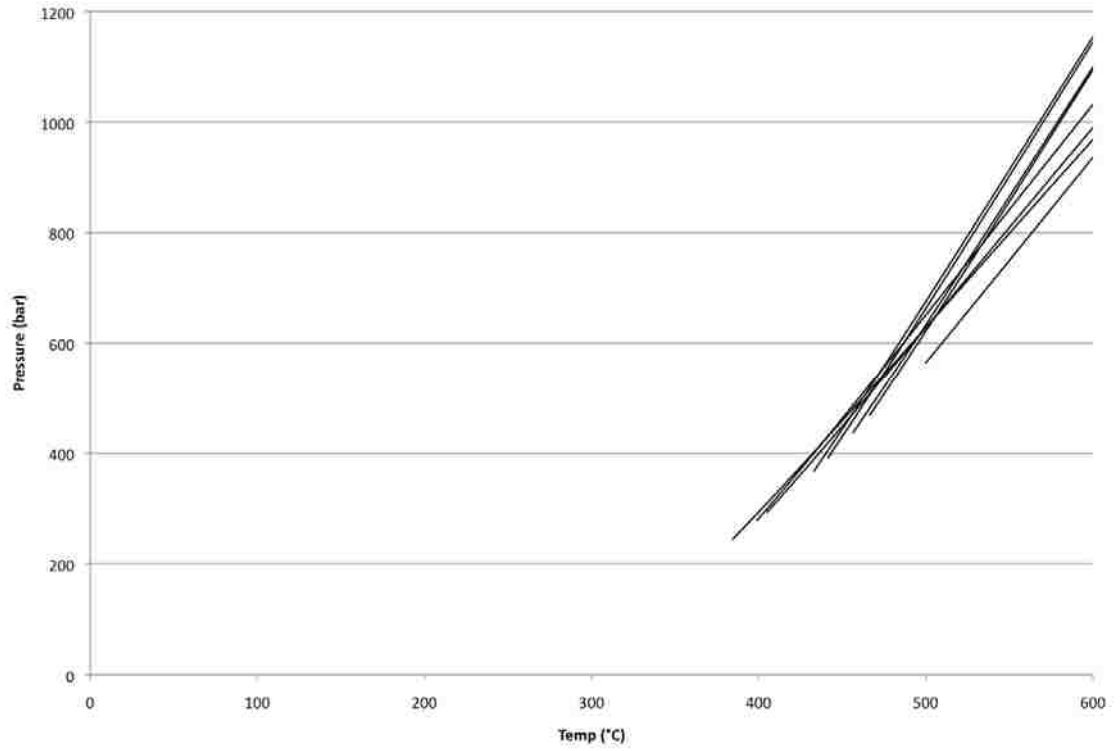
Figure 11 Constant density isochors for VB60 inclusions.   No liquid-vapor curve is shown. Individual isochors correspond to individual VB60 fluid inclusions. The temperature at the base of each isochore is the minimum apparent homogenization temperature of each inclusion to vapor.

79
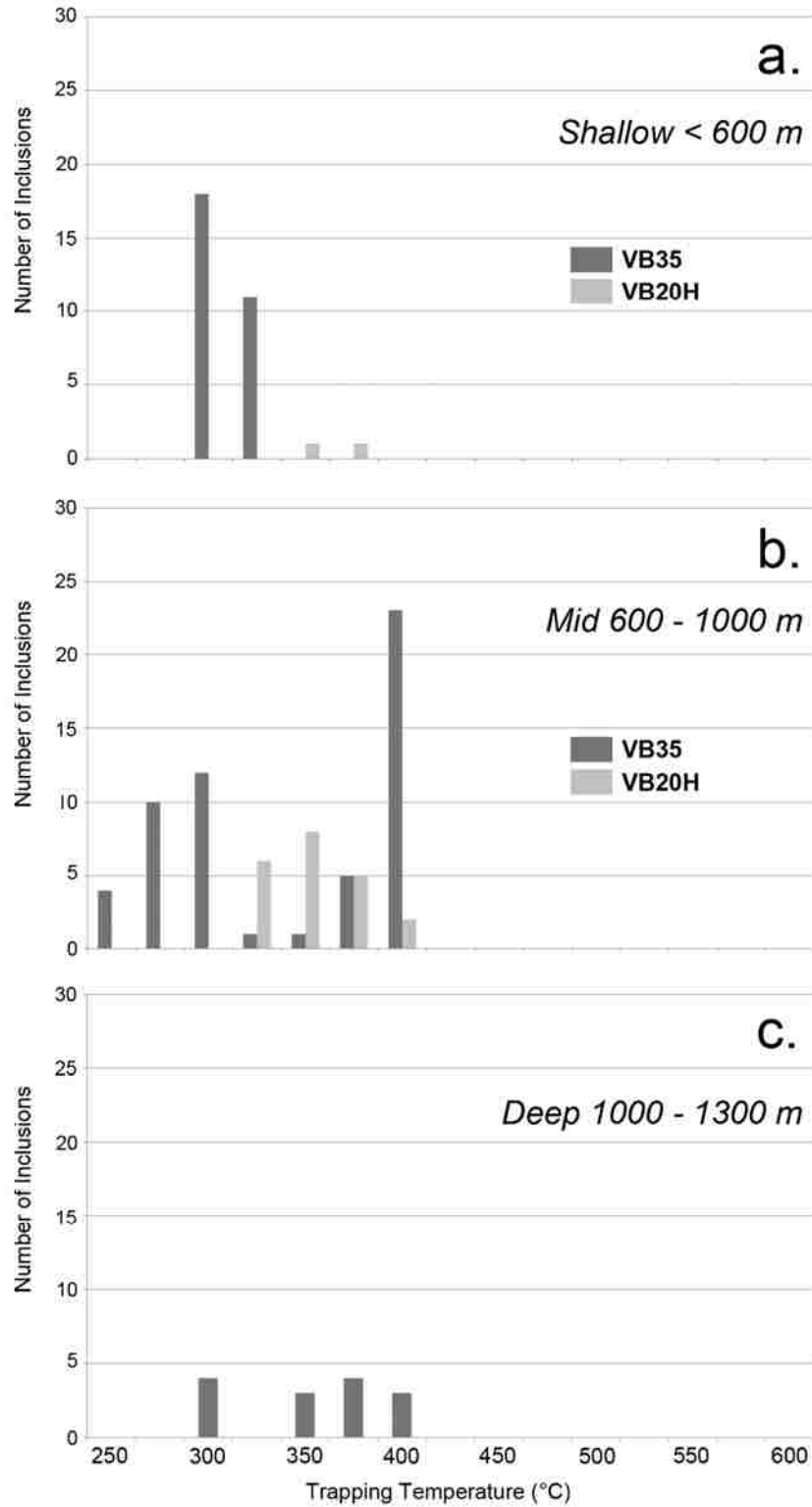
Figure 12 Approximate trapping temperatures for 99 VB35 and 23 VB20H inclusions.   Histograms are based on relative depth. a. Shallow system (<600 m), b. Mid system (1000 – 600 m) and, c. deep system (1300 to 1000 m).   Trapping temperatures are shown on the horizontal axis and were grouped in 25 ˚C intervals; frequency is plotted on the vertical axis.

80
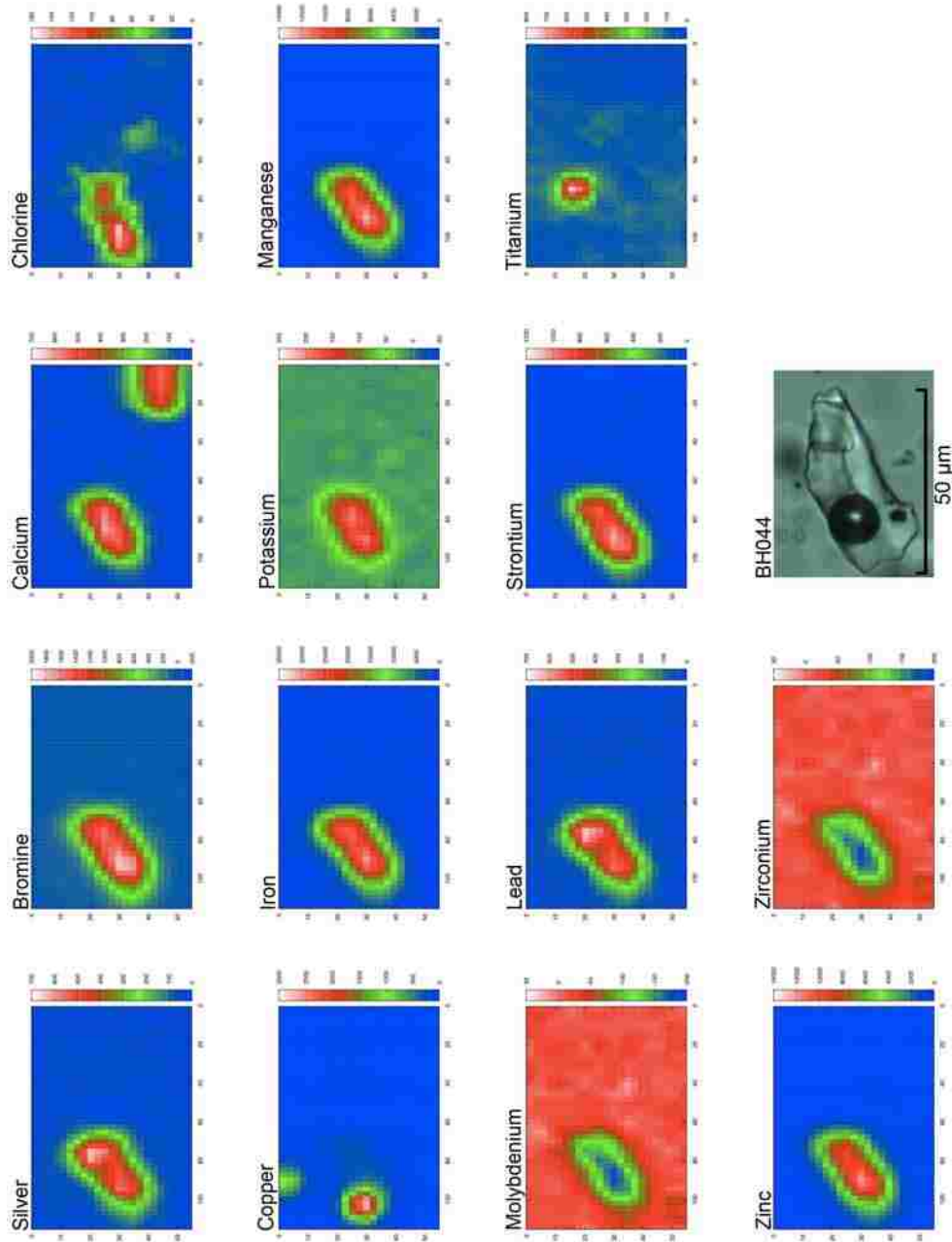
Figure 13 Elemental distribution maps for VB20H inclusion #BH044 exhibiting overlapping high relative concentrations of Cu and Fe, along with elevated abundances of Br, Mn, Zn, K, Pb, and Ti, among other elements. Note the elevated Fe, Mn, and Zn coincide with the inclusion.

81
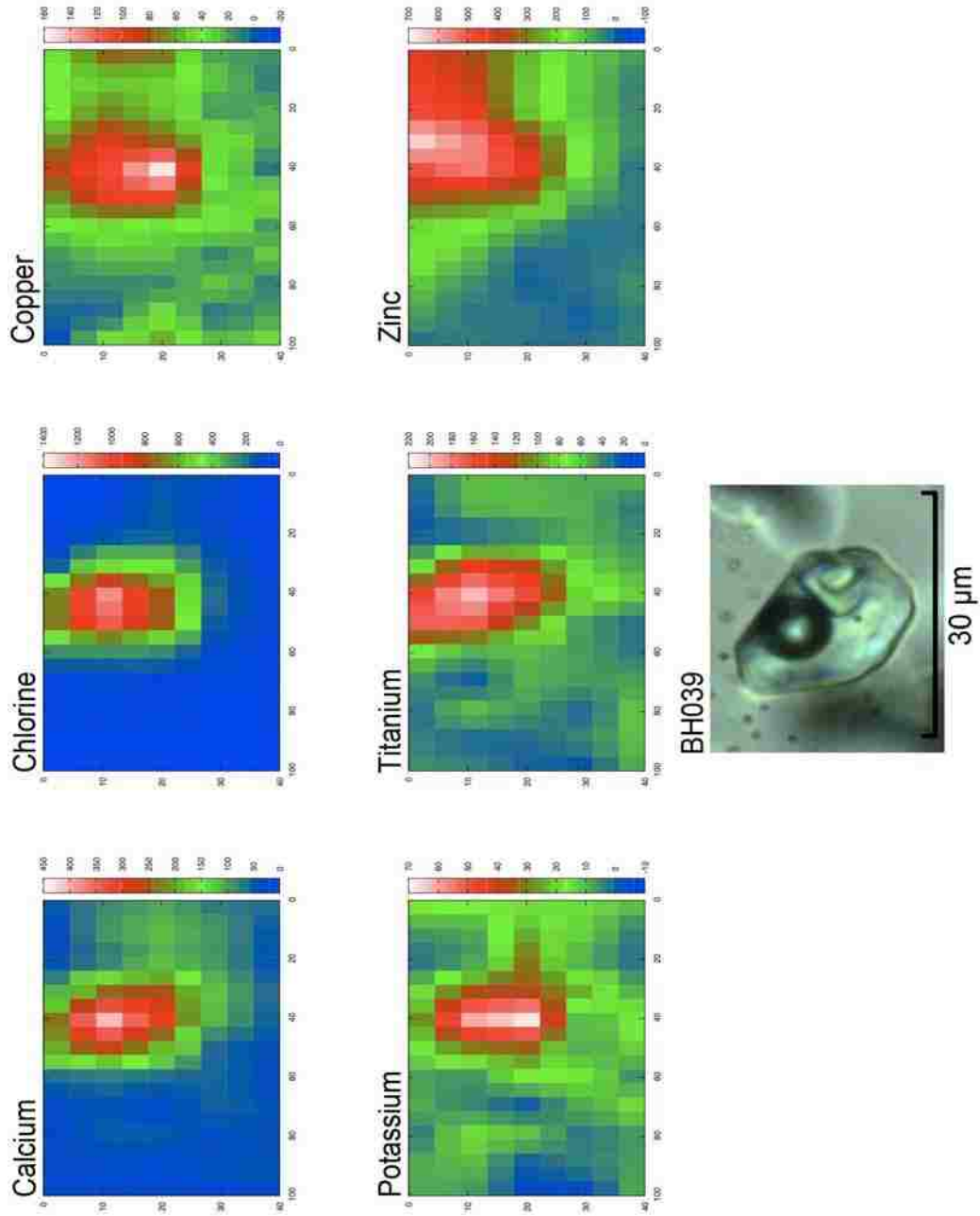
Figure 14 Elemental distribution maps for VB20H inclusion #BH039 exhibiting diffuse Cu distribution throughout the entire liquid phase of the fluid inclusion.
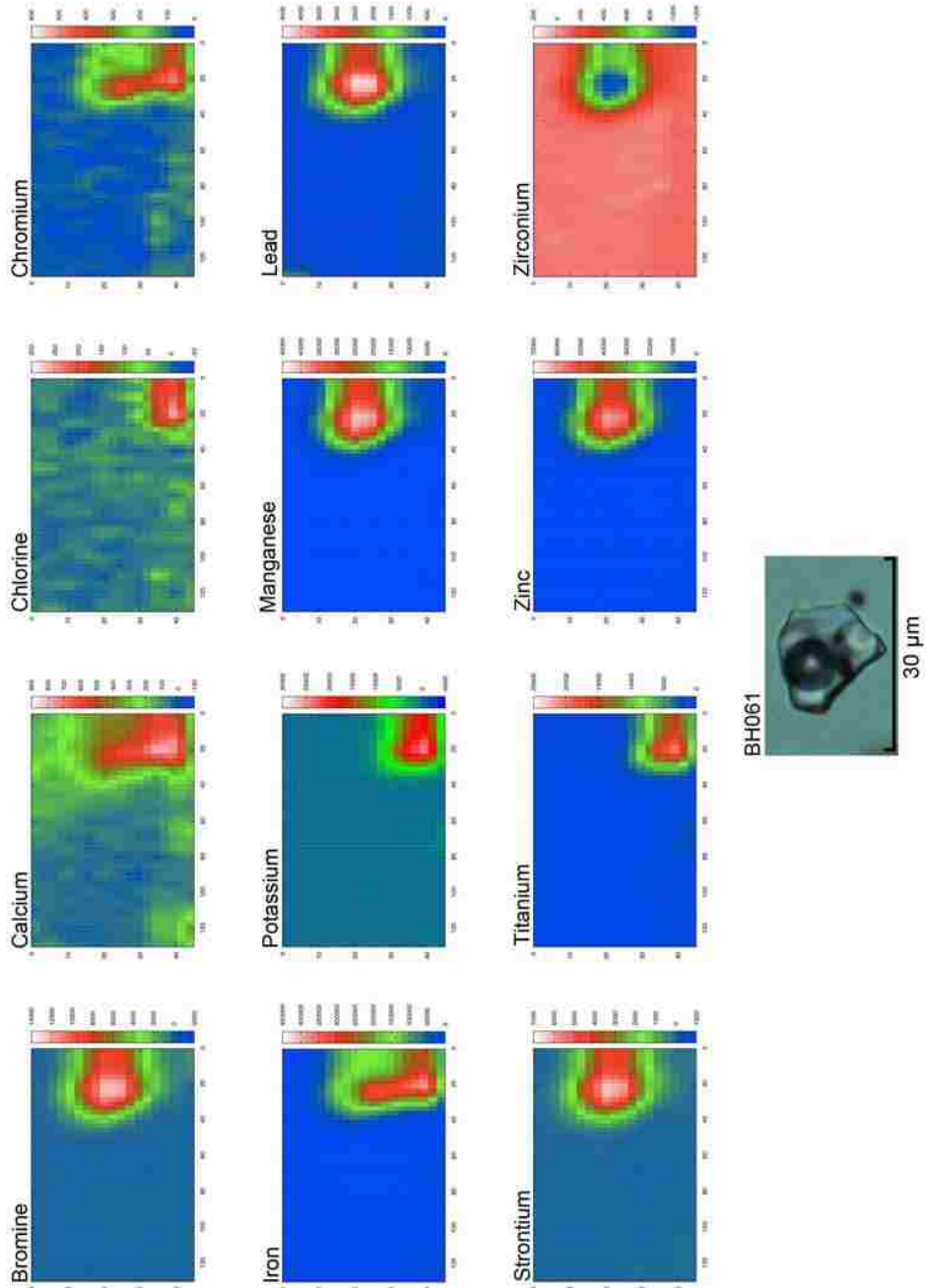
Figure 15 Elemental distribution maps for VB20H inclusion #BH061 exhibiting coincident Ca and Cr with Fe, Mn, and Zn, in addition to Br, Sr, and a relative absence of Zr.
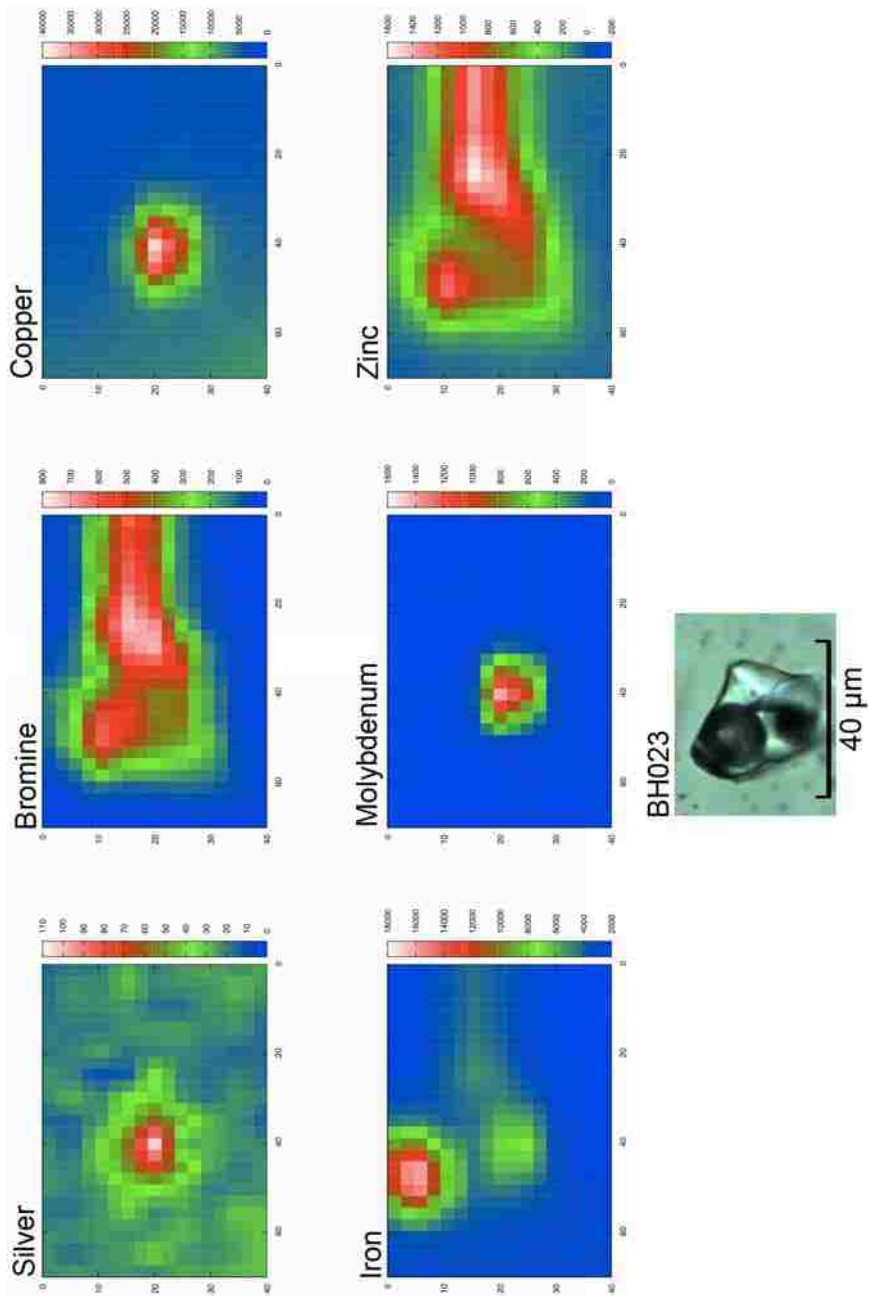
Figure 16 Elemental distribution maps for VB20H inclusion #BH023 exhibiting concentrated Cu, likely related to the presence of a Cu-bearing daughter crystal.
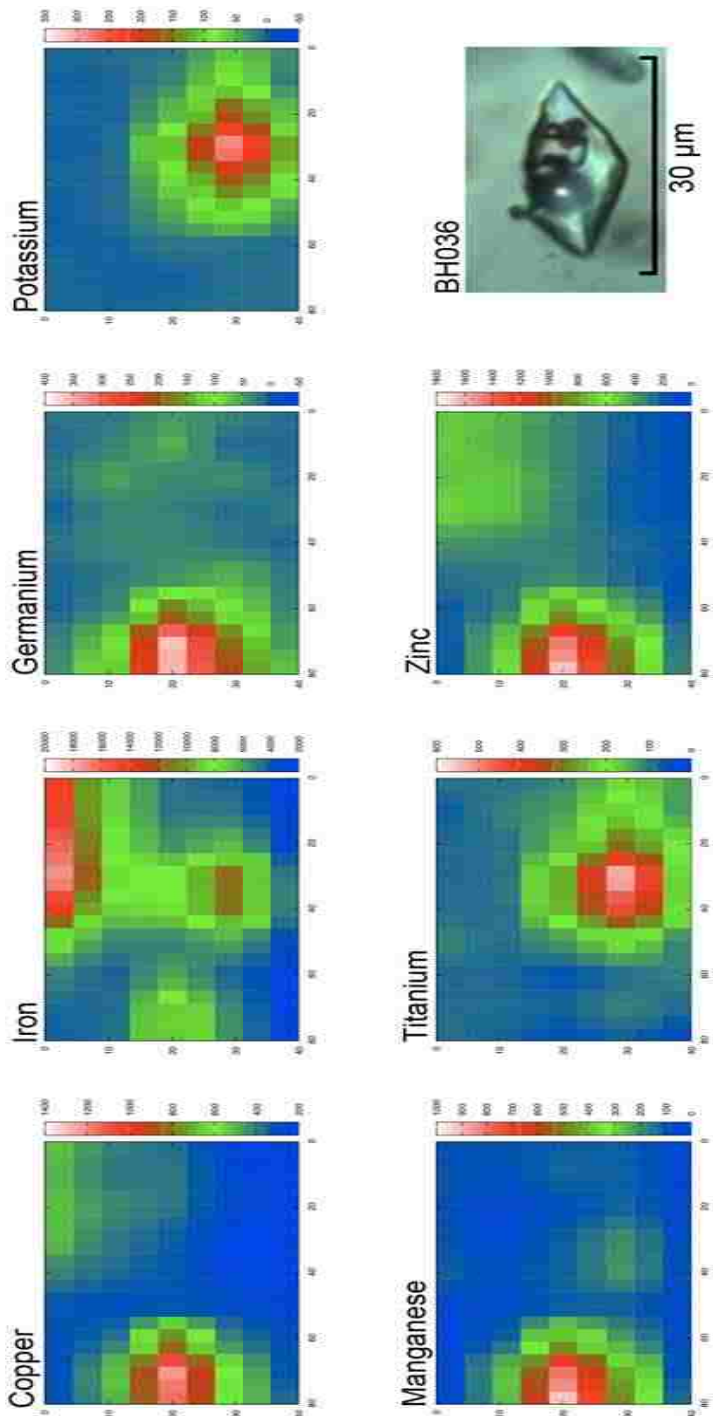
Figure 17 Elemental distribution maps for VB20H inclusion #BH036 exhibiting diffuse Cu throughout the liquid phase of the fluid inclusion.
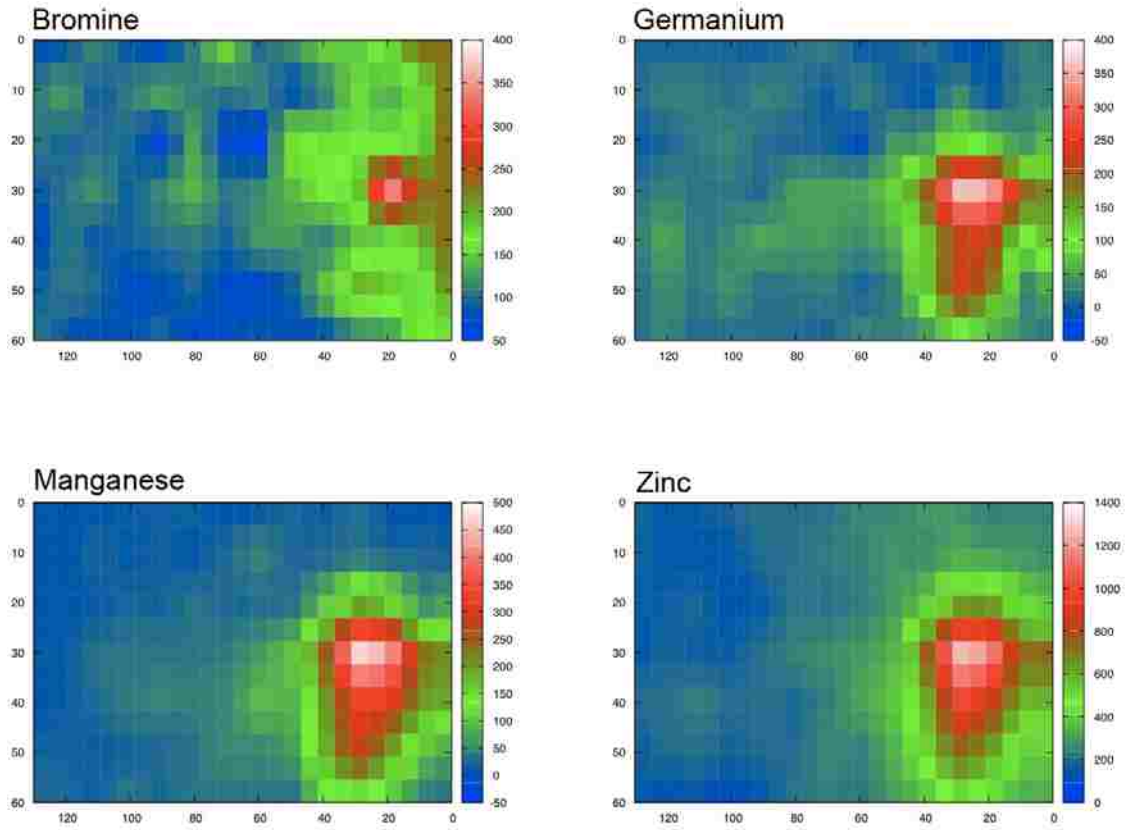
Figure 18 Elemental distribution maps for VB20H inclusion #BH033 exhibiting relative enrichment of Ge within the fluid inclusion, coincident with Mn, Zn, and to a lesser extent, Br.
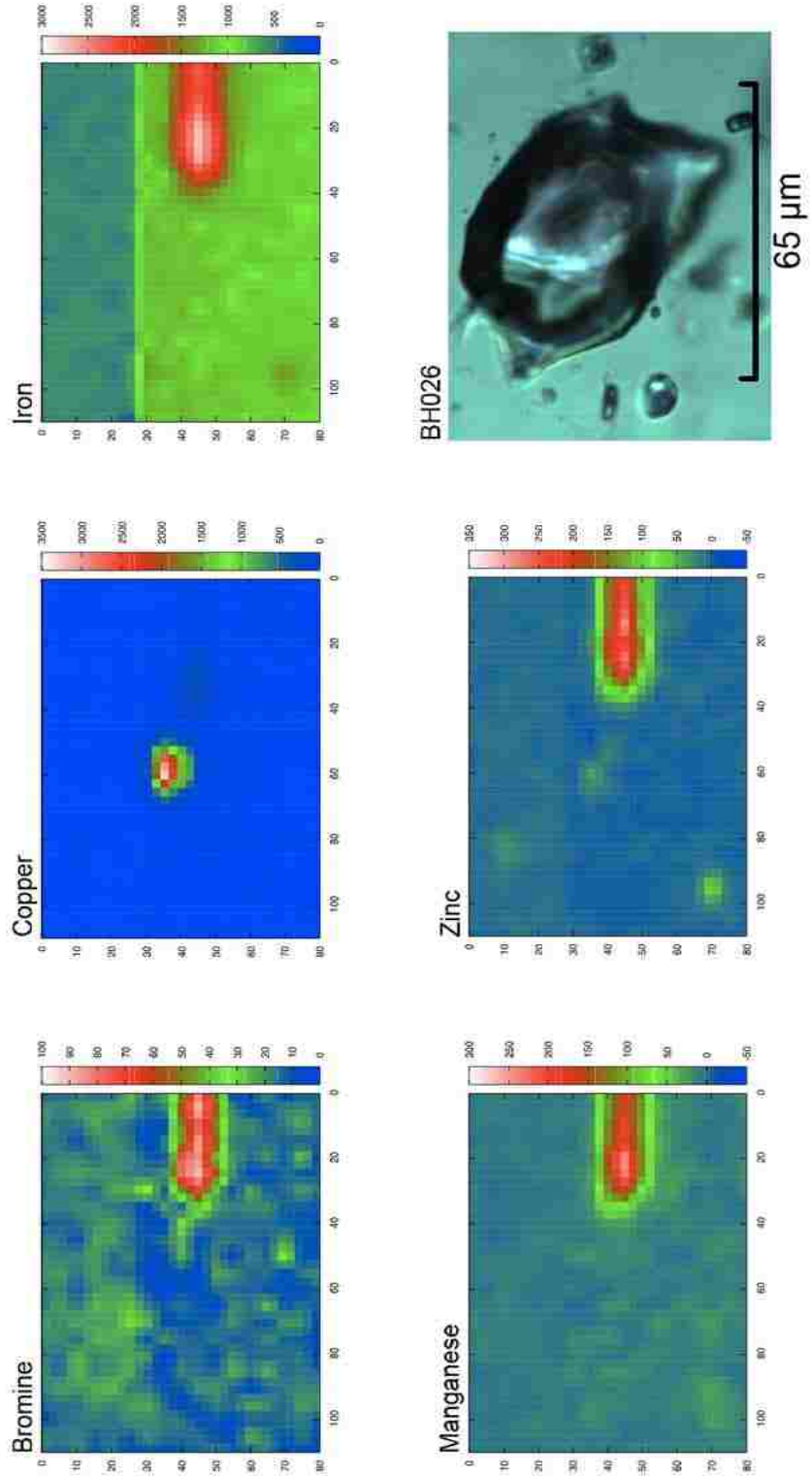
Figure 19 Elemental distribution maps for VB60 inclusion #BH026 exhibiting coincident enrichment of Fe, Mn, and Zn, along with Br. Cu is concentrated into a small area consistent with the presence of a Cu-Fe daughter crystal.

87
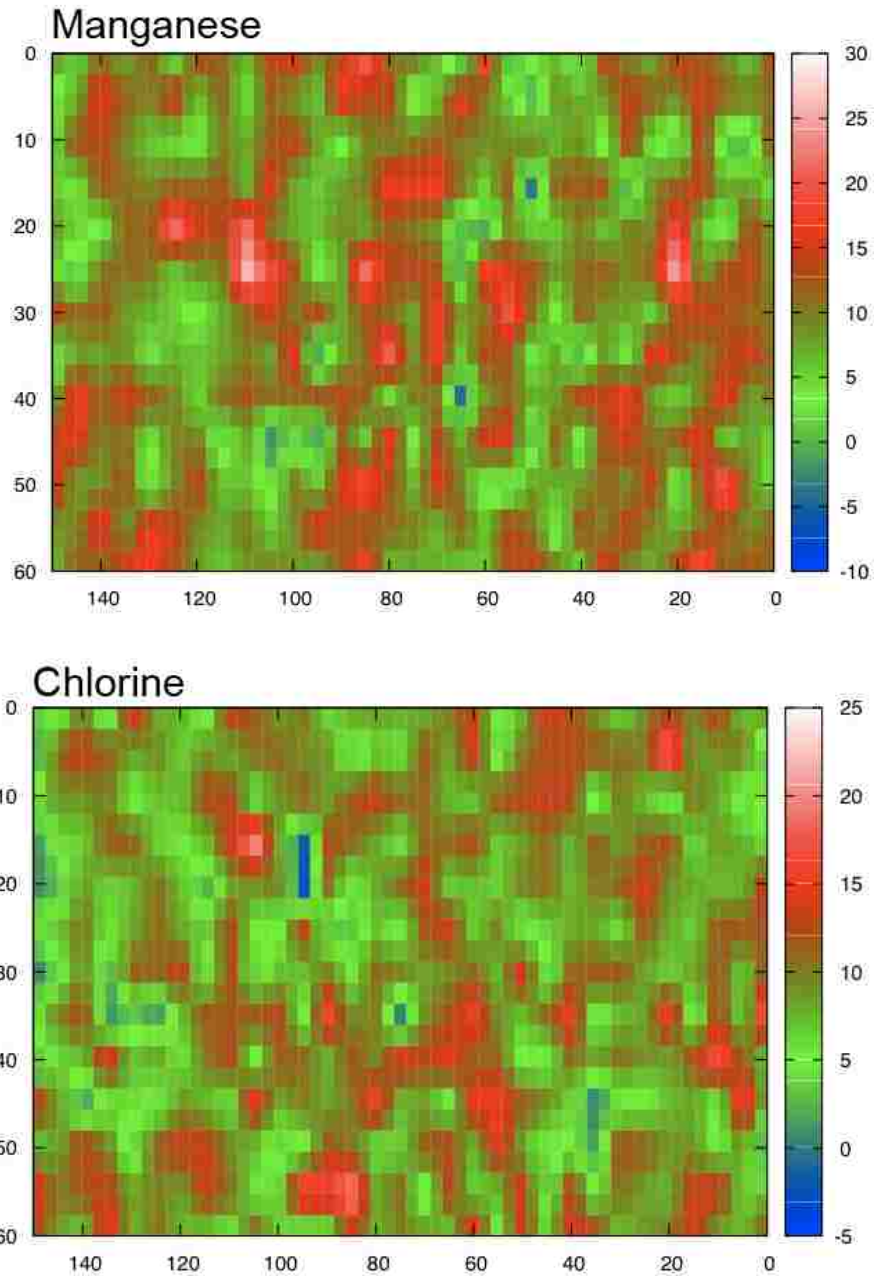
Figure 20 Elemental distribution maps of Cl and Mn within inclusion #BH021, demonstrating the lack of apparent patterns that was typically observed in B35 and B85 inclusions. Correlation with a photomicrograph of an individual inclusion was not possible.
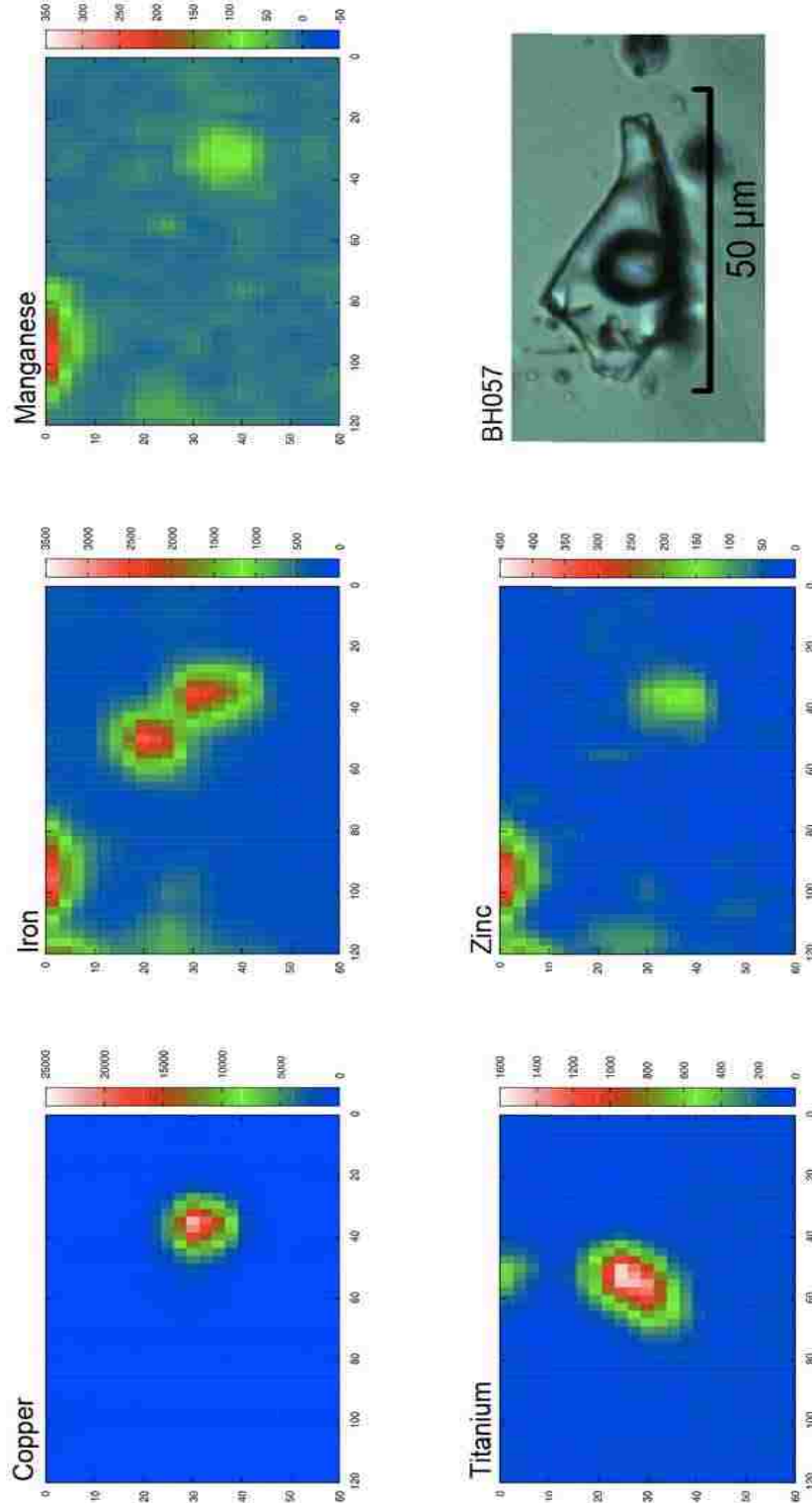
Figure 21 Elemental distribution maps for VB20H inclusion #BH057 exhibiting overlapping elevated Cu and Fe.
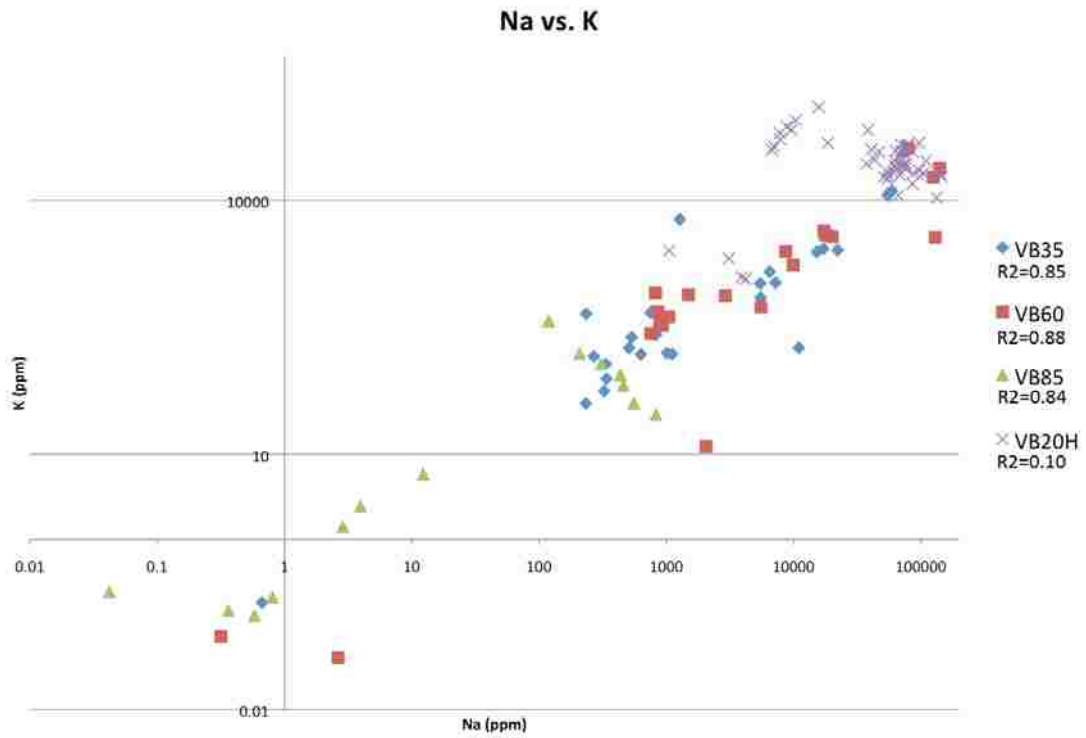
Figure 22 Na vs. K plot. Note that Na and K are strongly correlated in all but VB20H inclusions.

90
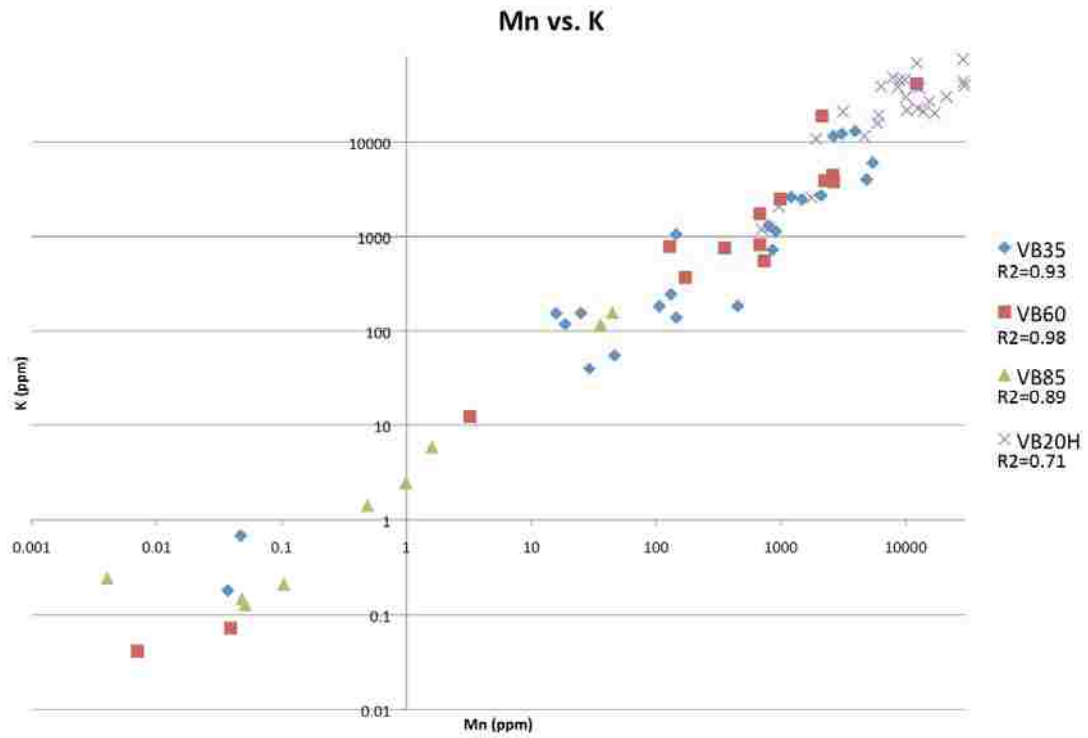
Figure 23 Mn vs. K plot. Mn and K are correlated strongly in all inclusion types.
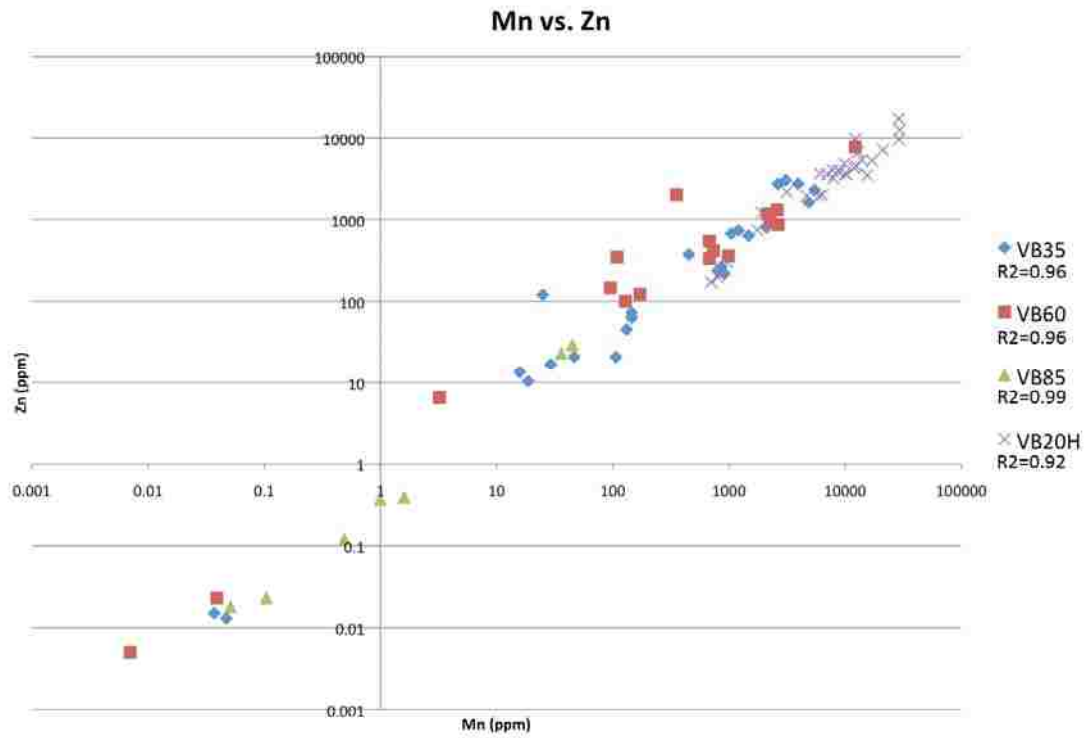
Figure 24 Mn vs. Zn plot. Mn and Zn are strongly correlated in all inclusion types.
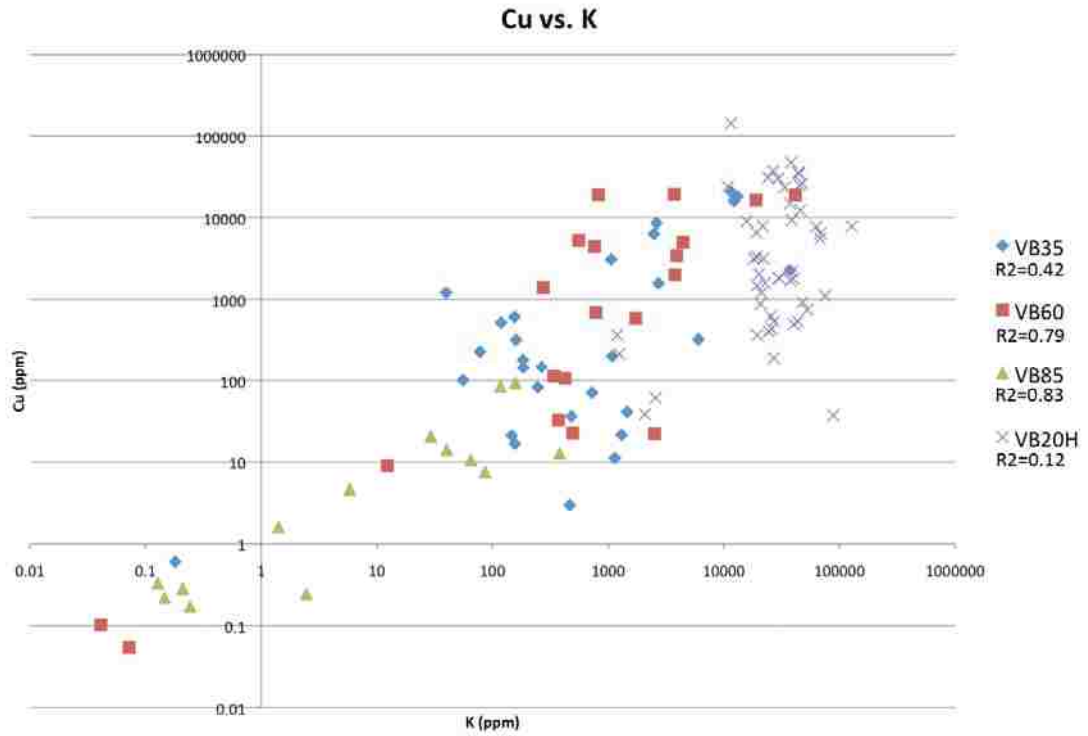
Figure 25 Cu vs. K plot. Note that Cu and K are strongly correlated in VB60 and VB85 type inclusions, moderately correlated in VB35 inclusions, and poorly correlated in VB20H inclusions.
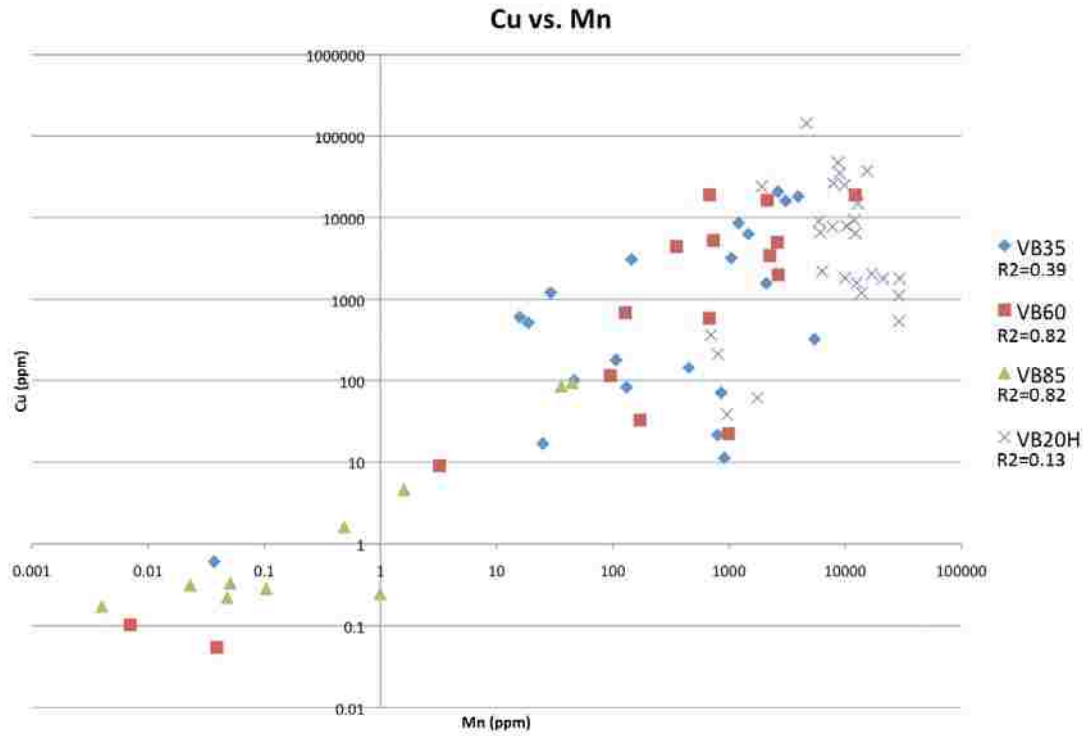
Figure 26 Cu vs. Mn plot. Cu and Mn are strongly correlated in VB60 and VB85 type inclusions, moderately correlated in VB35 inclusions, and poorly correlated in VB20H inclusions.
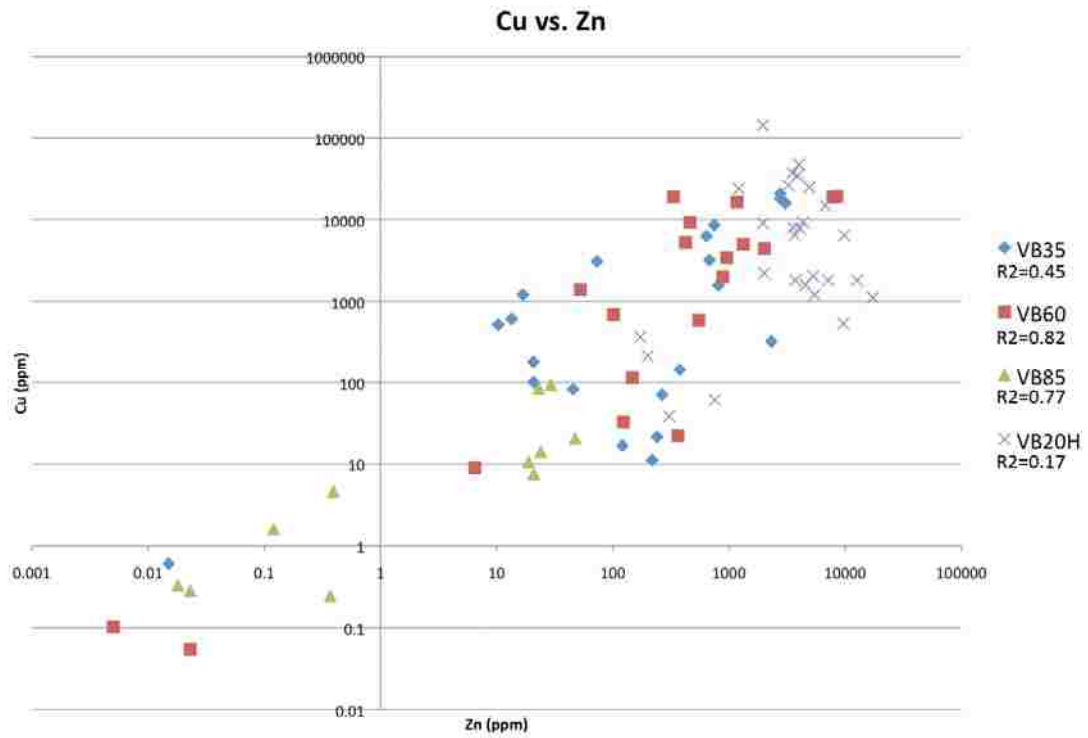
Figure 27 Cu vs. Zn plot. Cu and Zn are strongly correlated in VB60 and VB85 type inclusions, moderately correlated in VB35 inclusions, and poorly correlated in VB20H inclusions.
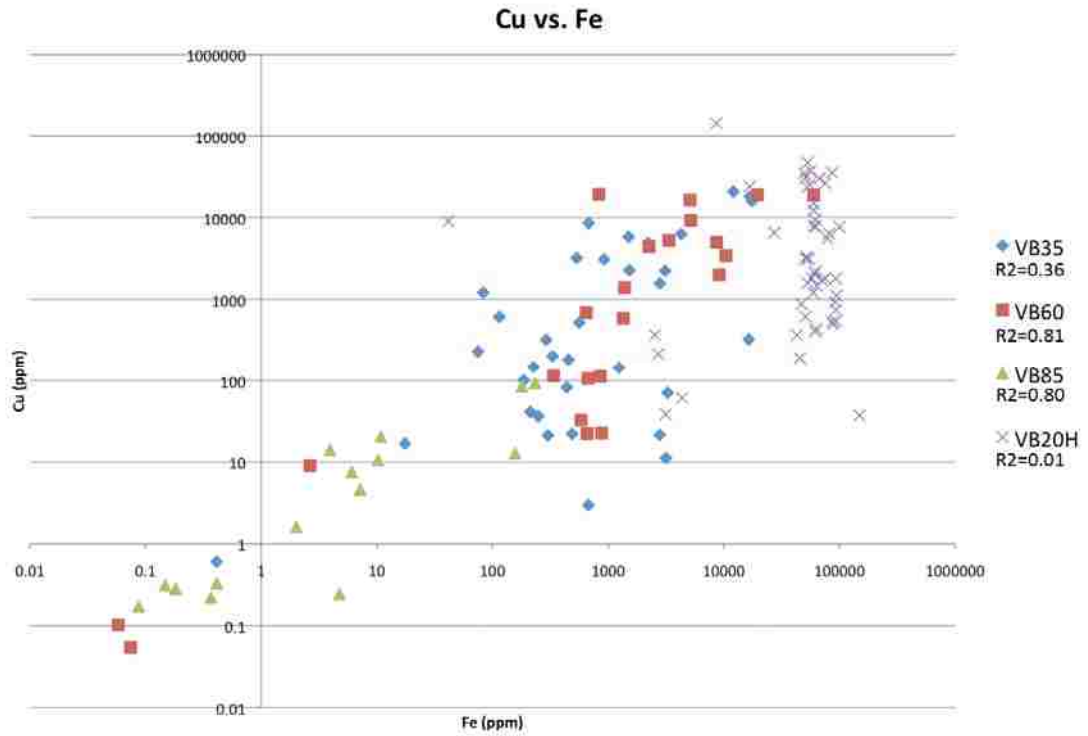
Figure 28 Cu vs. Fe plot. Cu and Fe are strongly correlated in VB60 and VB85 type inclusions, moderately correlated in VB35 inclusions, and poorly correlated in VB20H inclusions.
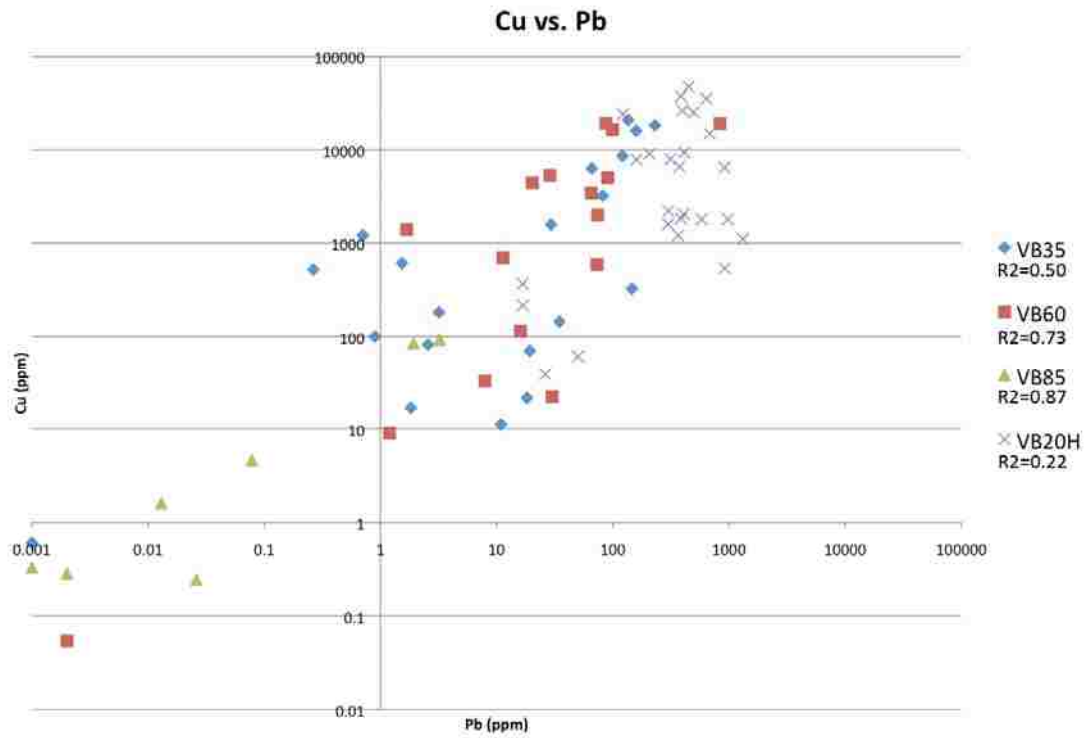
Figure 29 Cu vs. Pb plot. Cu and Pb are strongly correlated in VB60 and VB85 type inclusions, moderately correlated in VB35 inclusions, and poorly correlated in VB20H inclusions.

97
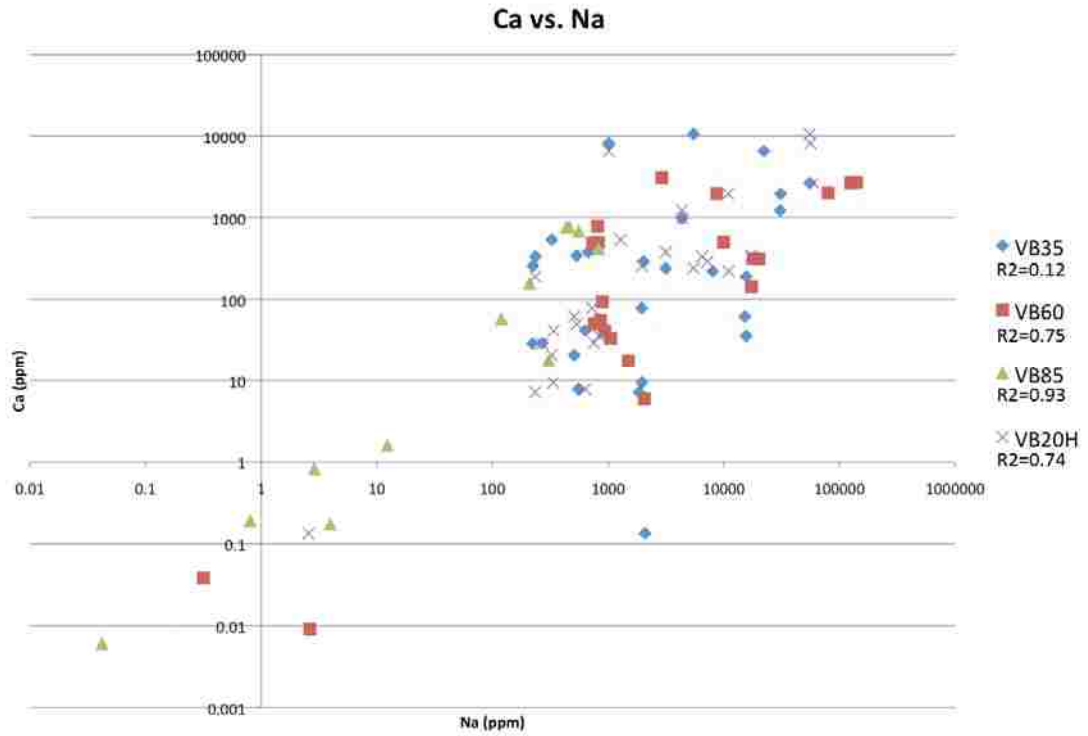
Figure 30 Ca vs. Na plot. Ca and Na are strongly correlated in VB60 and VB85 type inclusions, moderately correlated in VB20H inclusions, and poorly correlated in VB35 inclusions.
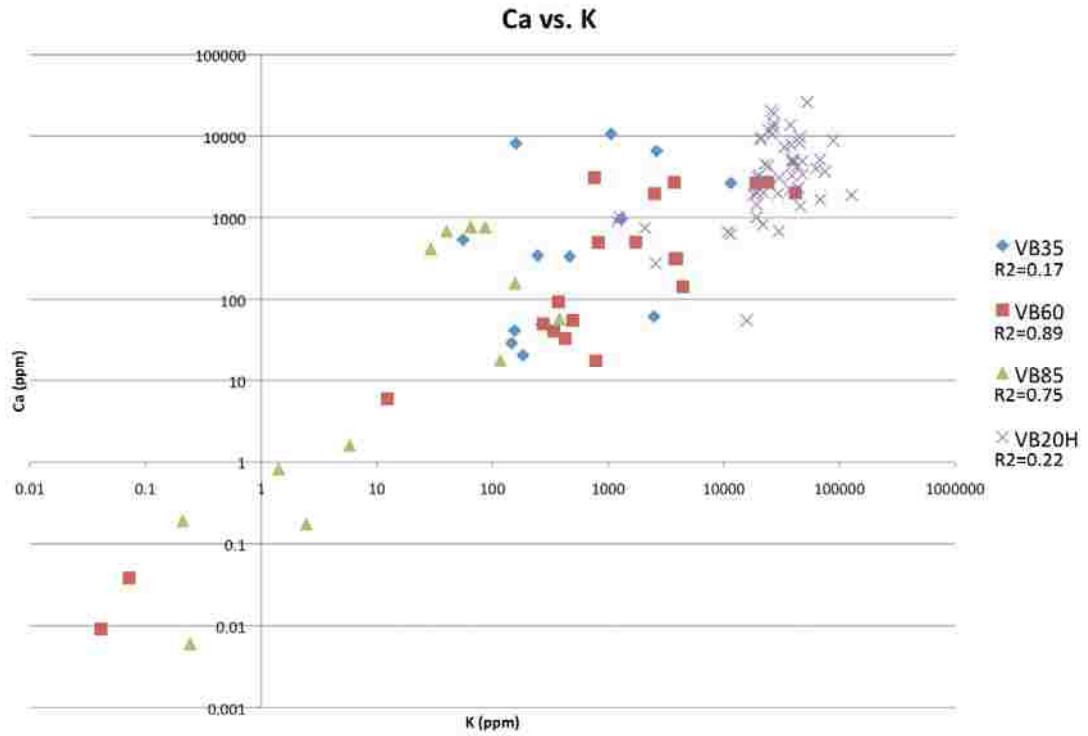
Figure 31 Ca vs. K plot. Ca and K are strongly correlated in VB60 and VB85 type inclusions and poorly correlated in VB35 and VB20H type inclusions.
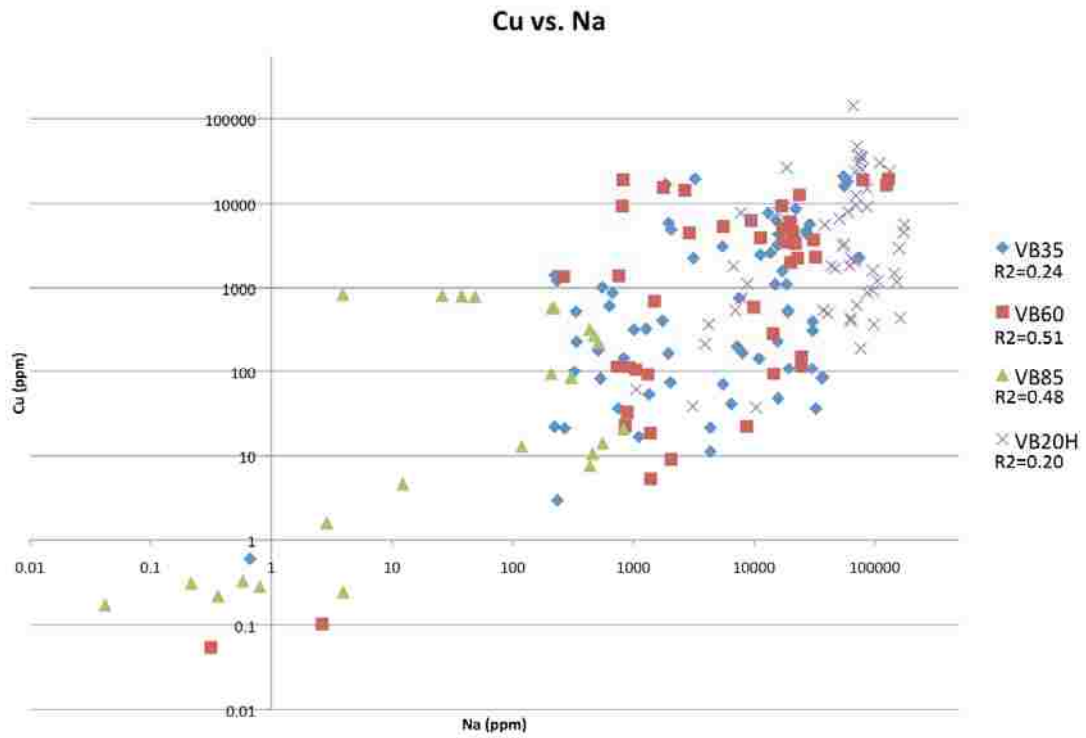
Figure 32 Cu vs. Na plot. Cu and Na are moderately correlated in VB60 and VB85 type inclusions and poorly correlated in VB35 and VB20H type inclusions.
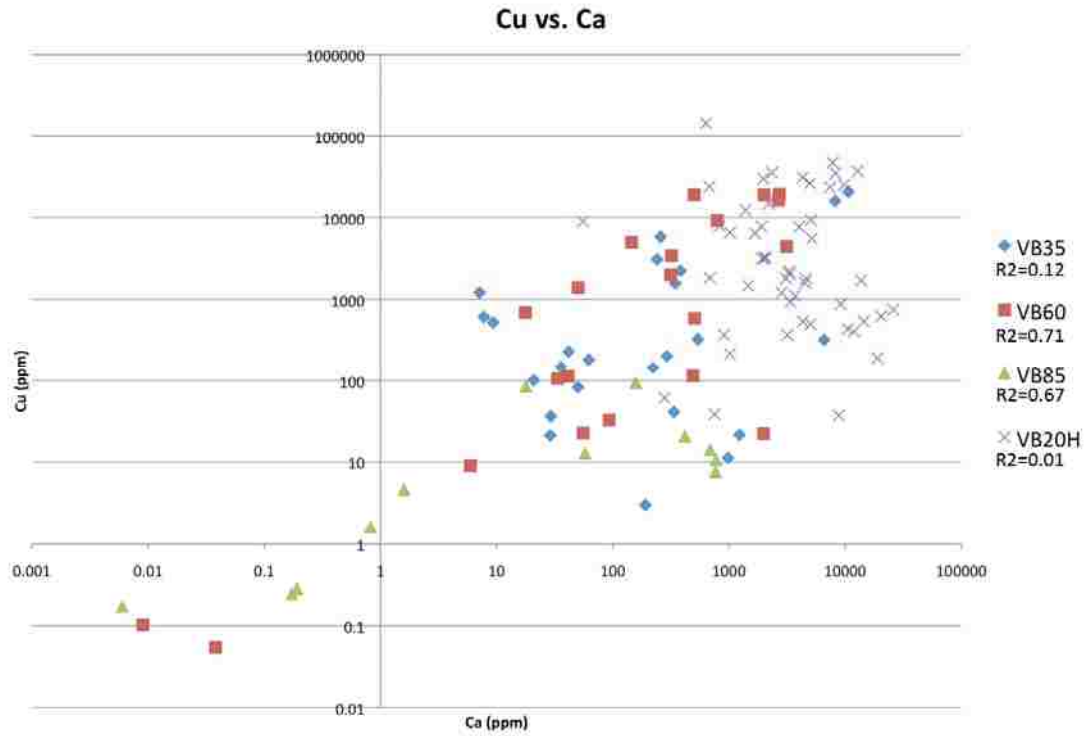
Figure 33 Cu vs. Ca plot. Cu and Ca are moderately correlated in VB60 and VB85 type inclusions and poorly correlated in VB35 and VB20H type inclusions.
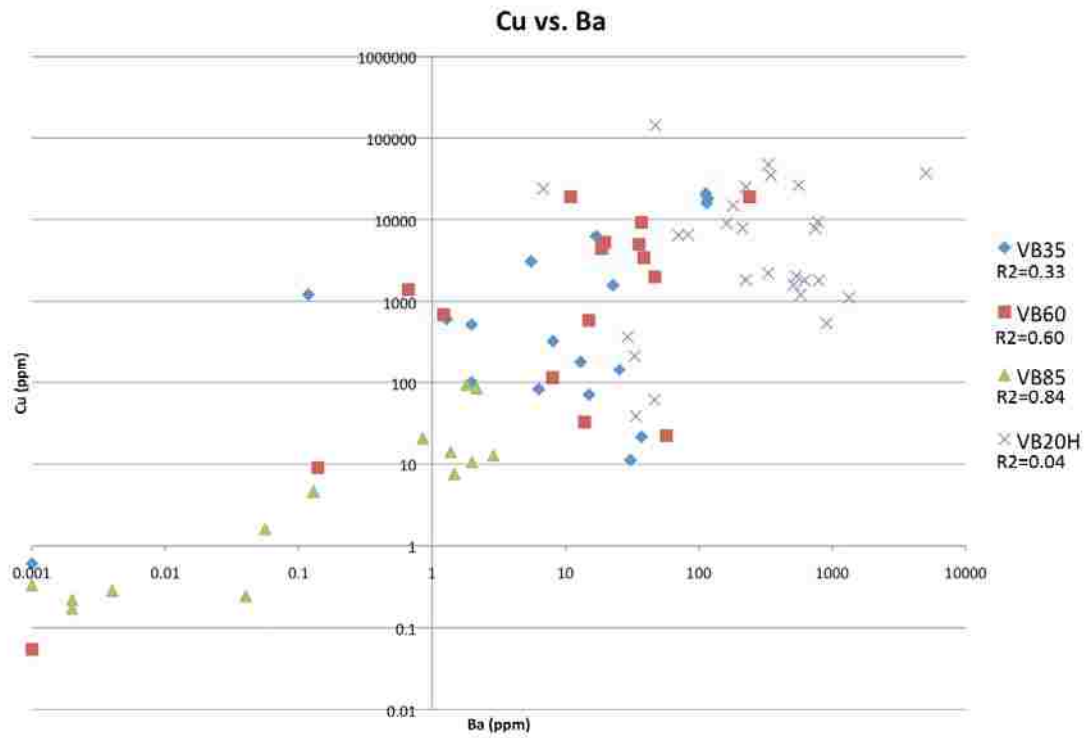
Figure 34 Cu vs. Ba plot. Cu and Ba are strongly correlated in VB85 inclusions, moderately correlated in VB60 inclusions, and poorly correlated in VB35 and VB20H type inclusions.
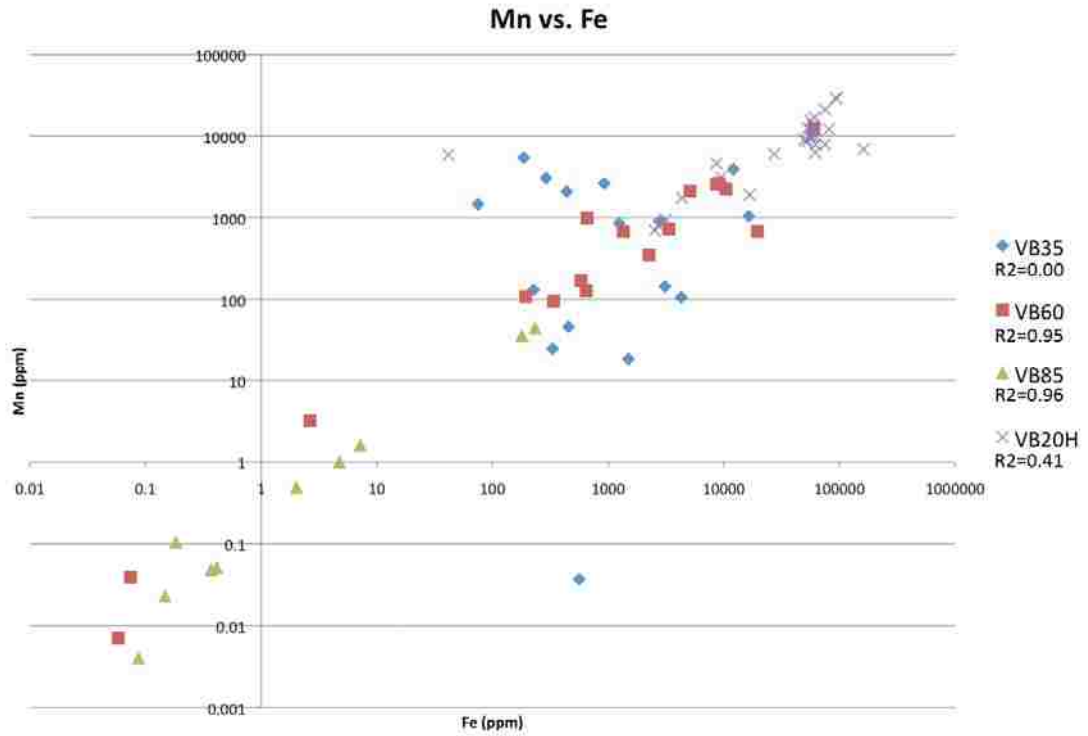
Figure 35 Mn vs. Fe plot. Mn and Fe are strongly correlated in VB60 and VB85 type inclusions, moderately correlated in VB20H inclusions, and poorly correlated in VB35 inclusions.
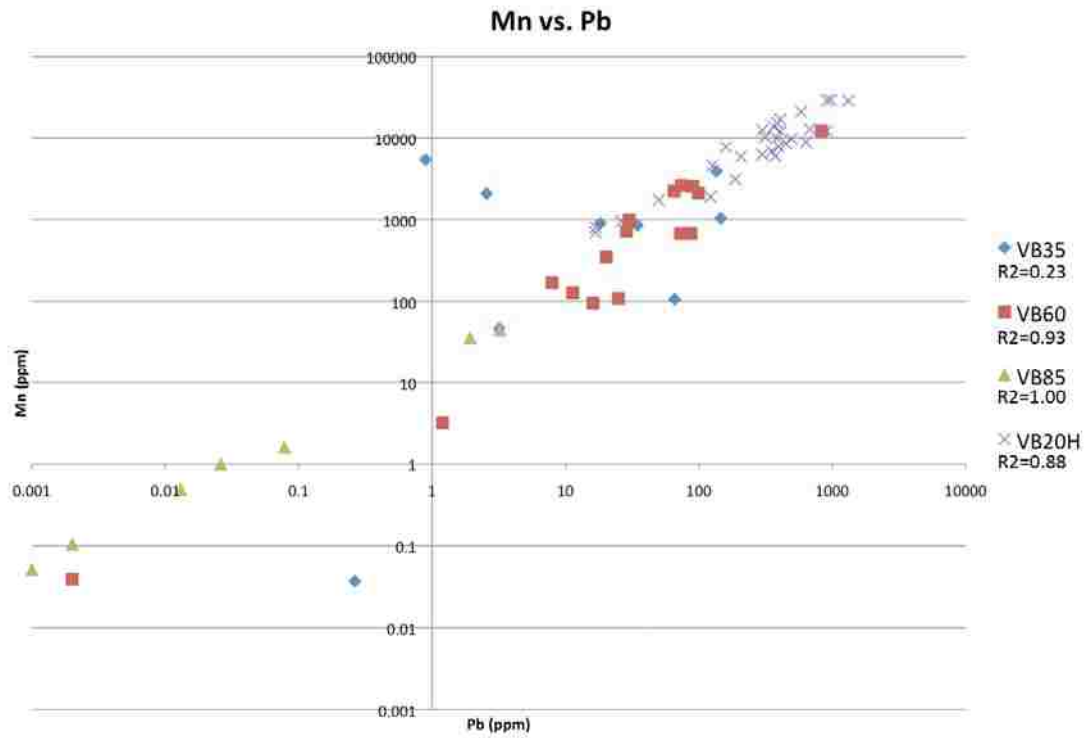
Figure 36 Mn vs. Pb plot. Mn and Pb are strongly correlated in VB60, VB85, and VB20H type inclusions and poorly correlated in VB35 inclusions.
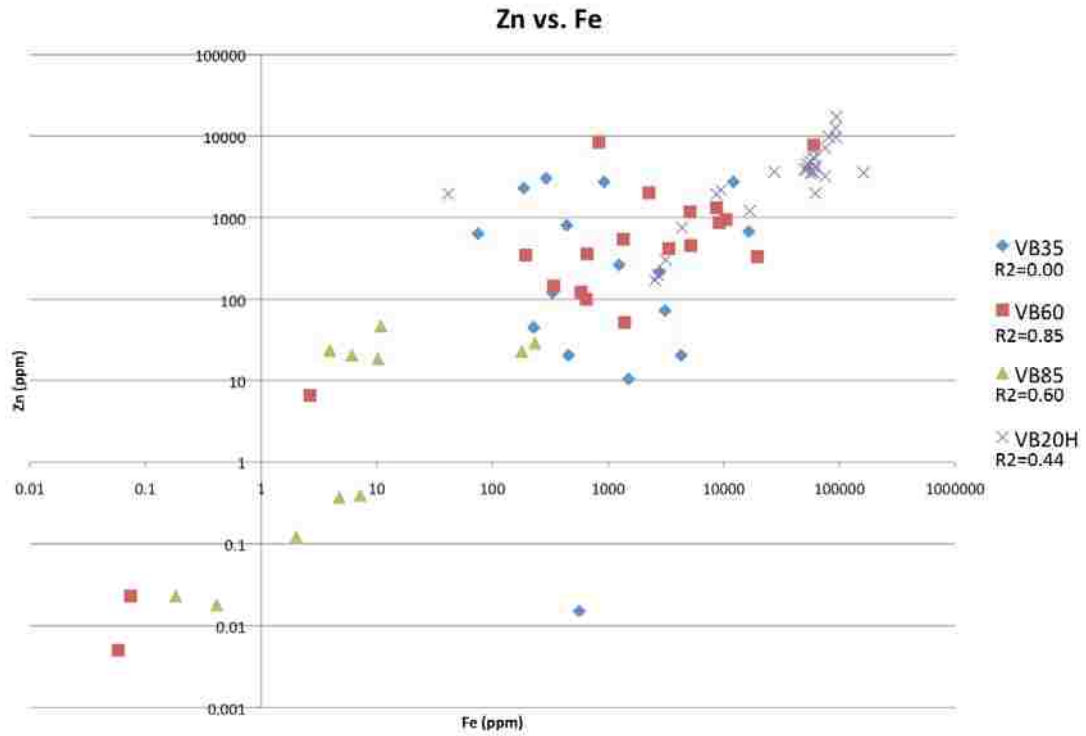
Figure 37 Zn vs. Fe plot. Zn and Fe are strongly correlated in VB60 inclusions, moderately correlated in VB85 and VB20H type inclusions, and poorly correlated in VB35 inclusions.
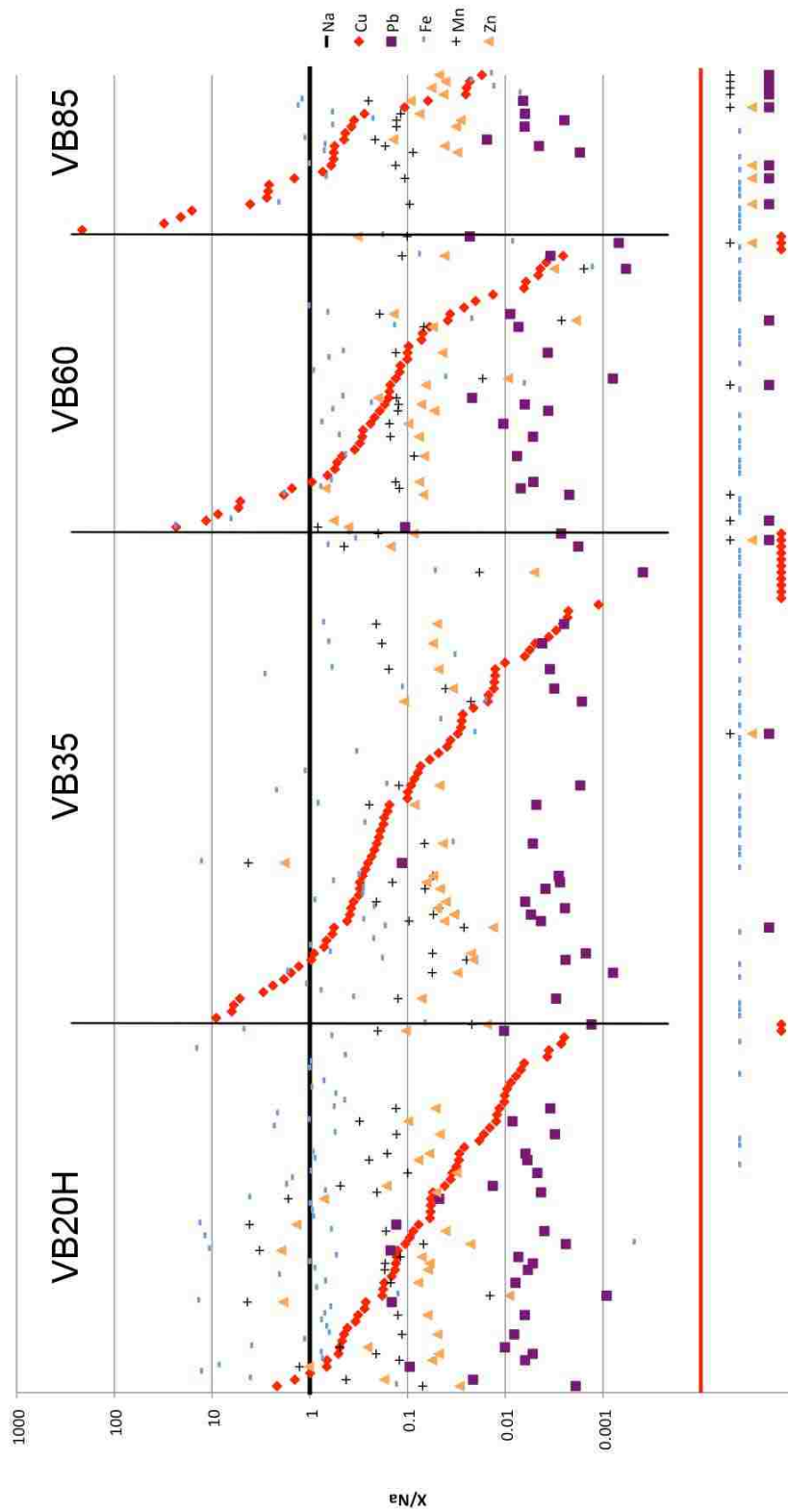
Figure 38 Group 1 elements Cu, Pb, Fe, Mn, and Zn ratioed to Na. Ratios are plotted in order of decreasing Cu/Na for each inclusion type.   Points at the bottom of the plot, below the red line, indicate analysis for which elements were detected, but were below the limit of detection.

106
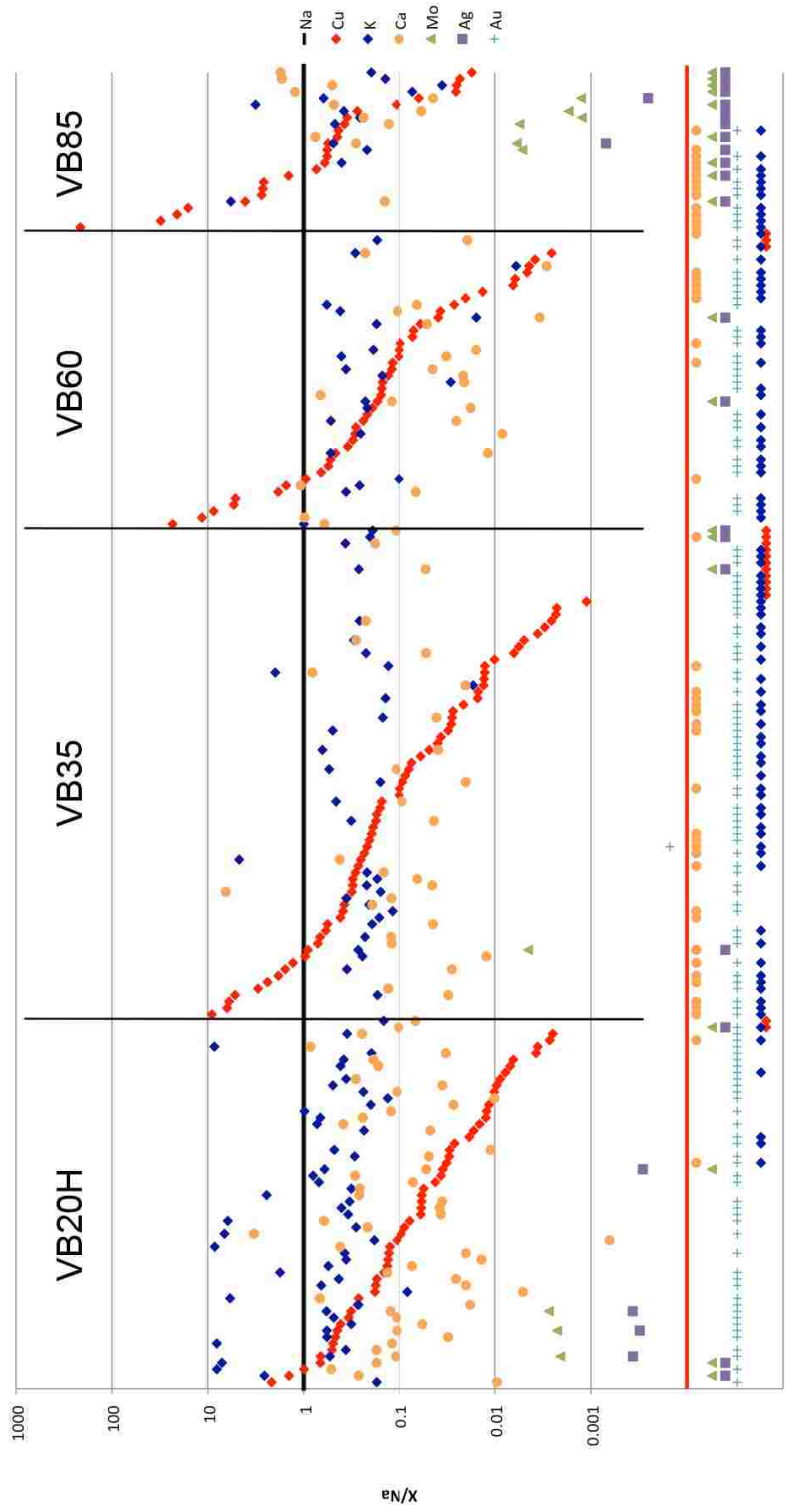
Figure 39 Group 2 elements K, Ca, Mo, Ag, and Au ratioed to Na. Ratios are plotted in order of decreasing Cu/Na for each inclusion type. Points at the bottom of the plot, below the red line, indicate analysis for which elements were detected, but were below the limit of detection.

107
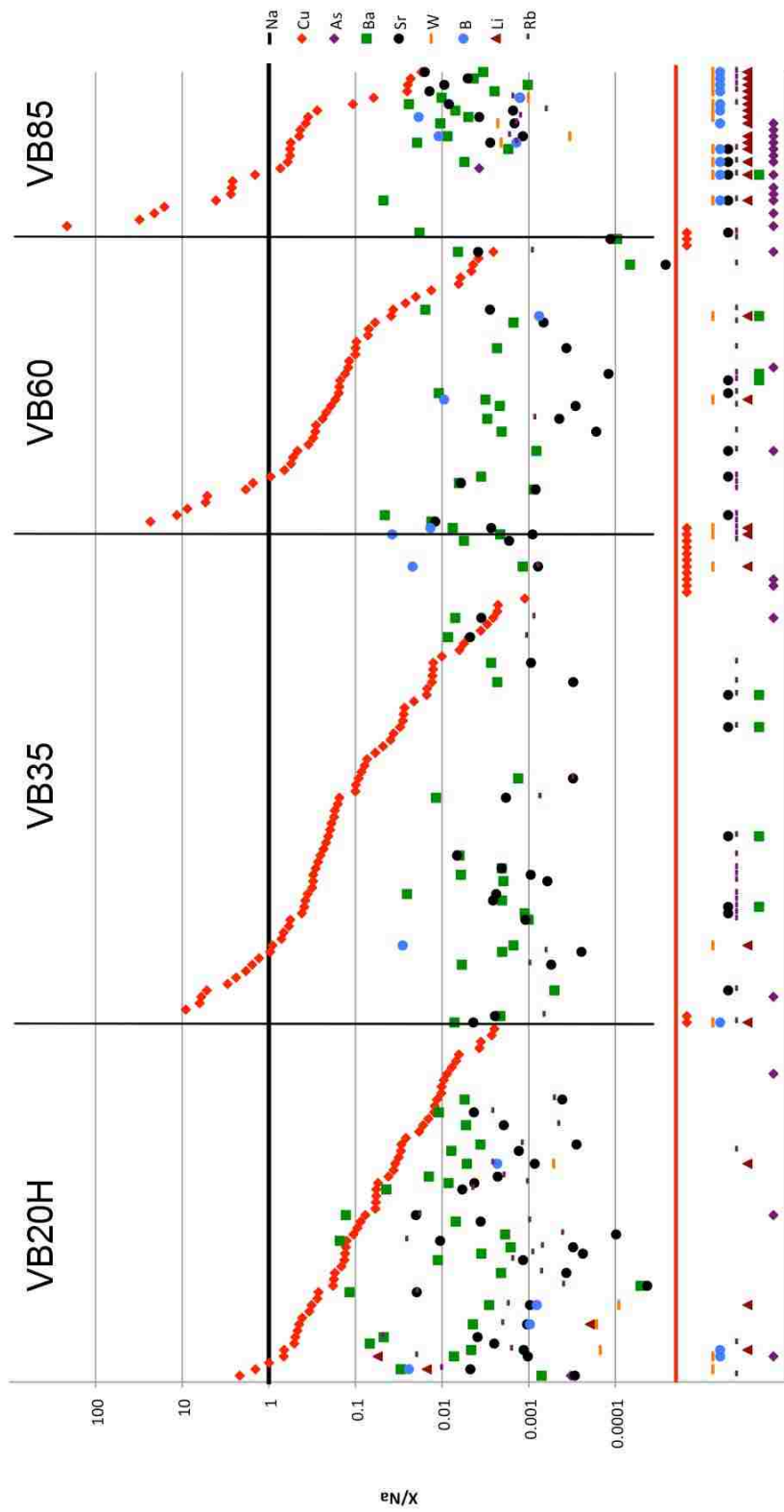
Figure 40 Group 3 elements As, Ba, Sr, W, B, Li and Rb ratioed to Na. Ratios are plotted in order of decreasing Cu/Na for each inclusion type. Points at the bottom of the plot, below the red line, indicate analysis for which elements were detected, but were below the limit of detection.
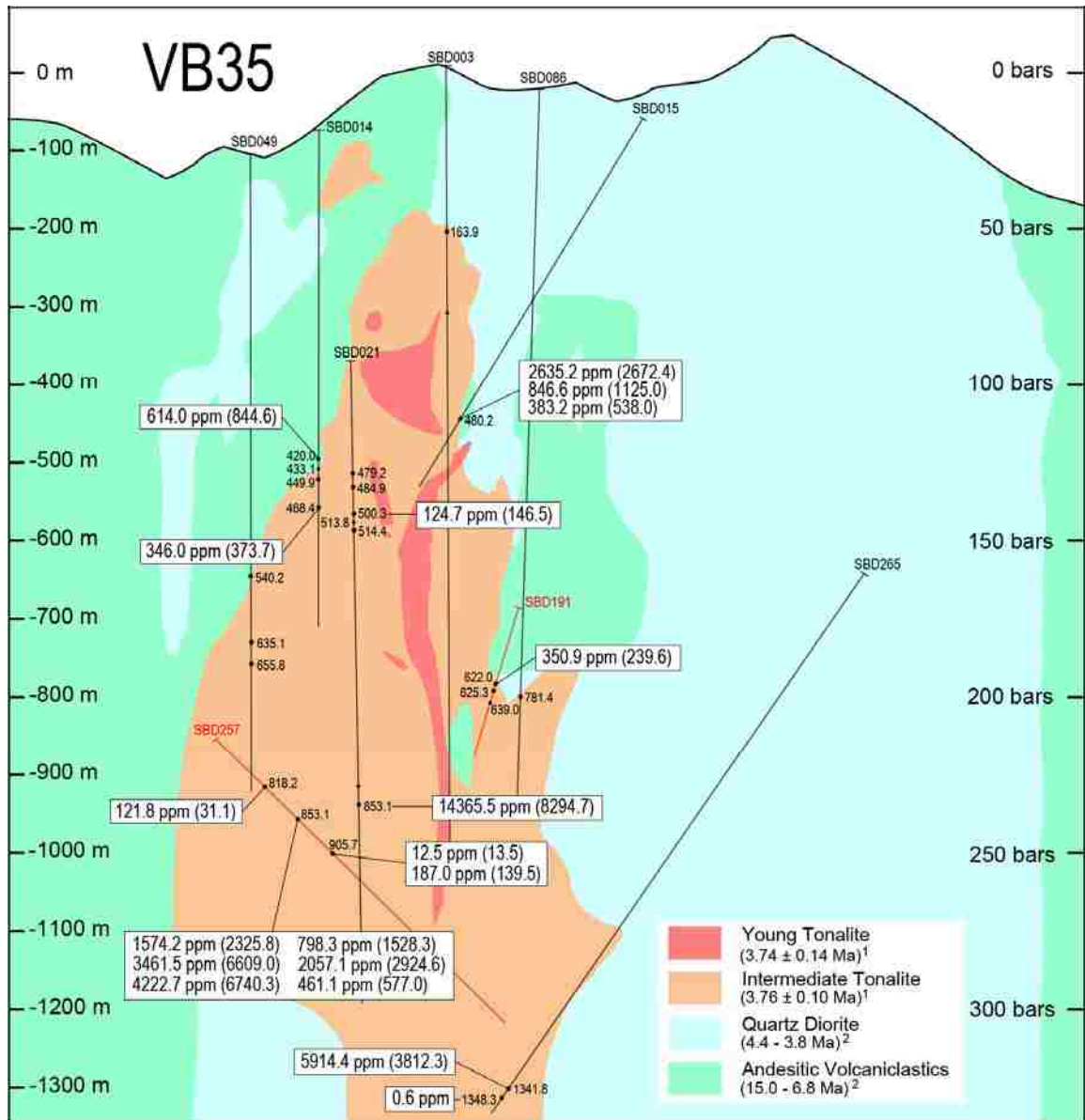
Figure 41 East-West cross section through the Batu Hijau deposit. Contained within the boxes are average Cu concentrations for either VB35 FIAs or single inclusions, obtained with LA-ICP-MS analyses, and plotted near the sample location. Standard deviations for FIA averages are listed in parentheses. Concentrations without a standard deviation indicate analyses of a single fluid inclusion. Multiples averages in a single box indicate analysis of multiple FIAs in a single sample.
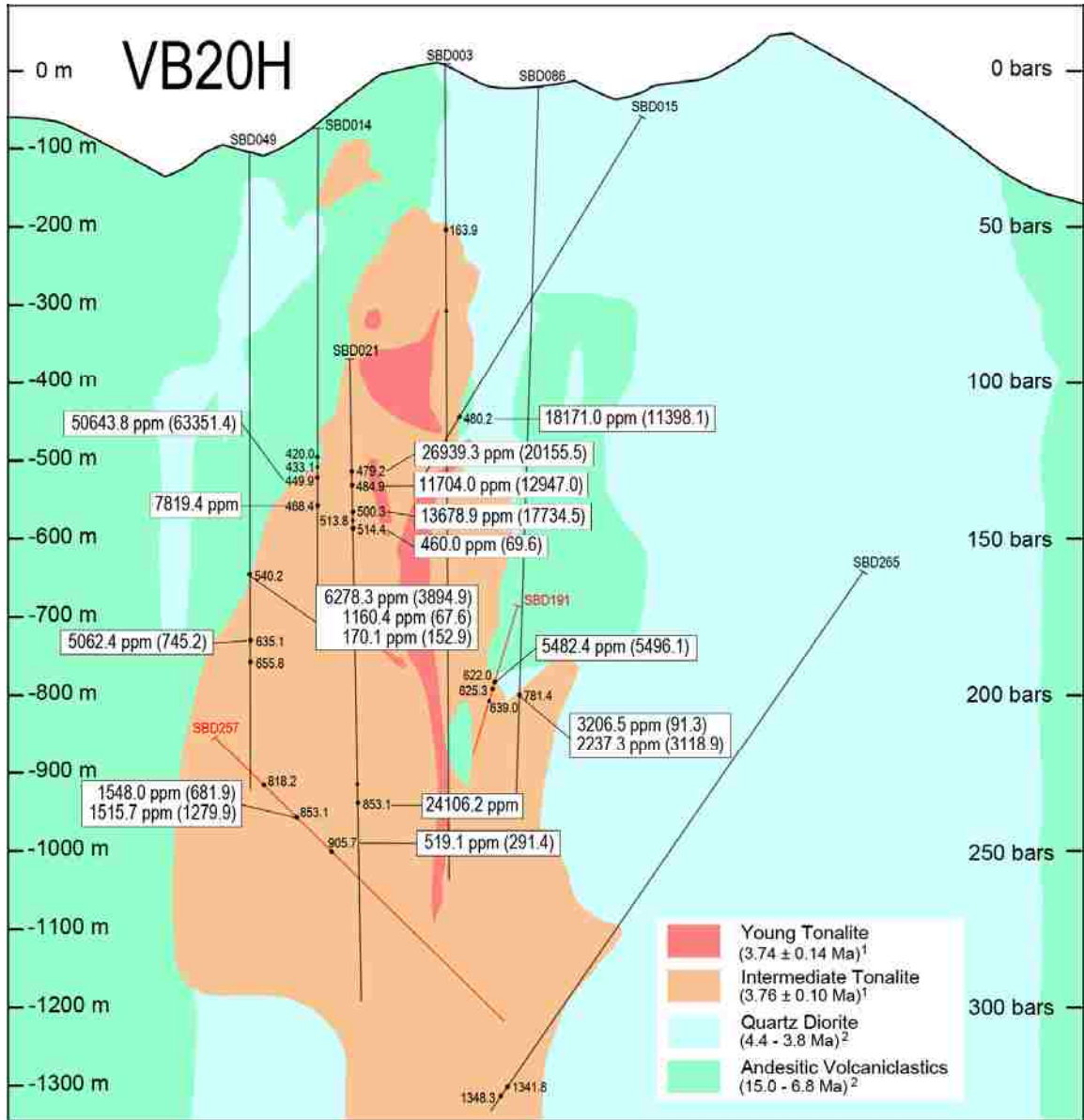
Figure 42 East-West cross section through the Batu Hijau deposit. Contained within the boxes are average Cu concentrations for either VB20H FIAs or single inclusions, obtained with LA-ICP-MS analyses, and plotted near the sample location. Standard deviations for FIA averages are listed in parentheses. Concentrations without a standard deviation indicate analyses of a single fluid inclusion. Multiples averages in a single box indicate analysis of multiple FIAs in a single sample.

110
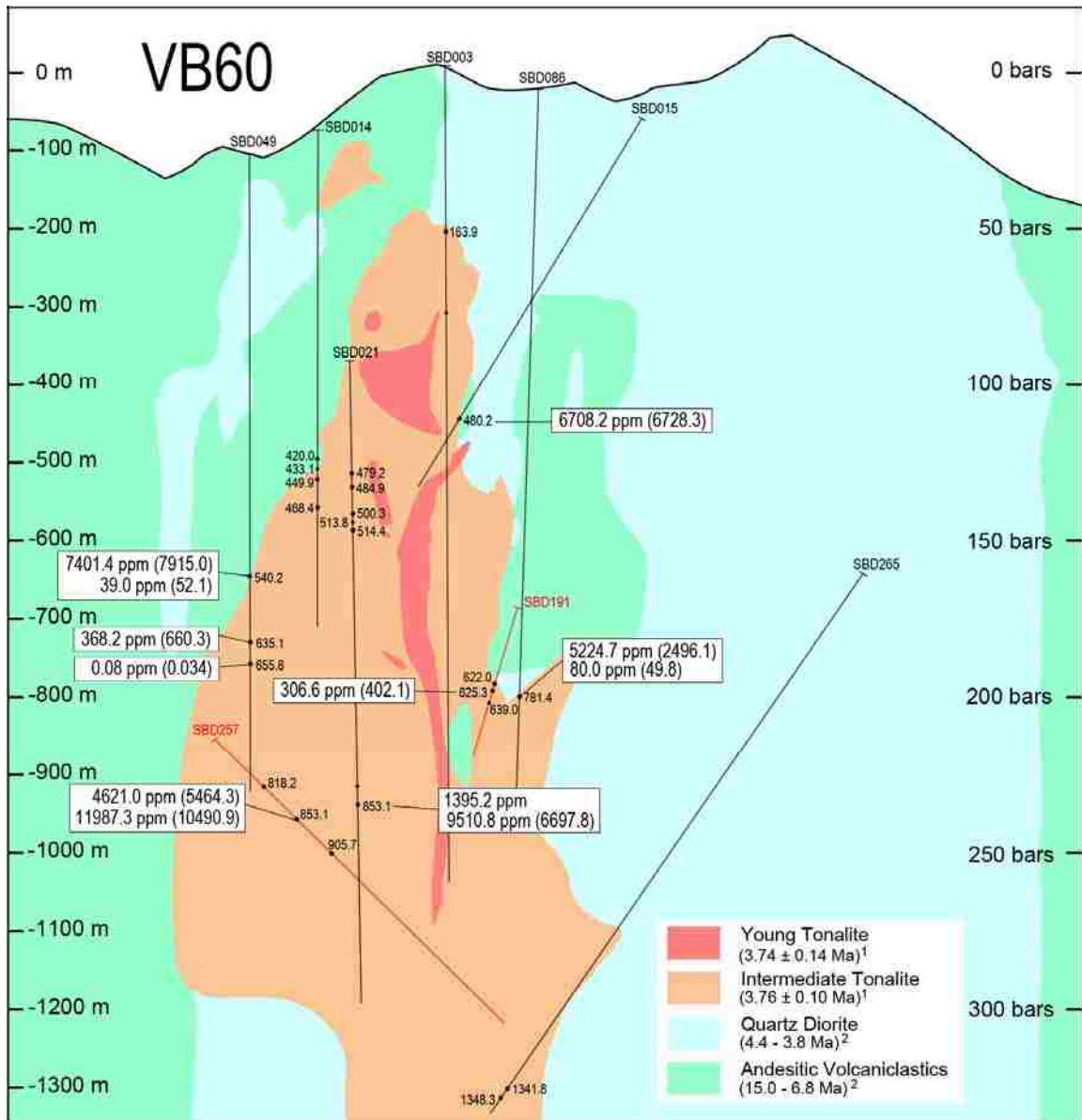
Figure 43 East-West cross section through the Batu Hijau deposit. Contained within the boxes are average Cu concentrations for either VB60 FIAs or single inclusions, obtained with LA-ICP-MS analyses, and plotted near the sample location. Standard deviations for FIA averages are listed in parentheses. Concentrations without a standard deviation indicate analyses of a single fluid inclusion. Multiples averages in a single box indicate analysis of multiple FIAs in a single sample.
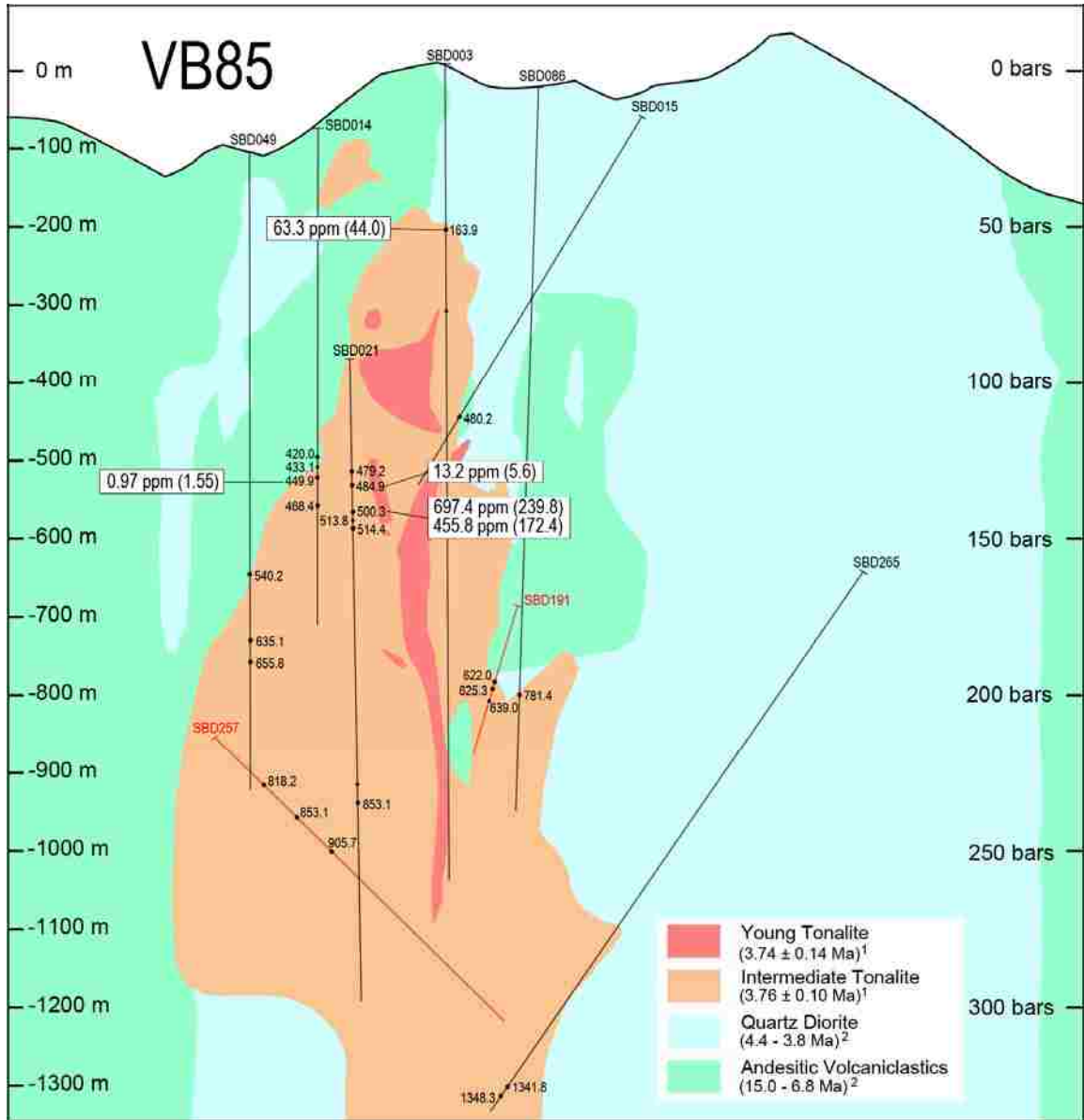
Figure 44 East-West cross section through the Batu Hijau deposit. Contained within the boxes are average Cu concentrations for either VB85 FIAs or single inclusions, obtained with LA-ICP-MS analyses, and plotted near the sample location. Standard deviations for FIA averages are listed in parentheses. Multiple averages in a single box indicate analysis of multiple FIAs in a single sample.
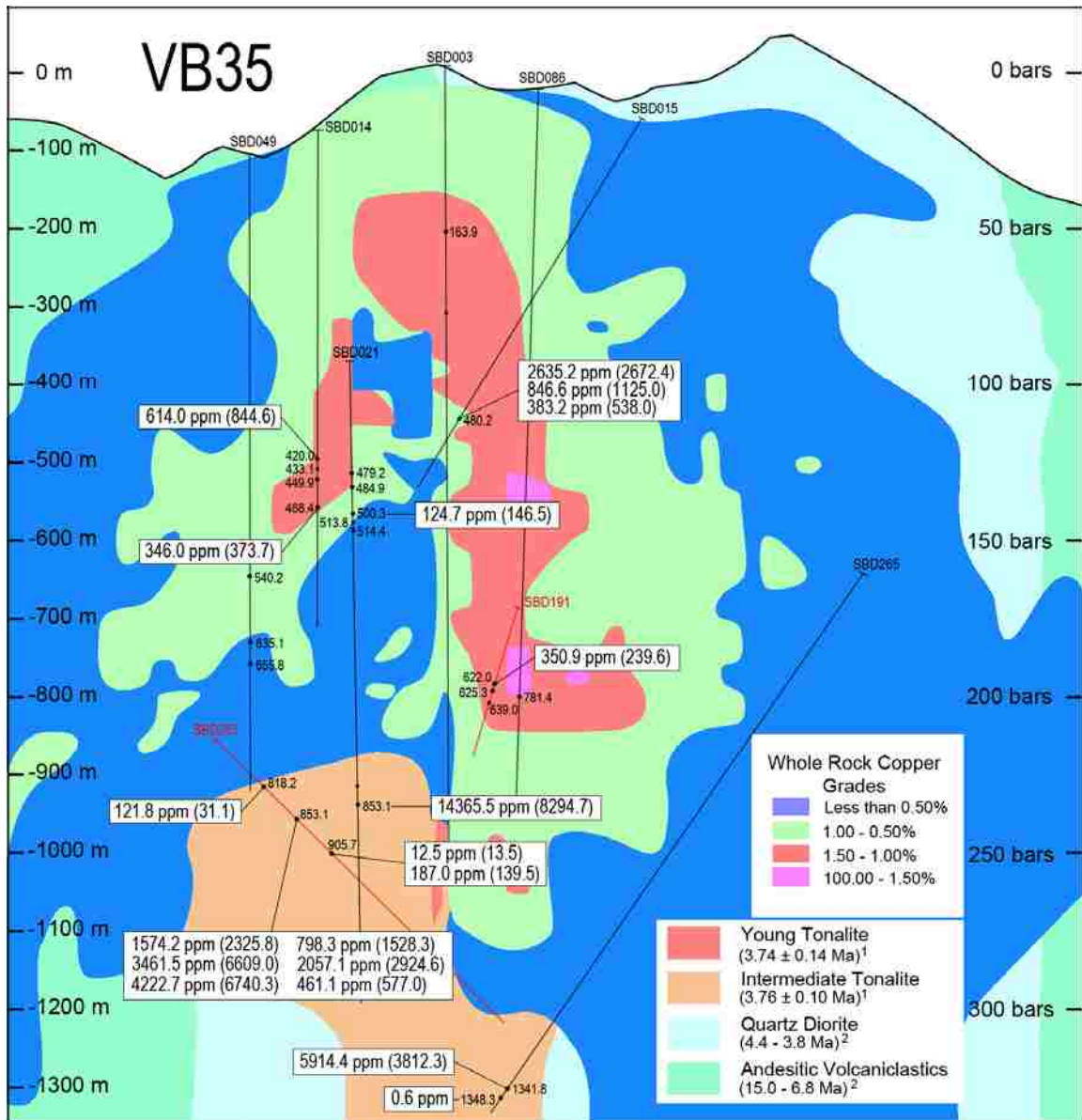
Figure 45 East-West cross section through the Batu Hijau deposit showing whole rock Cu concentrations obtained from assays from mine drill core. Average Cu concentrations obtained from LA-ICP-MS analyses in VB35 FIAs are plotted for given sample locations. (Johan Arif, Personal Communication, 2009).

113
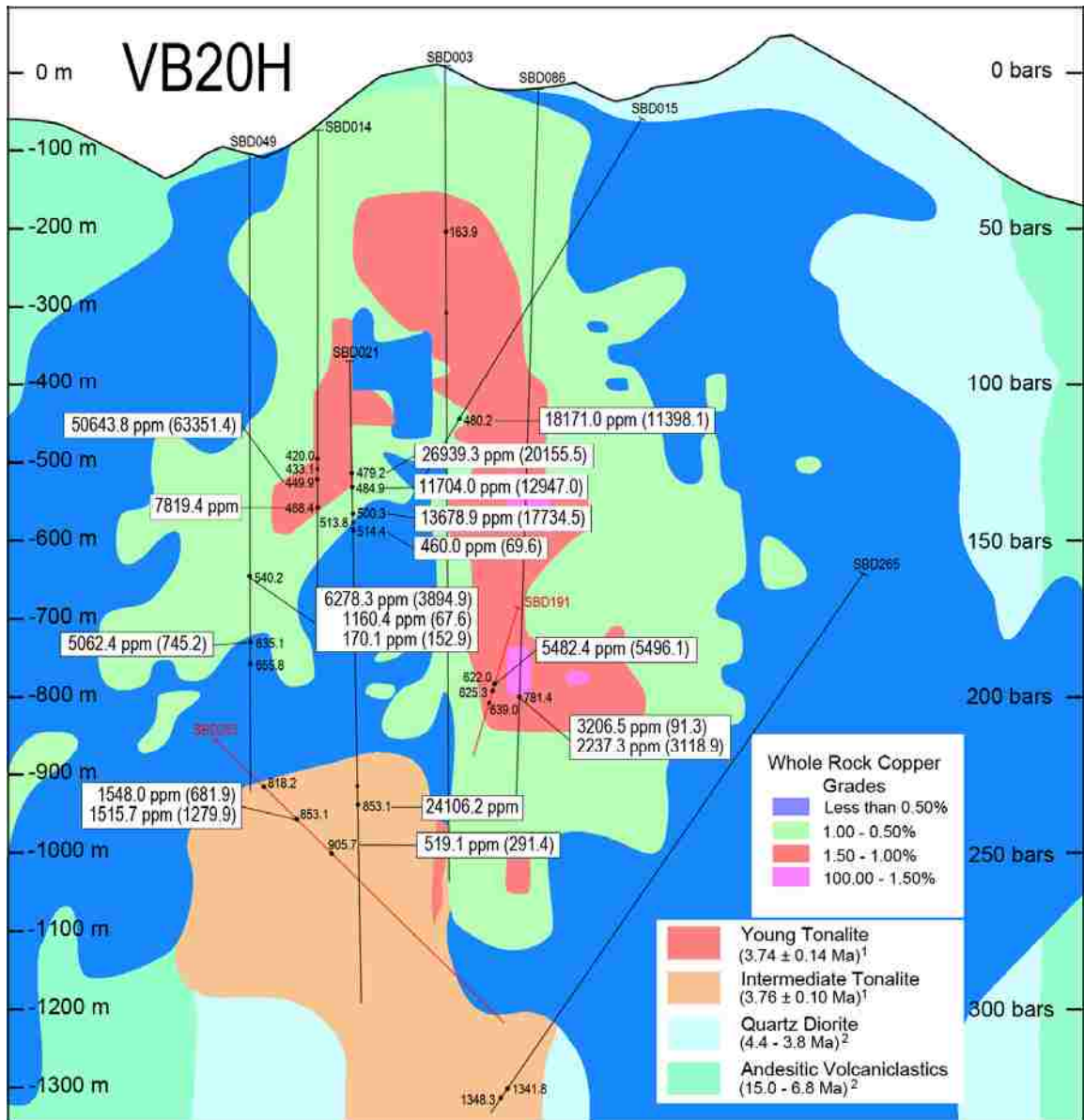
Figure 46 East-West cross section through the Batu Hijau deposit showing whole rock Cu concentrations obtained from assays from mine drill core. Average Cu concentrations obtained from LA-ICP-MS analyses in VB20H FIAs are plotted for given sample locations. (Johan Arif, Personal Communication, 2009).
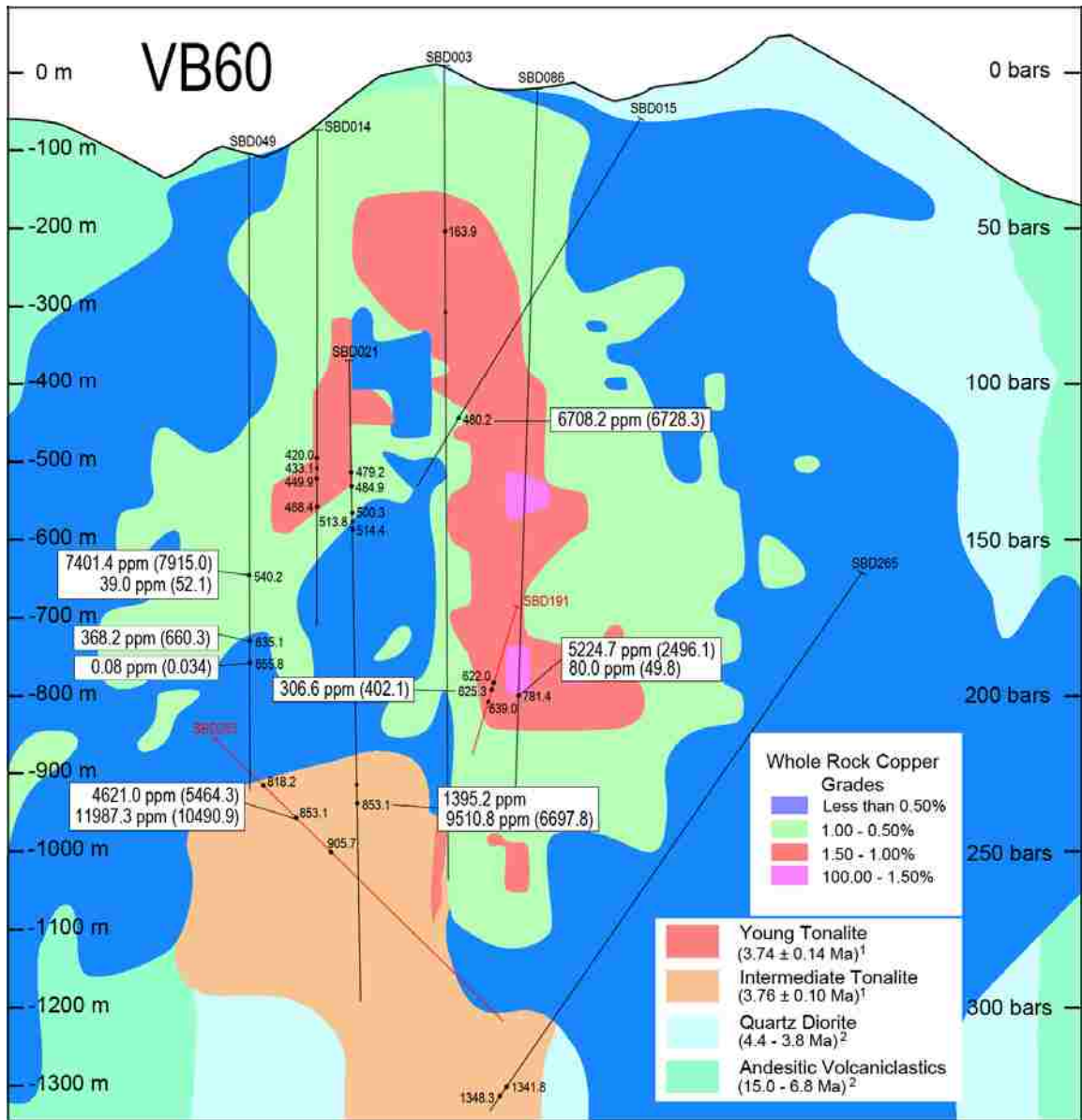
Figure 47 East-West cross section through the Batu Hijau deposit showing whole rock Cu concentrations obtained from assays from mine drill core. Average Cu concentrations obtained from LA-ICP-MS analyses in VB60 FIAs are plotted for given sample locations. (Johan Arif, Personal Communication, 2009).
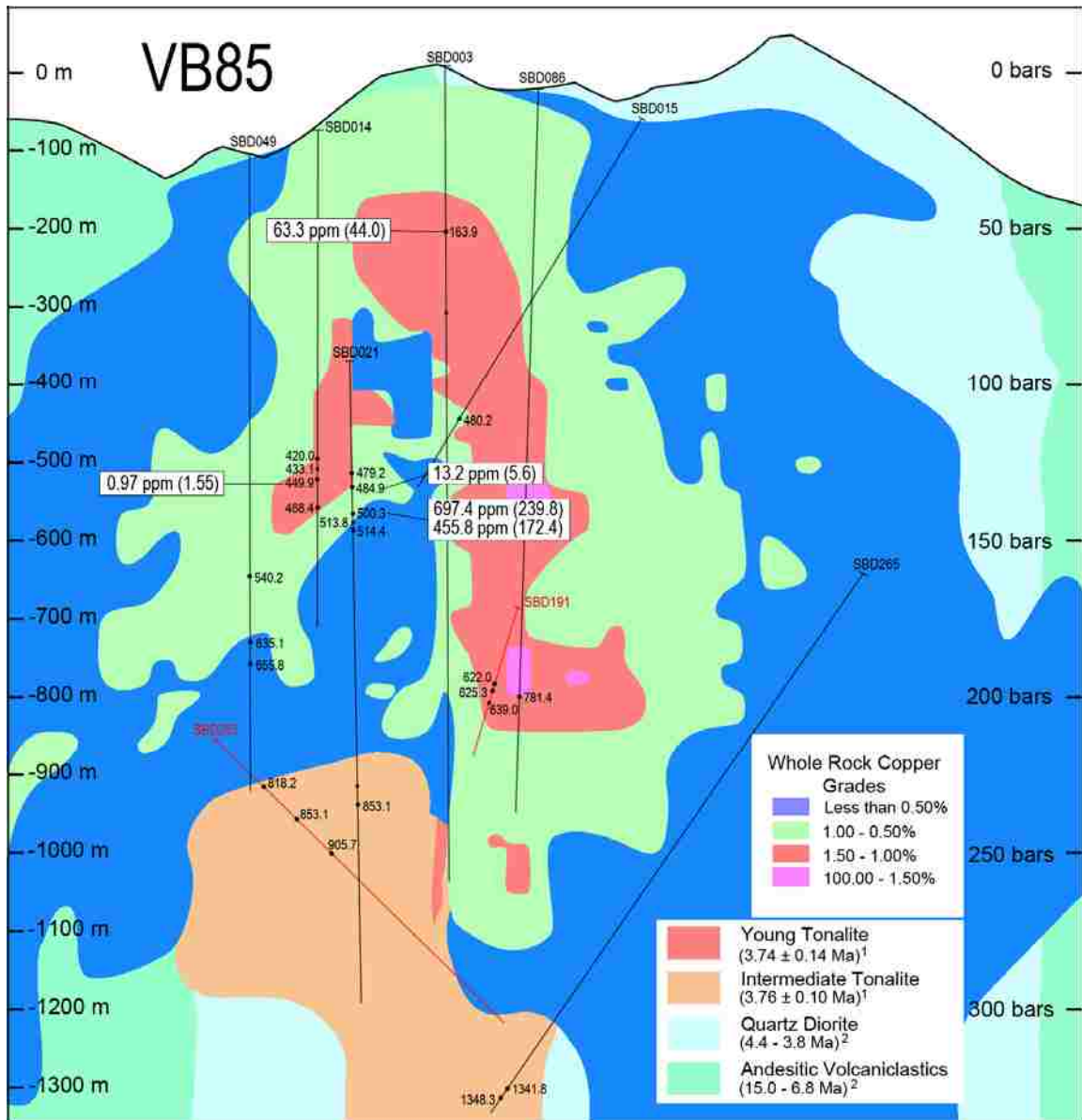
Figure 48 East-West cross section through the Batu Hijau deposit showing whole rock Cu concentrations obtained from assays from mine drill core. Average Cu concentrations obtained from LA-ICP-MS analyses in VB85 FIAs are plotted for given sample locations. (Johan Arif, Personal Communication, 2009).

116
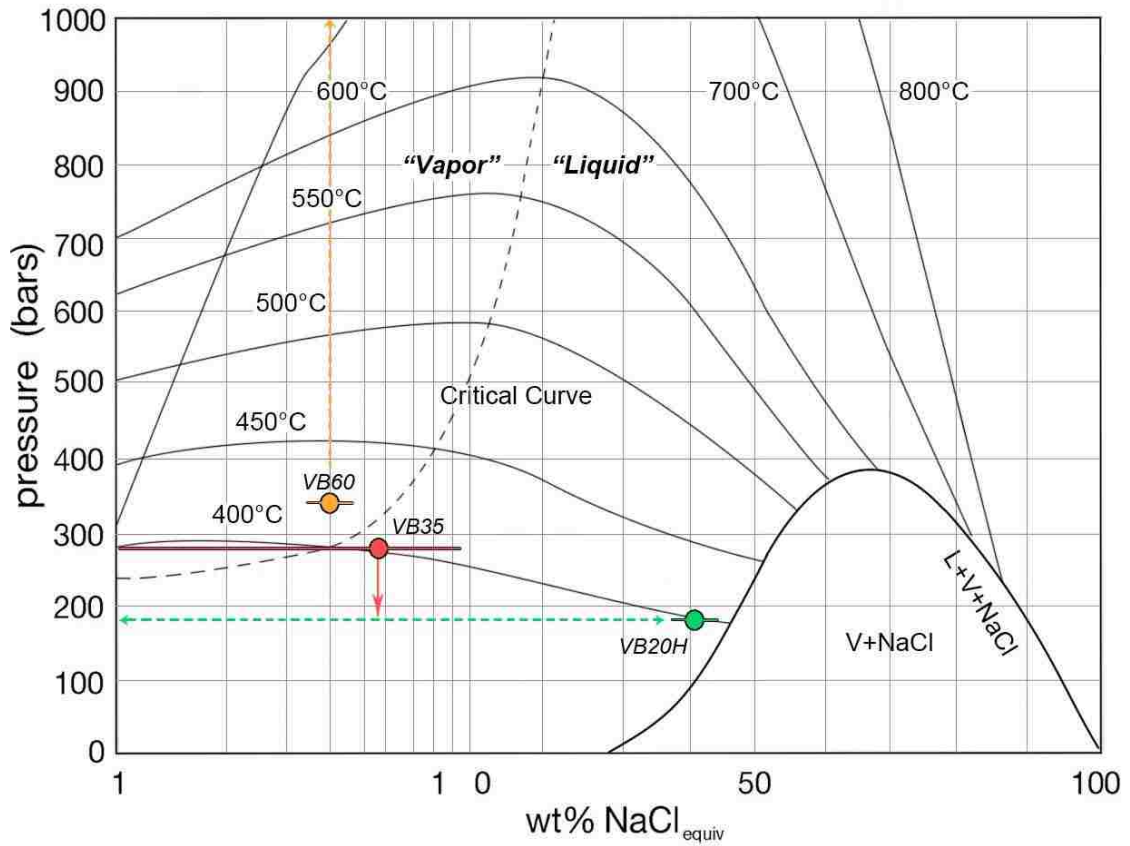
Figure 49 Phase diagram for H$_2$O-NaCl (Sourirajan and Kennedy, 1962; Urusova, 1975; Bodnar et al., 1985; modified from Ulrich et al., 2001), displaying the approximate P-T-Salinity conditions for various fluid inclusion types with color-coded error bars displaying the variability of salinities; VB60 inclusion shown in orange, VB35 inclusions shown in red, and VB20H inclusions shown in green. The green dashed line represents conditions of un-mixing of VB35 fluids to form VB20H and VB85 fluids. VB85 inclusions plot at salinities outside of currently available experimental data and are not shown on this figure.

117

Appendix 1 Microthermometric Data

Drill Hole #	Footage	FIA #	Incl. Type	Incl. #	Ice Melting Temp (°C)	HH Melting Temp (°C)	Halite Melting (°C)	Homog. to Liquid (°C)	Homog. to Vapor (°C)	Salinity (wt% NaCl equiv.)
SBD21	500.3	FIA051	VB20H	1			426.4	354		50.42
				2			393.6	378.6		46.75
				3			401.9	357.1		47.65
				4			353.2	335.2		42.70
		FIA053	VB85	1	-21.1				368	23.11
				2					345	
				3					345	
				4					ND	
				5					ND	
				6					345	
		FIA054	VB85	1						
				2						
				3						
				4						
				5						
				6						
				7						
				8						
				9			291.1	352.9		37.49
				10			296	377.4		37.86
		FIA055	VB35	1	-0.1			293.5		0.18
				2	-0.1			293.5		0.18
				3	-0.4			276.4		0.71
				4	-0.2			290.1		0.35
				5	-0.2			291.1		0.35
SBD03	214.6	FIA041	VB85	1					>400	
				2					>400	
			VB20H	3			DNM	309		
				4			DNM	300		

Appendix 1 Microthermometric Data

Drill Hole #	Footage	FIA #	Incl. Type	Incl. #	Ice Melting Temp (°C)	HH Melting Temp (°C)	Halite Melting (°C)	Homog. to Liquid (°C)	Homog. to Vapor (°C)	Salinity (wt% NaCl equiv.)
SBD03	214.6	FIA041	VB20H	5			DNM	299		
				6			DNM	296.5		
SDB257	905.7	FIA061	VB35	1	-0.1			232.2		0.18
				2	-0.1			232.2		0.18
				3	-0.1			232.2		0.18
				4	-0.1			232.2		0.18
				20+	-0.1			232.2		0.18
		FIA062	VB35	1	-1.7			379		2.90
				2	0			257.3		0.00
				3	-1.6			378.2		2.74
				4	-1.3			381.1		2.24
				5	-1.3			379		2.24
		FIA063	VB35	1	-1.2			257.9		2.07
				2	-1.3			258.5		2.24
				3	-1.5			253.2		2.57
				4	-1.2			260.2		2.24
				5	-1.1			255.6		1.91
		FIA064	VB20H	1			325	337		40.18
				2			330	345		40.61
				3			328	339		40.44
				4			315	299		39.35
				5			320	325		39.76
				6			331	324		40.70
SBD86	781.4	FIA022	VB60	1			358.1		>475	43.16
				2	-3.9				>475	6.30
		FIA023	VB20H	1			178.1	394.5		30.84
				2			180	369		30.92
				3			177	354.4		30.79
				4			179.2	306.1		30.89
				5			DNM	358.4		

Appendix 1 Microthermometric Data

Drill Hole #	Footage	FIA #	Incl. Type	Incl. #	Ice Melting Temp (°C)	HH Melting Temp (°C)	Halite Melting (°C)	Homog. to Liquid (°C)	Homog. to Vapor (°C)	Salinity (wt% NaCl equiv.)
SBD86	781.4	FIA024	VB60	1	-4.1				432.9	6.59
				2	-3.3			408		5.41
				3	-3.8			428.1		6.16
				4	-2.8				386	4.65
				5	-2.9				388	4.80
				6	-4.5			441.5		7.17
		FIA025	VB20H	1			315	317		39.35
				2			314	317		39.27
				3			320	327.4		39.76
				4			322	327.4		39.93
				5			320	322		39.76
				6			310	307		38.95
				7			315.5	316.5		39.39
SBD15	480.2	FIA056	VB35	1	-2.8	-18		324		4.65
				1	-0.3			283		0.53
		FIA057	VB35	2	-0.3			287		0.53
				3	-0.2			289		0.35
				4	-0.1			280		0.18
				5	-0.3			281.2		0.53
				6	-0.6			290.1		1.05
		FIA058	VB35	1	-2.2			300		3.71
				2	-1.1			295.8		1.91
				3	-1.1			297.1		1.91
				4	-1.2			311.8		2.07
		FIA059	VB60	1	-2.2				400-410	3.71
				2	-1.9				395	3.23
				3	-1.1				405-410	1.91
				4	-2				400	3.39
				5	-2.3				388	3.87

Appendix 1 Microthermometric Data

Drill Hole #	Footage	FIA #	Incl. Type	Incl. #	Ice Melting Temp (°C)	HH Melting Temp (°C)	Halite Melting (°C)	Homog. to Liquid (°C)	Homog. to Vapor (°C)	Salinity (wt% NaCl equiv.)
SBD15	480.2	FIA059	VB60	6	-1				399	1.74
		FIA060	VB20H	1			357.4	381		43.10
				2			358	384		43.15
				3			355	365		42.87
				4			354	368		42.78
				5			355	369		42.87
				6			355	362.1		42.87
				7			359	389		43.25
				8			362	402.2		43.54
SBD265	1348.3a	FIA020	VB35	1	0			266.4		0.00
				2	-0.1			268.8		0.18
				3	0			270		0.00
				4	-0.1			267.2		0.18
		FIA021	VB35	1	-0.1			341.9		0.18
				2	-0.2			327		0.35
				3	-0.4			336.4		0.71
				4	0			333.3		0.00
				5	-0.1			311.1		0.18
				6	0.1			322.3		0.18
				7	-0.2			329		0.35
SBD49	655.8a	FIA026	VB60	1			DNM		374.2	
				2			DNM		364	
				3			338.1		420-430	
				4			DNM		410-420	
		FIA027	VB35	1	-0.4			276.9		0.71
				2	-0.3			284.1		0.53
				3	-0.2			288.9		0.35
				4	-0.2			285		0.35
				5	-0.3			287.5		0.53
				6	-0.1			287.3		0.18

Appendix 1 Microthermometric Data

Drill Hole #	Footage	FIA #	Incl. Type	Incl. #	Ice Melting Temp (°C)	HH Melting Temp (°C)	Halite Melting (°C)	Homog. to Liquid (°C)	Homog. to Vapor (°C)	Salinity (wt% NaCl equiv.)
SBD49	635.1	FIA037	VB20H	1			376.2	328.1		44.94
				2			386.7	336.7		46.02
				3			390.1	339		46.38
				4			379.1	313.9		45.24
				5			362	308.5		43.54
				6			387.5	319.1		46.11
		FIA038	VB60	1	-0.5				409.3	0.88
				2	-0.3				360.1	0.53
				3	-0.5				372.2	0.88
				4	-0.6				322.2	1.05
				5	-0.2				351	0.35
			VB20H	6			255.4	310.2		35.02
SBD257	853.1	FIA042	VB35	1	-5	-7.5		415.6		7.86
				2	-5.3	-13.7			>470	8.28
				3	-4.9	-15.8		363.8		7.73
				4	-5.5	-17.6		398.7		8.55
				5	-6.2	-15.5		>470		9.47
				6	-6	-18.9		393		9.21
		FIA043	VB35	1	-2.4	-5.5		309.3		4.03
		FIA050	VB35	1	-1.8			378.9		3.06
				2	-1.7			375.4		2.90
				3	-1.9			379		3.23
				4	-2			377.8		3.39
				5	-1.8			376.4		3.06
				6	-1.9			378.5		3.23
				7	-1.5			378.6		2.57
				8	-1.3			312.8		2.24
		FIA044	VB35	1	-3.4	-20.2		400		5.56
				2	-1.3	-20		376.6		2.24

Appendix 1 Microthermometric Data

Drill Hole #	Footage	FIA #	Incl. Type	Incl. #	Ice Melting Temp (°C)	HH Melting Temp (°C)	Halite Melting (°C)	Homog. to Liquid (°C)	Homog. to Vapor (°C)	Salinity (wt% NaCl equiv.)
SBD257	853.1	FIA044	VB35	3	-3	-20.4		396.6		4.96
				4	-2.8			419.2		4.65
				5	-1.9			401.1		3.23
		FIA045	VB60	1	-5.6	-10			466.5	8.86
				2	-5.5	-10			424	8.55
				3	-4.4				388	7.02
				4	-2.8				395	4.65
				5	-4.8	-10			421	7.59
				6	-2.4	-10			401.2	4.03
				7	-2.9				394	4.80
		FIA046	VB20H	1			341	325.3		41.58
				2			341	319.1		41.58
				3			318	290		39.60
				4			342	327.2		41.67
				5			329.2	308.2		40.54
		FIA047	VB35	1	-1.4	-19.3		366.6		2.41
				2	-1.1	-18.8		382		1.91
				3	-1.9			380.1		3.23
				4	-1.4			378.7		2.41
				5	-1.6			379		2.74
				6	-2			385.6		3.39
				7	-0.9			379.2		1.57
		FIA048	VB35	1	-4.8	-16			456.2	7.59
				2	-5	-18.2			456.5	7.86
				3	-2.5	-17.1			411.1	4.18
				4	-4.1				422	6.59
		FIA049	VB20H	1			340.1	345.4		41.50
				2			309	330		38.87
				3			335	341		41.05
				4			339	328		41.40

Appendix 1 Microthermometric Data

Drill Hole #	Footage	FIA #	Incl. Type	Incl. #	Ice Melting Temp (°C)	HH Melting Temp (°C)	Halite Melting (°C)	Homog. to Liquid (°C)	Homog. to Vapor (°C)	Salinity (wt% NaCl equiv.)
SBD03	163.9	FIA039	VB85	1					353.5	
				2					376.7	
				3					>350	
				4					>360	
SBD49	540.2	FIA028	VB85	1	-1.4				376	2.41
				2	-1.3				>370	2.24
				3	-1.1				385	1.91
				4	-1.1				>360	1.91
		FIA029	VB20H	1			300	483.4		38.16
				2			304.1	479.5		38.48
				3			295.3	360.9		37.80
		FIA030	VB60	1	-6.9				>415	10.36
				2					>390	
				3			365		>405	43.83
				4					>425	
				5	-6.1				>440	9.34
		FIA031	VB60	1	NOI				>410	
				2	NOI				372	
				3	NOI				376	
				4	NOI				387	
		FIA032	VB85	1					319.8	
				2					322	
				3					324.6	
				4						
		FIA033	VB35	1	-9	-23.3		344.4		12.85
				2	-8.6			355.4		12.39
			VB85	3					360	
				4					336.8	
				5					359.8	
		FIA034	VB20H	1			436.7	385.5		51.64

Appendix 1 Microthermometric Data

Drill Hole #	Footage	FIA #	Incl. Type	Incl. #	Ice Melting Temp (°C)	HH Melting Temp (°C)	Halite Melting (°C)	Homog. to Liquid (°C)	Homog. to Vapor (°C)	Salinity (wt% NaCl equiv.)
SBD49	540.2	FIA034	VB20H	2			422.2	372		49.93
				3			391.1	369.6		46.49
				4			365.9	381.2		43.92
		FIA036	VB35	1	-1.7			252		2.90
				2	-1.6			252		2.74
				3	-1.6			254		2.74
				4	-1.8			256		3.06
				5	-1.7			266		2.90
				6	-1.6			273		2.74
				7	-1.5			271		2.57
				8	-1.6			260		2.74
SBD21	482.8	FIA001	VB85	1					>350	
				2					>355	
				3					>340	
			VB20H	4			406.8	304.2		48.19
				5			392.1	309.2		46.59
				6			388.4	328.1		46.20
SBD21	853.1	FIA002	VB35	1		-20.6	83.5	381.4		27.54
				2		-20.2	74.4	385.9		27.32
				3		-19.5	82.1	389.4		27.50
				4		-20.5	138.2	372.6		29.22
				5		-18.5	130.4	367.6		28.94
		FIA003	VB60	1	-0.5				378.9	0.88
				2	-0.3				384.3	0.53
				3	-0.5				387.5	0.88
				4	-0.6				389.9	1.05
				5	-0.2				320.2	0.35
		FIA066	VB60	1	-2.4				376.5	4.03
				2	-2.2				389.4	3.71
				3	-2.3				384.5	3.87

Appendix 1 Microthermometric Data

Drill Hole #	Footage	FIA #	Incl. Type	Incl. #	Ice Melting Temp (°C)	HH Melting Temp (°C)	Halite Melting (°C)	Homog. to Liquid (°C)	Homog. to Vapor (°C)	Salinity (wt% NaCl equiv.)
SBD21	853.1	FIA066	VB60	4	-2				383.9	3.39
		FIA067	VB35	1	-2.3			376.4		3.87
				2	-2.1			380.9		3.55
				3	-2			374		3.39
				4	-1.1			375.5		1.91
				5	-0.9			374.5		1.57
				6	-1.3			378.1		2.24
				7	-1.4			371.1		2.41
				8	-1.6			382.3		2.74
				9	-2.2			389.4		3.71
				10	-2.6			378.9		4.34
				11	-1.8			372.2		3.06
SBD14	449.9	FIA004	VB20H	1			429.5	356.6		50.78
				2			434.5	366		51.38
				3			432.2	369.1		51.10
				4			448.1	372.1		53.03
				5			437.9	376.6		51.78
				6			456.6	370.3		54.08
				7			442.2	359.1		52.30
		FIA005	VB60/VB85	1					>420	
				2					>440	
				3					>450	
				4					>450	
				5					>430	
			VB20H	6			444.3	399.9		52.56
				7			410	334.9		48.54
				8			418.2	294.4		49.47
				9			438.2	392		51.82
				10			448.9	345.5		53.12

Appendix 1 Microthermometric Data

Drill Hole #	Footage	FIA #	Incl. Type	Incl. #	Ice Melting Temp (°C)	HH Melting Temp (°C)	Halite Melting (°C)	Homog. to Liquid (°C)	Homog. to Vapor (°C)	Salinity (wt% NaCl equiv.)
SBD14	449.9	FIA006	VB85	2					>340-350	
				3					>340-350	
				4					>340-350	
			VB20H	1			329.1	337.9		40.53
				2			370.6	328.1		44.38
				3			367.2	323.4		44.04
				4			354.4	313.2		42.81
SBD21	484.9	FIA007	VB35	1	-0.4			292.3		0.71
				2	-0.4			294.4		0.71
				3	-0.4			294.7		0.71
				4	-0.4			319.2		0.71
				5	-0.4			315.5		0.71
				6	-0.5			304.6		0.88
				7	-0.3			308.7		0.53
				8	-0.6			313.4		1.05
		FIA008	VB85	1					>365	
				2					>350	
				3					>370	
				4					>400	
			VB20H	1			329.2	378		40.54
				2			338.4	379.9		41.35
		FIA011	VB20H	1			431.7	337.8		51.04
				2			286.5	324.6		37.15
				3			440.1	330.2		52.05
				4			405.8	320.9		48.08
				5			376.4	317.8		44.96
				6			422.3	305.8		49.94
SBD14	433.1	FIA013	VB35	1	-2.1			298.6		3.55
				2	-1.9			284.5		1.57
				3	-1.9			270.8		1.57

Appendix 1 Microthermometric Data

Drill Hole #	Footage	FIA #	Incl. Type	Incl. #	Ice Melting Temp (°C)	HH Melting Temp (°C)	Halite Melting (°C)	Homog. to Liquid (°C)	Homog. to Vapor (°C)	Salinity (wt% NaCl equiv.)
SBD14	433.1	FIA013	VB35	4	-2			296.5		3.39
				5	-2			281.4		3.39
SBD21	479.2	FIA016	VB20H	1			445	362.2		52.65
				2			444.3	353.3		52.56
				3			441.1	386.7		52.17
				4			443.5	375		52.46
				5				360.8		
				6			442.9	375.9		52.39
		FIA017	VB20H	1			380.3	367.6		45.36
				2			381.2	390		45.45
				3			384.4	389.6		45.78
				4			381.1	385.8		45.44
				5			380.9	386.7		45.42
				6			382	379.4		45.53
SBD21	514.4	BH061	VB20H				301.1	429.4		38.25
		BH062	VB20H				298.8	441		38.07
		BH063	VB20H				303.1	442.7		38.40
		BH064	VB20H				370.3	410.5		44.35
SBD265	1341.8	BH001	VB35		-2.7			370		4.49
		BH002	VB35		-3.2	-22		383		5.26
		BH003	VB35		-5.4	-22		383.6		8.41

ND = Not determined   **HH = Hydro halite**

DNM = Did not measure   **NOI = No observable ice**

Appendix 2.1 VB35 LA-ICP-MS Data

Hole	Depth	FIA #	Incl. #	Sal*	Sal 2**	ppm B	ppm Na	ppm K	ppm Ca	ppm Mn
SBD21	500.3	FIA055	1	0.20	0.15		338.07	77.68	41.53	
			2	0.20	0.17		269.39	146.20	28.86	
SDB257	905.7	FIA062	2	2.74	0.30		234.28	463.78	190.53	
			3	2.74	0.17		222.08	0.00	-	
		FIA063	1	2.10	1.98		6477.32	1453.60	335.23	
			2	2.57	2.12		7221.62	1082.47	291.66	
			3	2.20	0.40		1010.64	159.41	6571.66	
SBD15	480.2	FIA056	1	0.40	0.34		831.08	265.71	35.76	
			2	0.40	0.34		750.46	479.25	29.22	
			3	2.20	1.79		2052.25	0.00	-	
			4	2.20	1.86		3144.05	0.00	380.80	
			5	2.20	1.75		1957.34	0.00	257.28	
		FIA057	1	0.50	0.53		2080.19	0.00		
			2	0.50	0.53		2082.73	0.00		
			3	0.50	0.51		1745.27	0.00		
			4	0.50	0.52		2055.68	0.00		
			6	0.50	0.53		2023.70	0.00		
			7	0.50	0.52		1946.54	0.00		
			8	0.40	0.30		550.75	0.00		
			9	0.40	0.28		223.33	0.00		
		FIA058	1	3.40	3.26		11274.91	0.00		
			3	3.40	3.40		13286.94	0.00		
			4	2.10	2.07		8014.68	0.00		
			5	2.10	2.04		7528.17	0.00		
SBD265	1348.3	FIA021	2	0.35	0.00	0.02	0.67	0.18	-	0.04
SBD257	853.1	FIA042	1	7.90	7.87		30605.19	0.00		
			2	8.30	8.30		32520.68	0.00		
			3	7.70	7.75		30300.86	0.00		
			4	8.50	8.26		28896.08	0.00		

* Salinity determined by microthermometry; ** Salinity calculated from LA-ICP-MS data

Appendix 2.1 VB35 LA-ICP-MS Data

Hole	Depth	FIA #	Incl. #	Sal*	Sal 2**	ppm B	ppm Na	ppm K	ppm Ca	ppm Mn
SBD257	853.1	FIA042	5	9.50	9.50		37178.06	0.00		
			6	9.20	9.24		36153.83	0.00		
			7	9.20	7.63		27028.71	0.00		
			8	9.20	7.88		30678.02	0.00		
			9	9.20	7.89		30935.29	0.00		
			10	9.20	7.65		27302.74	0.00		
		FIA043	1	4.00	4.03		15808.12	0.00		
			2	4.00	3.10		1847.85	0.00		
			3	4.00	4.03		15639.76	0.00		
			4	4.00	3.89		13674.31	0.00		
			5	4.00	4.04		15793.52	0.00		
			6	4.00	4.00		14920.27	0.00		
		FIA044	1	5.56	4.73		15921.74	0.00		
			2	2.24	4.95		19066.72	0.00		
			3	4.96	4.54		13098.81	0.00		
			4	4.45	0.50		1946.08	0.00		
			5	3.32	3.87		3248.11	0.00		
			6	3.09	4.95		19049.49	0.00		
			7	2.24	4.91		18585.16	0.00		
			8	5.56	4.97		19409.06	0.00		
		FIA047	1	2.41	2.04		4347.33	1136.54	977.83	909.48
			2	1.91	2.30		5513.50	723.21	-	855.48
			4	2.41	1.99		4341.00	1302.97	1229.45	793.90
			5	2.74	2.29		5466.61	1058.98	240.62	144.56
		FIA048	1	7.20	5.15		10889.47	4005.87	1964.56	4856.14
			2	7.20	6.31		15211.17	2480.19	-	1469.19
			3	7.20	5.25		1277.03	6016.38	538.54	5439.34
			4	6.60	5.77		17123.79	2719.05	344.13	2096.37
		FIA049	1	0.40	0.31		670.08	0.00		
			3	0.40	0.35		1349.20	0.00		

Appendix 2.1 VB35 LA-ICP-MS Data

Hole	Depth	FIA #	Incl. #	Sal*	Sal 2**	ppm B	ppm Na	ppm K	ppm Ca	ppm Mn
SBD21	853.1	FIA002	1	27.50	26.77		74386.39	37145.51	-	-
			2	27.50	23.03		55796.56	12217.50	8169.92	3068.25
			3	27.50	24.26		59241.22	13058.69	2666.19	3927.17
			4	27.50	22.24		55103.64	11490.99	10632.98	2632.98
SBD265	1341.8	BH002		5.30	4.60		15589.97	0.00	-	1044.56
		BH003		8.50	7.64		22122.54	2616.01	-	1204.68
SBD191	622	BH035		0.40	0.30		509.08	183.50	62.01	106.05
		BH036		0.40	0.32		333.79	118.33	9.33	18.66
SBD14	468.4	BH025		0.40	0.30		533.51	245.59	50.09	131.41
		BH026		0.40	0.31		632.16	154.60	7.74	15.79
SBD14	420.0b	BH021		0.40	0.32		1110.32	155.89	-	24.93
		BH022		0.40	0.27		233.20	39.67	7.11	29.19
SBD257	818.2	BH046		3.70	3.14		10986.00	184.50	221.51	449.16
		BH048		0.20	0.15		324.36	55.58	20.81	46.39

Appendix 2.1 VB35 LA-ICP-MS Data

Hole	Depth	FIA #	Incl. #	Sal*	Sal 2**	ppm Fe	ppm Cu	ppm Zn	ppm As	ppm Rb
SBD21	500.3	FIA055	1	0.2	0.15	74.86	228.35			
			2	0.2	0.17	301.02	21.11			
SDB257	905.7	FIA062	2	2.74	0.30	673.46	2.98			
			3	2.74	0.17	486.66	22.04			
		FIA063	1	2.1	1.98	211.53	40.93			
			2	2.57	2.12	329.65	201.03			
			3	2.2	0.40	290.24	318.94			
SBD15	480.2	FIA056	1	0.4	0.34	226.49	146.48			
			2	0.4	0.34	248.24	36.13			
			3	2.2	1.79	2213.00	4892.93			
			4	2.2	1.86	3100.50	2245.10			
			5	2.2	1.75	1498.78	5855.36			
		FIA057	1	0.53	0.53	0.00	0.00			
			2	0.53	0.53	0.00	0.00			
			3	0.35	0.51	0.00	407.24			
			4	0.18	0.52	0.00	0.00			
			6	1.05	0.53	0.00	73.62			
			7	0.53	0.52	0.00	166.35			
			8	0.4	0.30	0.00	1012.49			
			9	0.4	0.28	0.00	1405.83			
		FIA058	1	3.4	3.26	0.00	2463.17			
			3	1.91	3.40	0.00	0.00			
			4	2.1	2.07	0.00	169.47			
			5	2.1	2.04	0.00	753.76			
SBD265	1348.3	FIA021	2	0.35	0.00	0.41	0.60	0.02	-	-
SBD257	853.1	FIA042	1	7.9	7.87	0.00	396.36			
			2	8.3	8.30	0.00	36.09			
			3	7.7	7.75	0.00	108.54			
			4	8.5	8.26	0.00	5667.33			

Appendix 2.1 VB35 LA-ICP-MS Data

Hole	Depth	FIA #	Incl. #	Sal	Sal 2**	ppm Fe	ppm Cu	ppm Zn	ppm As	ppm Rb
SBD257	853.1	FIA042	5	9.5	9.50	0.00	84.22			
			6	9.2	9.24	0.00	83.43			
			7	9.2	7.63	0.00	4693.68			
			8	9.2	7.88	0.00	309.11			
			9	9.2	7.89	0.00	0.00			
			10	9.2	7.65	0.00	4363.10			
		FIA043	1	4	4.03	0.00	0.00			
			2	4	3.10	0.00	16802.33			
			3	4	4.03	0.00	232.41			
			4	4	3.89	0.00	2589.71			
			5	4	4.04	0.00	47.68			
			6	4	4.00	0.00	1096.87			
		FIA044	1	5.56	4.73	0.00	4298.86			
			2	2.24	4.95	0.00	518.23			
			3	4.96	4.54	0.00	7690.55			
			4	4.45	0.50	0.00	0.00			
			5	3.32	3.87	0.00	19526.10			
			6	3.09	4.95	0.00	540.32			
			7	2.24	4.91	0.00	1098.79			
			8	5.56	4.97	0.00	108.91			
		FIA047	1	2.41	2.04	3146.99	11.18	217.66		3.80
			2	1.91	2.30	3265.16	70.08	265.51		-
			4	2.41	1.99	2780.61	21.46	239.84		4.59
			5	2.74	2.29	922.46	3090.42	72.99		-
		FIA048	1	7.2	5.15	7084.41	0.00	1627.93		-
			2	7.2	6.31	4268.72	6323.40	639.12		-
			3	7.2	5.25	16403.52	325.17	2312.03		-
			4	6.6	5.77	2792.46	1579.86	809.65		5.32
		FIA049	1	0.4	0.31	0.00	869.13			
			3	0.4	0.35	0.00	53.17			

Appendix 2.1 VB35 LA-ICP-MS Data

Hole	Depth	FIA #	Incl. #	Sal*	Sal 2**	ppm Fe	ppm Cu	ppm Zn	ppm As	ppm Rb
SBD21	853.1	FIA002	1	27.5	26.77	1521.09	2275.30	-		-
			2	27.5	23.03	17453.88	16066.63	3054.18		-
			3	27.5	24.26	16789.94	18261.85	2758.37		-
			4	27.5	22.24	12068.52	20858.34	2748.40		-
SBD265	1341.8	BH002		5.3	4.60	533.07	3218.73	679.33		-
		BH003		8.5	7.64	676.08	8610.08	743.86		-
SBD191	622	BH035		0.4	0.30	453.50	181.47	20.70		-
		BH036		0.4	0.32	560.96	520.27	10.30		0.32
SBD14	468.4	BH025		0.4	0.30	438.54	81.75	45.35		0.40
		BH026		0.4	0.31	114.13	610.23	13.41		0.40
SBD14	420.0b	BH021		0.4	0.32	17.52	16.73	120.57		-
		BH022		0.4	0.27	83.06	1211.21	16.79		-
SBD257	818.2	BH046		3.7	3.14	1238.96	143.78	377.41		-
		BH048		0.2	0.15	185.82	99.84	20.76		-

Appendix 2.1 VB35 LA-ICP-MS Data

Hole	Depth	FIA #	Incl. #	Sal*	Sal 2**	ppm Sr	ppm Mo	ppm Ag	ppm Ba
SBD21	500.3	FIA055	1	0.2	0.15				
			2	0.2	0.17				
SDB257	905.7	FIA062	2	2.74	0.30				
			3	2.74	0.17				
		FIA063	1	2.1	1.98				
			2	2.57	2.12				
			3	2.2	0.40				
SBD15	480.2	FIA056	1	0.4	0.34				
			2	0.4	0.34				
			3	2.2	1.79				
			4	2.2	1.86				
			5	2.2	1.75				
		FIA057	1	0.53	0.53				
			2	0.53	0.53				
			3	0.35	0.51				
			4	0.18	0.52				
			6	1.05	0.53				
			7	0.53	0.52				
			8	0.4	0.30				
			9	0.4	0.28				
		FIA058	1	3.4	3.26				
			3	1.91	3.40				
			4	2.1	2.07				
			5	2.1	2.04				
SBD265	1348.3	FIA021	2	0.35	0.00	-	0.00	-	0.00
SBD257	853.1	FIA042	1	7.9	7.87				
			2	8.3	8.30				
			3	7.7	7.75				
			4	8.5	8.26				

Appendix 2.1 VB35 LA-ICP-MS Data

Hole	Depth	FIA #	Incl. #	Sal*	Sal 2**	ppm Sr	ppm Mo	ppm Ag	ppm Ba
SBD257	853.1	FIA042	5	9.5	9.50				
			6	9.2	9.24				
			7	9.2	7.63				
			8	9.2	7.88				
			9	9.2	7.89				
			10	9.2	7.65				
		FIA043	1	4	4.03				
			2	4	3.10				
			3	4	4.03				
			4	4	3.89				
			5	4	4.04				
			6	4	4.00				
		FIA044	1	5.56	4.73				
			2	2.24	4.95				
			3	4.96	4.54				
			4	4.45	0.50				
			5	3.32	3.87				
			6	3.09	4.95				
			7	2.24	4.91				
			8	5.56	4.97				
		FIA047	1	2.41	2.04	15.36			30.69
			2	1.91	2.30	5.20			14.99
			4	2.41	1.99	20.64			37.14
			5	2.74	2.29	5.99			5.51
		FIA048	1	7.2	5.15	18.39			60.96
			2	7.2	6.31	-			16.96
			3	7.2	5.25	8.58			8.04
			4	6.6	5.77	5.28			22.69
		FIA049	1	0.4	0.31				
			3	0.4	0.35				

Appendix 2.1 VB35 LA-ICP-MS Data

Hole	Depth	FIA #	Incl. #	Sal*	Sal 2**	ppm Sr	ppm Mo	ppm Ag	ppm Ba
SBD21	853.1	FIA002	1	27.5	26.77	-			-
			2	27.5	23.03	114.52			114.47
			3	27.5	24.26	36.13			116.31
			4	27.5	22.24	142.50			112.48
SBD265	1341.8	BH002		5.3	4.60	-			-
		BH003		8.5	7.64	-			-
SBD191	622	BH035		0.4	0.30	1.21			12.96
		BH036		0.4	0.32	0.18			1.98
SBD14	468.4	BH025		0.4	0.30	0.98			6.29
		BH026		0.4	0.31	0.16			1.28
SBD14	420.0b	BH021		0.4	0.32	-			-
		BH022		0.4	0.27	-			0.12
SBD257	818.2	BH046		3.7	3.14	3.37			25.38
		BH048		0.2	0.15	0.31			1.97

Appendix 2.1 VB35 LA-ICP-MS Data

Hole	Depth	FIA #	Incl. #	Sal*	Sal 2**	ppm W	ppm Au	ppm Pb
SBD21	500.3	FIA055	1	0.2	0.15		-	
			2	0.2	0.17		-	
SDB257	905.7	FIA062	2	2.74	0.30		-	
			3	2.74	0.17		-	
		FIA063	1	2.1	1.98		-	
			2	2.57	2.12		-	
			3	2.2	0.40		-	
SBD15	480.2	FIA056	1	0.4	0.34		-	
			2	0.4	0.34		-	
			3	2.2	1.79		-	
			4	2.2	1.86		-	
			5	2.2	1.75		-	
		FIA057	1	0.53	0.53		-	
			2	0.53	0.53		-	
			3	0.35	0.51		-	
			4	0.18	0.52		-	
			6	1.05	0.53		-	
			7	0.53	0.52		-	
			8	0.4	0.30		-	
			9	0.4	0.28		-	
		FIA058	1	3.4	3.26		1.14	
			3	1.91	3.40		-	
			4	2.1	2.07		-	
			5	2.1	2.04		-	
SBD265	1348.3	FIA021	2	0.35	0.00	-		0.00
SBD257	853.1	FIA042	1	7.9	7.87		-	
			2	8.3	8.30		-	
			3	7.7	7.75		-	
			4	8.5	8.26		-	

138

Appendix 2.1 VB35 LA-ICP-MS Data

Hole	Depth	FIA #	Incl. #	Sal*	Sal 2**	ppm W	ppm Au	ppm Pb
SBD257	853.1	FIA042	5	9.5	9.50			-
			6	9.2	9.24			-
			7	9.2	7.63			-
			8	9.2	7.88			-
			9	9.2	7.89			-
			10	9.2	7.65			-
		FIA043	1	4	4.03			-
			2	4	3.10			-
			3	4	4.03			-
			4	4	3.89			-
			5	4	4.04			-
			6	4	4.00			-
		FIA044	1	5.56	4.73			-
			2	2.24	4.95			-
			3	4.96	4.54			-
			4	4.45	0.50			-
			5	3.32	3.87			-
			6	3.09	4.95			-
			7	2.24	4.91			-
			8	5.56	4.97			-
		FIA047	1	2.41	2.04			10.87
			2	1.91	2.30			19.29
			4	2.41	1.99			18.20
			5	2.74	2.29			-
		FIA048	1	7.2	5.15			19.51
			2	7.2	6.31			65.76
			3	7.2	5.25			145.69
			4	6.6	5.77			29.31
		FIA049	1	0.4	0.31			-
			3	0.4	0.35			-

Appendix 2.1 VB35 LA-ICP-MS Data

Hole	Depth	FIA #	Incl. #	Sal*	Sal 2**	ppm W	ppm Au	ppm Pb
SBD21	853.1	FIA002	1	27.5	26.77		-	-
			2	27.5	23.03		-	158.37
			3	27.5	24.26		-	229.76
			4	27.5	22.24		-	135.21
SBD265	1341.8	BH002		5.3	4.60		-	81.48
		BH003		8.5	7.64		-	120.90
SBD191	622	BH035		0.4	0.30			3.19
		BH036		0.4	0.32			0.26
SBD14	468.4	BH025		0.4	0.30			2.57
		BH026		0.4	0.31			1.53
SBD14	420.0b	BH021		0.4	0.32			1.83
		BH022		0.4	0.27			0.70
SBD257	818.2	BH046		3.7	3.14			34.65
		BH048		0.2	0.15			0.90

Appendix 2.2 VB20H LA-ICP-MS Data

Hole	Depth	FIA #	Incl. #	Sal*	Sal 2**	ppm B	ppm Na	ppm K	ppm Ca	ppm Mn
SBD21	500.3	FIA051	1	55.4	53.19		10347.86	88416.49	8802.59	
			2	54.6	55.28		144708.37	19258.07	1458.17	
			3	56.2	54.73		96485.03	47891.09	3390.12	
			4	55.6	53.02		76542.65	43839.01	2342.54	
			5	55.6	53.50		109673.89	29445.30	1973.30	
SDB257	905.7	FIA064	1	40.4	35.02		76449.10	26993.60	18873.88	
			2	40.2	34.59		70890.08	25605.85	20335.17	
			3	40.2	33.22		7841.02	52568.70	25937.48	
SBD86	781.4	FIA023	1	30.9	30.18		54588.90	18139.93	1926.60	
			2	30.8	30.22		56154.10	19334.75	2044.79	
			3	30.9	30.15		54322.15	21930.98	2035.01	
		FIA025	1	39.4	37.97		40794.62	40120.53	5029.09	
			2	39.4	38.55		98462.86	19374.03	3178.00	
			3	39.4	36.86		86694.20	20729.11	9130.45	
			4	39.4	37.81		7787.34	62734.34	4018.72	
			5	39.4	35.15		47063.12	37552.95	13676.44	
SBD15	480.2	FIA060	1	43.1	40.24		75534.31	24131.80	4293.08	
			2	43.2	41.45		38427.65	67920.38	5169.56	
			3	42.9	39.59		69046.30	33571.72	7350.19	
			4	42.9	41.86		69575.51	45726.98	1385.80	
SBD49	635.1	FIA037	1	44.9	44.86		173015.04	0.00		
			2	46	45.88		176387.93	0.00		
SBD257	853.1	FIA046	1	41.6	34.14		43393.39	30137.46	3089.65	21124.12
			2	41.5	30.56		6750.62	39624.33	4588.33	29375.78
			3	41.5	31.30		7013.98	43450.50	4310.92	29041.77
			4	41.5	35.38		68455.39	20129.66	3324.39	16954.19
			5	41.5	40.67		140334.16	24045.19	2702.52	-
			6	41.5	39.20		124866.62	18932.18	2666.16	2130.27
			7	40.5	36.98		129470.83	3723.42	2703.21	-

Appendix 2.2 VB20H LA-ICP-MS Data

Hole	Depth	FIA #	Incl. #	Sal*	Sal 2**	ppm B	ppm Na	ppm K	ppm Ca	ppm Mn
SBD257	853.1	FIA049	4	38.9	41.64		162885.14	0.00		
			5	38.9	39.03		152227.40	0.00		
			6	41	41.04		159029.83	0.00		
SBD49	540.2	FIA028	1	2.4	1.88		3904.39	1244.84	1020.89	801.94
			2	2.4	1.93		4207.25	1194.93	906.71	699.07
			3	2.4	1.75		1054.04	2569.68	277.92	1749.96
			4	2.4	1.91		3092.59	2078.48	748.78	958.23
		FIA029	1	38.2	26.39		86048.58	15776.66	55.20	5917.04
			2	38.2	34.77		61922.76	29781.14	684.29	9988.33
			3	38.2	34.38		60111.72	21721.22	827.95	10208.17
		FIA034	1	49.7	44.48		105222.15	21053.64	2832.84	13804.44
			2	49.7	37.97		8820.33	74695.52	3685.50	28832.30
SBD21	853.1	FIA003	4	45.6	43.52		132916.21	10801.24	675.73	1910.23
SBD14	449.9	FIA004	1	50.8	45.00		86428.59	37239.07	2192.13	12843.33
			2	26.8	23.87		50978.88	19119.29	1017.37	6056.58
			3	43.1	43.45		66327.82	11488.75	631.81	4638.38
			4	43.1	42.40		73452.91	26753.64	12791.86	15420.13
SBD21	484.9		2	41	37.94	146.82	63568.66	38609.41	3281.54	6337.09
			3	41	35.02	448.62	18563.38	47717.08	4974.14	7884.37
			4	41	34.86	-	9595.66	68324.55	1669.89	12210.25
SBD21	479.2	FIA016	1	52.6	45.11	63.42	78426.01	45447.69	9763.99	9835.04
			2	52.6	44.88	-	71327.83	38099.09	7785.98	8659.57
			3	52.6	45.39	-	34226.93	0.00	3472.17	6919.48
			4	52.6	45.32	76.00	78453.22	45030.44	8276.69	8943.20
SBD21	514.4	BH061		38.2	35.37		62844.27	26003.16	10511.73	
		BH062		38.1	34.81		63462.45	24310.33	11913.33	
		BH063		38.4	34.41		37415.68	27174.48	14444.53	
SBD191	622	BH033		46.4	40.66		69701.46	38631.05	5079.25	11959.84
		BH034		46.6	41.16		96291.96	22643.15	4509.64	12497.80
SBD14	468.4	BH024		47.4	43.61		15789.43	127263.96	1899.04	7786.34
SBD257	818.2	BH049		46.4	42.53		142647.63	20929.70	9577.87	3137.44

142

Appendix 2.2 VB20H LA-ICP-MS Data

Hole	Depth	FIA #	Incl. #	Sal*	Sal 2**	ppm Fe	ppm Cu	ppm Zn	ppm As	ppm Rb
SBD21	500.3	FIA051	1	50.42	53.19	148286.45	37.03			
			2	46.75	55.28	63656.63	1477.22			
			3	47.65	54.73	91772.34	924.36			
			4	42.7	53.02	86317.04	35759.53			
			5	55.6	53.50	66937.52	30196.49			
SDB257	905.7	FIA064	1	40.4	35.02	45538.23	190.42			
			2	40.2	34.59	50745.72	621.42			
			3	40.2	33.22	92879.74	745.60			
SBD86	781.4	FIA023	1	30.9	30.18	54191.40	3150.67			
			2	30.8	30.22	51517.66	3312.09			
			3	30.9	30.15	51166.53	3157.63			
		FIA025	1	39.4	37.97	87382.04	496.83			
			2	39.4	38.55	42604.06	366.43			
			3	39.4	36.86	46907.76	877.90			
			4	39.4	37.81	99835.60	7737.47			
			5	39.4	35.15	70842.22	1707.81			
SBD15	480.2	FIA060	1	43.1	40.24	50721.17	31161.12			
			2	43.2	41.45	78514.85	5589.42			
			3	42.9	39.59	52409.34	23562.38			
			4	42.9	41.86	59314.53	12370.93			
SBD49	635.1	FIA037	1	44.9	44.86	0.00	4535.46			
			2	46	45.88	0.00	5589.30			
SBD257	853.1	FIA046	1	41.6	34.14	75067.95	1805.60	7133.90		83.62
			2	41.5	30.56	92522.29	1803.95	12641.19		131.11
			3	41.5	31.30	93180.01	539.27	9644.29		126.44
			4	41.5	35.38	60585.29	2043.35	5294.35		52.10
			5	41.5	40.67	1182.83	0.00	-		-
			6	41.5	39.20	5087.00	16468.71	1170.57		-
			7	40.5	36.98	829.53	19493.28	8428.11		-

Appendix 2.2 VB20H LA-ICP-MS Data

Hole	Depth	FIA #	Incl. #	Sal*	Sal 2**	ppm Fe	ppm Cu	ppm Zn	ppm As	ppm Rb
SBD257	853.1	FIA049	4	38.9	41.64	0.00	436.58			
			5	38.9	39.03	0.00	1180.74			
			6	41	41.04	0.00	2929.65			
SBD49	540.2	FIA028	1	2.4	1.88	2700.51	214.57	198.64		4.04
			2	2.4	1.93	2531.89	367.07	172.39		4.11
			3	2.4	1.75	4343.20	60.66	753.31		4.66
			4	2.4	1.91	3144.78	38.29	304.65		8.04
		FIA029	1	38.2	26.39	41.34	9072.32	1963.76		34.94
			2	38.2	34.77	57293.70	1829.18	3718.26		73.61
			3	38.2	34.38	60202.37	7933.34	3575.55		54.00
		FIA034	1	49.7	44.48	59151.79	1208.13	5450.40		53.29
			2	49.7	37.97	93864.26	1112.58	17280.10		225.88
SBD21	853.1	FIA003	4	45.6	43.52	16678.18	24106.15	1214.10		52.60
SBD14	449.9	FIA004	1	50.8	45.00	59567.24	14952.98	6745.82		61.47
			2	51.38	23.87	27256.60	6579.53	3666.69		35.50
			3	51.1	43.45	8607.54	143645.37	1955.03		-
			4	53.03	42.40	56099.94	37397.37	3516.86		-
SBD21	484.9		2	41	37.94	61760.80	2211.33	2004.25	-	165.46
			3	41	35.02	75229.03	26452.42	3220.86	-	188.29
			4	41	34.86	80987.74	6448.12	9807.74	-	188.78
SBD21	479.2	FIA016	1	52.6	45.11	55139.92	25152.81	4911.28	-	135.17
			2	52.6	44.88	52933.27	47516.46	3994.54	-	112.82
			3	52.6	45.39	161505.70	0.00	3561.97	-	-
			4	52.6	45.32	49599.40	35088.01	3884.21	25.59	156.72
SBD21	514.4	BH061		38.2	35.37	63052.22	434.07			
		BH062		38.1	34.81	61316.90	407.10			
		BH063		38.4	34.41	86337.09	538.79			
SBD191	622	BH033		46.4	40.66	61903.57	9368.67	4331.41		106.68
		BH034		46.6	41.16	52968.51	1596.06	4530.49		43.43
SBD14	468.4	BH024		47.4	43.61	62101.50	7819.45	4069.83		765.34
SBD257	818.2	BH049		46.4	42.53	9410.23	0.00	2190.60		94.98

Appendix 2.2 VB20H LA-ICP-MS Data

Hole	Depth	FIA #	Incl. #	Sal*	Sal 2**	ppm Sr	ppm Mo	ppm Ag	ppm Ba
SBD21	500.3	FIA051	1	50.42	53.19				
			2	46.75	55.28				
			3	47.65	54.73				
			4	42.7	53.02				
			5	55.6	53.50				
SDB257	905.7	FIA064	1	40.4	35.02				
			2	40.2	34.59				
			3	40.2	33.22				
SBD86	781.4	FIA023	1	30.9	30.18				
			2	30.8	30.22				
			3	30.9	30.15				
		FIA025	1	39.4	37.97				
			2	39.4	38.55				
			3	39.4	36.86				
			4	39.4	37.81				
			5	39.4	35.15				
SBD15	480.2	FIA060	1	43.1	40.24				
			2	43.2	41.45				
			3	42.9	39.59				
			4	42.9	41.86				
SBD49	635.1	FIA037	1	44.9	44.86				
			2	46	45.88				
SBD257	853.1	FIA046	1	41.6	34.14	99.13			618.04
			2	41.5	30.56	132.55			789.89
			3	41.5	31.30	140.74			907.22
			4	41.5	35.38	89.27			536.96
			5	41.5	40.67	16.05			13.40
			6	41.5	39.20	15.00			-
			7	40.5	36.98	-			-

Appendix 2.2 VB20H LA-ICP-MS Data

Hole	Depth	FIA #	Incl. #	Sal*	Sal 2**	ppm Sr	ppm Mo	ppm Ag	ppm Ba
SBD257	853.1	FIA049	4	38.9	41.64				
			5	38.9	39.03				
			6	41	41.04				
SBD49	540.2	FIA028	1	2.4	1.88	16.59			32.94
			2	2.4	1.93	15.13			29.28
			3	2.4	1.75	6.17			46.46
			4	2.4	1.91	13.31			33.66
		FIA029	1	38.2	26.39	8.45			161.22
			2	38.2	34.77	17.42			224.09
			3	38.2	34.38	14.27			212.35
		FIA034	1	49.7	44.48	43.28			579.06
			2	49.7	37.97	92.96			1338.12
SBD21	853.1	FIA003	4	45.6	43.52	5.71			6.82
SBD14	449.9	FIA004	1	50.8	45.00	31.89			180.86
			2	51.38	23.87	15.70			82.74
			3	51.1	43.45	19.52			47.21
			4	53.03	42.40	184.04			5031.90
SBD21	484.9		2	41	37.94	54.34	-	18.30	329.74
			3	41	35.02	87.68	-	-	559.25
			4	41	34.86	9.85	-	-	70.13
SBD21	479.2	FIA016	1	52.6	45.11	75.98	214.92	28.78	225.08
			2	52.6	44.88	81.71	148.61	25.96	329.85
			3	52.6	45.39	149.55	-	-	246.60
			4	52.6	45.32	82.14	176.17	24.29	346.84
SBD21	514.4	BH061		38.2	35.37				
		BH062		38.1	34.81				
		BH063		38.4	34.41				
SBD191	622	BH033		46.4	40.66	81.17			780.98
		BH034		46.6	41.16	187.14			511.22
SBD14	468.4	BH024		47.4	43.61	61.61			746.74
SBD257	818.2	BH049		46.4	42.53	350.41			304.30

Appendix 2.2 VB20H LA-ICP-MS Data

Hole	Depth	FIA #	Incl. #	Sal*	Sal 2**	ppm W	ppm Au	ppm Pb
SBD21	500.3	FIA051	1	50.42	53.19		-	
			2	46.75	55.28		-	
			3	47.65	54.73		-	
			4	42.7	53.02		-	
			5	55.6	53.50		-	
SDB257	905.7	FIA064	1	40.4	35.02		-	
			2	40.2	34.59		-	
			3	40.2	33.22		-	
SBD86	781.4	FIA023	1	30.9	30.18		-	
			2	30.8	30.22		-	
			3	30.9	30.15		-	
		FIA025	1	39.4	37.97		-	
			2	39.4	38.55		-	
			3	39.4	36.86		-	
			4	39.4	37.81		-	
			5	39.4	35.15		-	
SBD15	480.2	FIA060	1	43.1	40.24		-	
			2	43.2	41.45		-	
			3	42.9	39.59		-	
			4	42.9	41.86		-	
SBD49	635.1	FIA037	1	44.9	44.86		-	
			2	46	45.88		-	
SBD257	853.1	FIA046	1	41.6	34.14		-	582.93
			2	41.5	30.56		-	978.83
			3	41.5	31.30		-	914.74
			4	41.5	35.38		-	407.03
			5	41.5	40.67		-	96.95
			6	41.5	39.20		-	99.10
			7	40.5	36.98		-	-

Appendix 2.2 VB20H LA-ICP-MS Data

Hole	Depth	FIA #	Incl. #	Sal*	Sal 2**	ppm W	ppm Au	ppm Pb
SBD257	853.1	FIA049	4	38.9	41.64		-	
			5	38.9	39.03		-	
			6	41	41.04		-	
SBD49	540.2	FIA028	1	2.4	1.88			16.84
			2	2.4	1.93			16.77
			3	2.4	1.75			49.93
			4	2.4	1.91			26.14
		FIA029	1	38.2	26.39			206.67
			2	38.2	34.77			385.09
			3	38.2	34.38			313.35
		FIA034	1	49.7	44.48			364.94
			2	49.7	37.97			1314.97
SBD21	853.1	FIA003	4	45.6	43.52			122.15
SBD14	449.9	FIA004	1	50.8	45.00		-	680.48
			2	51.38	23.87		-	374.72
			3	51.1	43.45		-	126.34
			4	53.03	42.40		-	384.82
SBD21	484.9		2	41	37.94	32.77		298.88
			3	41	35.02	-		396.86
			4	41	34.86	-		910.91
SBD21	479.2	FIA016	1	52.6	45.11	7.18	-	495.38
			2	52.6	44.88	10.66	-	447.39
			3	52.6	45.39	-	-	352.90
			4	52.6	45.32	12.94	-	635.83
SBD21	514.4	BH061		38.2	35.37		-	
		BH062		38.1	34.81		-	
		BH063		38.4	34.41		-	
SBD191	622	BH033		46.4	40.66			409.62
		BH034		46.6	41.16			298.65
SBD14	468.4	BH024		47.4	43.61			159.29
SBD257	818.2	BH049		46.4	42.53			187.35

Appendix 2.3 VB60 LA-ICP-MS Data

Hole	Depth	FIA #	Incl. #	Sal*	Sal 2**	ppm B	ppm Na	ppm K	ppm Ca	ppm Mn
SBD86	781.4	FIA022	1	6.3	5.98		19742.27	0.00		
			2	6.3	6.07		20993.44	0.00		
			3	6.3	6.20		22929.19	0.00		
			4	6.3	6.14		21987.14	0.00		
			5	6.3	6.00		20031.57	0.00		
			6	6.3	5.79		16972.80	0.00		
			8	6.3	6.32		24697.56	0.00		
			9	6.3	6.32		24665.66	0.00		
		FIA024	1	0.5	0.51		856.33	492.38	55.45	
			2	0.5	0.52		1046.96	424.12	33.44	
			3	0.5	0.51		931.51	337.98	41.27	
SBD15	480.2	FIA059	1	3.71	2.85		1768.40	0.00		
			2	3.23	3.50		11308.74	0.00		
			3	1.91	2.91		2665.19	0.00		
			4	3.39	3.71		14508.08	0.00		
			5	3.87	3.70		14345.33	0.00		
			6	1.74	3.37		9416.53	0.00		
SBD49	655.8a	FIA026	1	0.2	0.00	0.00	2.63	0.04	0.01	0.01
			2	0.2	0.00	0.00	0.32	0.07	0.04	0.04
			3	0.9	0.00	0.06	2.56	0.68	0.13	0.05
SBD49	635.1	FIA038	1	0.88	0.28		264.06	0.00		
			2	0.53	0.36		1389.06	0.00		
			3	0.88	0.35		1315.88	0.00		
			4	0.35	0.35		1378.14	0.00		
SBD257	853.1	FIA045	1	8.7	8.66		33941.80	0.00		
			2	8.55	8.00		23741.19	0.00		
			3	7.02	8.50		31082.96	0.00		
			4	8.71	8.58		32214.71	0.00		

Appendix 2.3 VB60 LA-ICP-MS Data

Hole	Depth	FIA #	Incl. #	Sal*	Sal 2**	ppm B	ppm Na	ppm K	ppm Ca	ppm Mn
SBD49	540.2	FIA030	1	9.2	8.22		20071.51	3770.13	313.67	2645.28
			2	9.2	8.22		17906.52	3901.15	319.11	2242.19
			3	9.2	8.00		17303.00	4419.12	144.68	2594.56
			4	9.2	7.76		820.99	820.01	500.30	678.10
		FIA031	1	0.5	0.28		733.06	0.00	489.43	95.13
			2	0.5	0.32		1079.09	0.00	-	108.70
			3	0.5	0.43		888.44	370.36	92.75	171.15
			4	0.5	0.53		2050.44	12.30	5.92	3.22
SBD21	853.1	FIA003	1	0.9	0.78		755.83	273.91	50.17	-
			3	0.9	0.78		1491.94	782.09	17.63	127.88
		FIA066	1	4.03	3.10		5539.40	556.17	-	733.17
			2	3.7	2.83		807.26	0.00	790.84	-
			3	3.87	2.09		2908.18	760.75	3130.38	352.90
SBD191	625.3	BH040		3.7	2.85		8676.42	2513.45	1978.63	986.52
		BH041		3.7	3.26		9933.77	1727.51	504.94	676.28

Appendix 2.3 VB60 LA-ICP-MS Data

Hole	Depth	FIA #	Incl. #	Sal*	Sal 2**	ppm Fe	ppm Cu	ppm Zn	ppm As	ppm Rb
SBD86	781.4	FIA022	1	6.3	5.98	0.00	6064.92			
			2	6.3	6.07	0.00	4563.58			
			3	6.3	6.20	0.00	2235.74			
			4	6.3	6.14	0.00	3369.37			
			5	6.3	6.00	0.00	5719.69			
			6	6.3	5.79	0.00	9394.77			
			8	6.3	6.32	0.00	113.61			
			9	6.3	6.32	0.00	151.38			
		FIA024	1	6.59	0.51	873.74	22.65			
			2	6.16	0.52	667.64	105.03			
			3	5.41	0.51	852.85	112.45			
SBD15	480.2	FIA059	1	3.71	2.85	0.00	15399.96			
			2	3.23	3.50	0.00	3937.43			
			3	1.91	2.91	0.00	14318.68			
			4	3.39	3.71	0.00	93.47			
			5	3.87	3.70	0.00	289.02			
			6	1.74	3.37	0.00	6210.60			
SBD49	655.8a	FIA026	1	0.2	0.00	0.06	0.10	0.01	-	-
			2	0.2	0.00	0.07	0.05	0.02	-	-
			3	0.9	0.00	0.13	0.00	0.01	-	0.00
SBD49	635.1	FIA038	1	0.88	0.28	0.00	1356.96			
			2	0.53	0.36	0.00	5.29			
			3	0.88	0.35	0.00	92.21			
			4	0.35	0.35	0.00	18.41			
SBD257	853.1	FIA045	1	8.7	8.66	0.00	0.00			
			2	8.55	8.00	0.00	12495.28			
			3	7.02	8.50	0.00	3674.29			
			4	4.65	8.58	0.00	2314.24			

Appendix 2.3 VB60 LA-ICP-MS Data

Hole	Depth	FIA #	Incl. #	Sal*	Sal 2**	ppm Fe	ppm Cu	ppm Zn	ppm As	ppm Rb
SBD49	540.2	FIA030	1	9.2	8.22	9103.17	2004.20	882.21		-
			2	9.2	8.22	10420.87	3444.65	954.82		-
			3	9.2	8.00	8638.93	5028.43	1323.84		-
			4	9.2	7.76	19462.67	19128.46	331.95		-
		FIA031	1	0.5	0.28	336.71	114.35	147.05		-
			2	0.5	0.32	193.31	0.00	351.03		-
			3	0.5	0.43	581.99	32.62	123.02		-
			4	0.5	0.53	2.64	8.99	6.49		-
SBD21	853.1	FIA003	1	0.9	0.78	1382.44	1395.15	52.47		-
			3	0.9	0.78	644.30	696.18	101.27		-
		FIA066	1	4.03	3.10	3338.26	5278.91	422.26		-
			2	3.7	2.83	5167.00	9291.12	459.60		-
			3	3.87	2.09	2249.04	4432.00	2008.86		-
SBD191	625.3	BH040		3.7	2.85	656.09	22.24	363.12		7.89
		BH041		3.7	3.26	1347.27	590.92	548.80		-

Appendix 2.3 VB60 LA-ICP-MS Data

Hole	Depth	FIA #	Incl. #	Sal*	Sal 2**	ppm Sr	ppm Mo	ppm Ag	ppm Ba
SBD86	781.4	FIA022	1	6.3	5.98				
			2	6.3	6.07				
			3	6.3	6.20				
			4	6.3	6.14				
			5	6.3	6.00				
			6	6.3	5.79				
			8	6.3	6.32				
			9	6.3	6.32				
		FIA024	1	6.59	0.51				
			2	6.16	0.52				
			3	5.41	0.51				
SBD15	480.2	FIA059	1	3.71	2.85				
			2	3.23	3.50				
			3	1.91	2.91				
			4	3.39	3.71				
			5	3.87	3.70				
			6	1.74	3.37				
SBD49	655.8a	FIA026	1	0.2	0.00	-	-	-	-
			2	0.2	0.00	-	-	-	0.00
			3	0.9	0.00	0.00	-	-	0.00
SBD49	635.1	FIA038	1	0.88	0.28				
			2	0.53	0.36				
			3	0.88	0.35				
			4	0.35	0.35				
SBD257	853.1	FIA045	1	8.7	8.66				
			2	8.55	8.00				
			3	7.02	8.50				
			4	4.65	8.58				

Appendix 2.3 VB60 LA-ICP-MS Data

Hole	Depth	FIA #	Incl. #	Sal*	Sal 2**	ppm Sr	ppm Mo	ppm Ag	ppm Ba
SBD49	540.2	FIA030	1	9.2	8.22	7.39			46.64
			2	9.2	8.22	5.16			38.65
			3	9.2	8.00	2.88			35.60
			4	9.2	7.76	9.86			10.92
		FIA031	1	0.5	0.28	-			8.01
			2	0.5	0.32	-			19.71
			3	0.5	0.43	2.49			13.89
			4	0.5	0.53	0.05			0.14
SBD21	853.1	FIA003	1	0.9	0.78	0.63			0.66
			3	0.9	0.78	-			1.22
		FIA066	1	4.03	3.10	-			19.66
			2	3.7	2.83	-			37.06
			3	3.87	2.09	17.65			18.62
SBD191	625.3	BH040		3.7	2.85	33.34			56.97
		BH041		3.7	3.26	6.71			14.94

Appendix 2.3 VB60 LA-ICP-MS Data

Hole	Depth	FIA #	Incl. #	Sal*	Sal 2**	ppm W	ppm Au	ppm Pb
SBD86	781.4	FIA022	1	6.3	5.98		-	
			2	6.3	6.07		-	
			3	6.3	6.20		-	
			4	6.3	6.14		-	
			5	6.3	6.00		-	
			6	6.3	5.79		-	
			8	6.3	6.32		-	
			9	6.3	6.32		-	
		FIA024	1	6.59	0.51		-	
			2	6.16	0.52		-	
			3	5.41	0.51		-	
SBD15	480.2	FIA059	1	3.71	2.85		-	
			2	3.23	3.50		-	
			3	1.91	2.91		-	
			4	3.39	3.71		-	
			5	3.87	3.70		-	
			6	1.74	3.37		-	
SBD49	655.8a	FIA026	1	0.2	0.00	-		-
			2	0.2	0.00	-		0.00
			3	0.9	0.00	-		0.00
SBD49	635.1	FIA038	1	0.88	0.28		-	
			2	0.53	0.36		-	
			3	0.88	0.35		-	
			4	0.35	0.35		-	
SBD257	853.1	FIA045	1	8.7	8.66		-	
			2	8.55	8.00		-	
			3	7.02	8.50		-	
			4	4.65	8.58		-	

Appendix 2.3 VB60 LA-ICP-MS Data

Hole	Depth	FIA #	Incl. #	Sal*	Sal 2**	ppm W	ppm Au	ppm Pb
SBD49	540.2	FIA030	1	9.2	8.22			73.84
			2	9.2	8.22			65.14
			3	9.2	8.00			90.11
			4	9.2	7.76			86.97
		FIA031	1	0.5	0.28			16.04
			2	0.5	0.32			24.91
			3	0.5	0.43			7.92
			4	0.5	0.53			1.19
SBD21	853.1	FIA003	1	0.9	0.78			1.68
			3	0.9	0.78			11.33
		FIA066	1	4.03	3.10			28.65
			2	3.7	2.83			-
			3	3.87	2.09			20.22
SBD191	625.3	BH040		3.7	2.85			29.98
		BH041		3.7	3.26			72.83

Appendix 2.4 VB85 LA-ICP-MS Data

Hole	Depth	FIA #	Incl. #	Sal*	Sal 2**	ppm B	ppm Na	ppm K	ppm Ca	ppm Mn
SBD21	500.3	FIA053	1	0.2	0.13		26.03	0.00		
			2	0.2	0.13		37.88	0.00		
			3	0.2	0.13		48.63	0.00		
			4	0.2	0.13		3.91	0.00		
			5	0.2	0.16		473.78	0.00		
		FIA054	1	0.2	0.16		432.93	0.00		
			2	0.2	0.17		513.30	0.00		
			3	0.2	0.15		212.37	0.00		
			4	0.2	0.15		220.04	0.00		
			5	0.2	0.15		216.86	0.00		
SBD03	163.9	FIA039	1	0.2	0.14	-	118.99	378.43	57.72	-
			2	0.2	0.15	2.28	208.15	157.24	157.24	44.63
			4	0.2	0.15	-	305.46	116.60	17.78	35.90
SBD14	449.9	FIA006	1	0.2	0.00	-	0.58	0.13	-	0.05
			2	0.2	0.01	-	12.29	5.82	1.60	1.60
			3	0.2	0.00	-	0.36	0.15	-	0.05
			4	0.2	0.00	-	0.22	0.00	-	0.02
			5	0.2	0.00	-	0.04	0.24	0.01	0.00
			6	0.2	0.00	0.02	0.80	0.21	0.19	0.10
			7	0.2	0.00	0.00	2.88	1.41	0.82	0.49
			8	0.2	0.00	0.01	3.95	2.45	0.17	0.99
SBD21	484.9	FIA008	1	0.4	0.13	-	435.92	86.05	762.94	-
			2	0.4	0.15	-	555.21	40.11	685.42	-
			3	0.4	0.13	-	458.73	64.70	774.45	-
			4	0.4	0.22	-	827.47	29.25	416.36	-
			5	0.4	0.31	31.20	826.92	168.21	-	-
			6	0.4	0.28	9.93	726.45	139.01	78.52	144.99

Appendix 2.4 VB85 LA-ICP-MS Data

Hole	Depth	FIA #	Incl. #	Sal*	Sal 2**	ppm Fe	ppm Cu	ppm Zn	ppm As	ppm Rb
SBD21	500.3	FIA053	1	0.2	0.13	0.00	807.92			
			2	0.2	0.13	0.00	793.68			
			3	0.2	0.13	0.00	780.76			
			4	0.2	0.13	0.00	834.50			
			5	0.2	0.16	0.00	269.95			
		FIA054	1	0.2	0.16	0.00	318.97			
			2	0.2	0.17	0.00	222.46			
			3	0.2	0.15	0.00	584.02			
			4	0.2	0.15	0.00	574.83			
			5	0.2	0.15	0.00	578.64			
SBD03	163.9	FIA039	1	0.2	0.14	156.57	12.75	-	-	-
			2	0.2	0.15	233.25	92.91	29.13	-	0.35
			4	0.2	0.15	179.05	84.38	23.05	-	0.19
SBD14	449.9	FIA006	1	0.2	0.00	0.41	0.33	0.02	-	-
			2	0.2	0.01	7.16	4.62	0.39	-	0.02
			3	0.2	0.00	0.37	0.22	-	-	-
			4	0.2	0.00	0.15	0.31	-	-	-
			5	0.2	0.00	0.09	0.17	-	-	-
			6	0.2	0.00	0.18	0.28	0.02	0.00	0.00
			7	0.2	0.00	2.01	1.61	0.12	-	0.00
			8	0.2	0.00	4.73	0.24	0.37	-	0.01
SBD21	484.9	FIA008	1	0.4	0.13	6.06	7.57	20.81	-	-
			2	0.4	0.15	3.92	14.07	23.88	-	-
			3	0.4	0.13	10.20	10.57	18.77	-	-
			4	0.4	0.22	10.80	20.63	47.27	-	-
			5	0.4	0.31	281.19	0.00	-	-	-
			6	0.4	0.28	289.55	0.00	62.99	-	-

Appendix 2.4 VB85 LA-ICP-MS Data

Hole	Depth	FIA #	Incl. #	Sal*	Sal 2**	ppm Sr	ppm Mo	ppm Ag	ppm Ba
SBD21	500.3	FIA053	1	0.2	0.13				
			2	0.2	0.13				
			3	0.2	0.13				
			4	0.2	0.13				
			5	0.2	0.16				
		FIA054	1	0.2	0.16				
			2	0.2	0.17				
			3	0.2	0.15				
			4	0.2	0.15				
			5	0.2	0.15				
SBD03	163.9	FIA039	1	0.2	0.14	1.00	-	-	2.88
			2	0.2	0.15	0.24	-	-	1.81
			4	0.2	0.15	0.46	0.52	-	2.15
SBD14	449.9	FIA006	1	0.2	0.00	-	0.00	-	0.00
			2	0.2	0.01	0.02	0.07	-	0.13
			3	0.2	0.00	-	-	-	0.00
			4	0.2	0.00	-	-	-	-
			5	0.2	0.00	-	-	-	0.00
			6	0.2	0.00	0.00	0.00	-	0.00
			7	0.2	0.00	0.01	0.02	0.00	0.06
			8	0.2	0.00	0.01	0.01	0.00	0.04
SBD21	484.9	FIA008	1	0.4	0.13	6.91	-	-	1.47
			2	0.4	0.15	7.77	-	-	1.38
			3	0.4	0.13	2.32	-	-	1.99
			4	0.4	0.22	7.81	-	-	0.85
			5	0.4	0.31	0.75	-	-	1.77
			6	0.4	0.28	1.97	-	-	5.48

Appendix 2.4 VB85 LA-ICP-MS Data

Hole	Depth	FIA #	Incl. #	Sal*	Sal 2**	ppm W	ppm Au	ppm Pb
SBD21	500.3	FIA053	1	0.2	0.13		-	
			2	0.2	0.13		-	
			3	0.2	0.13		-	
			4	0.2	0.13		-	
			5	0.2	0.16		-	
		FIA054	1	0.2	0.16		-	
			2	0.2	0.17		-	
			3	0.2	0.15		-	
			4	0.2	0.15		-	
			5	0.2	0.15		-	
SBD03	163.9	FIA039	1	0.2	0.14	-		-
			2	0.2	0.15	0.07		3.21
			4	0.2	0.15	-		1.92
SBD14	449.9	FIA006	1	0.2	0.00	-		0.00
			2	0.2	0.01	0.03		0.08
			3	0.2	0.00	-		-
			4	0.2	0.00	-		-
			5	0.2	0.00	-		-
			6	0.2	0.00	-		0.00
			7	0.2	0.00	0.01		0.01
			8	0.2	0.00	0.00		0.03
SBD21	484.9	FIA008	1	0.4	0.13	-		-
			2	0.4	0.15	-		-
			3	0.4	0.13	-		-
			4	0.4	0.22	-		-
			5	0.4	0.31	-		-
			6	0.4	0.28	-		1.95

REFERENCES

Arif, J., Baker, T. (2004). Gold paragenesis and chemistry at Batu Hijau, Indonesia:

Implications for gold-rich porphyry copper deposits. *Mineralium Deposita*,

39, 523-535.

Barberi, S., Bigioggero, B., Boriani, A., Cattaneo, M., Cavallin, A., Eva, C., Cioni, R.,

Gelemini, R., Giorgetti, F., Iaccarino, S., Innocenti, F., Marinelli, G., Slejko, D.,

and Sudradjat, A. (1987). The island of Sumbawa: a major structural

discontinuity in the Indonesian arc. *Bollettino della Societa Geologica Italiana*,

106, 547-620.

Bodnar, J.R., and Vityk, M.O. (1994). Interpretation of microthermometric data for

H2O-NaCl fluid inclusions. *in* Fluid Inclusions in Minerals: Methods and

Applications, De Vivo, B., and Frezzotti, M.L., eds., pub. by Virginia Technical

Institute, Blacksburg, VA, 117–130.

Bodnar, R.J., Burnham, C.W., and Sterner, S.M. (1985). Synthetic fluid inclusions in

natural quartz. III. Determination of phase equilibrium properties in the

system H2O-NaCl to 1000°C and 1500 bars. *Geochimica et Cosmochimica

Acta*, *49*, 1861–1873.

Burnham, C.W., and Ohmoto, H. (1980). Late-stage processes of felsic magmatism. *Mining Geology,* Special Issue *8*, 1–13.

Clode, C.H., Proffett, J.M., Munajat, I. (1999). Timing relationship of intrusion, wall-rock alteration, and mineralization in the Batu Hijau copper–gold porphyry deposit. *Proceeding Pac-Rim Congress*, 10–13 October 1997, Bali, 485–498

Corbett G.J., Leach T.M. (1998). Southwest Pacific rim gold-copper systems: structure, alteration and mineralization. *Society of Economic Geologists Special Publication*, 6, 236.

Driesner, T. (2007). The system H_2O-NaCl. Part II: Correlation For molar volume, enthalpy, and isobaric heat capacity from 0° to 1000°C, 1 to 5000 bars, and 0 to 1 X_{NaCl}. *Geochimica et Cosmochimica Acta*, *71 (20)*, 4902–4919.

Fletcher, I. R., Garwin, S. L. and McNaughton, N. J. (2000). SHRIMP U-Pb dating of Pliocene zircons. *In* Woodhead,J. D., Hergt, J. M. and Noble, W. P., eds., *Beyond 2000: New Frontiers in Isotope Geoscience.* Lorne, NSW, 2000, Abstracts and Proceedings, 73–74.

Garwin, S.L. (2000). *The setting, geometry and timing of intrusion-related hydrothermal systems in the vicinity of the Batu Hijau porphyry copper-gold deposit, Sumbawa, Indonesia*. (Unpublished doctoral dissertation). University of Western Australia, Perth, Australia.

Garwin, S.L. (2002). The geologic setting of intrusion-related hydrothermal systems near the Batu Hijau porphyry copper-gold deposit, Sumbawa, Indonesia. *Society of Economic Geologists Special Publication*, *9*, 333-366.

Goldstein, R.H., and Reynolds, T.J. (1994). Systematics of fluid inclusions in diagenetic minerals. *Society for Sedimentary Geology Short Course*, *31*, 199.

Hamilton, W. (1979). Tectonics of the Indonesian region. *U.S. Geological Survey Professional Paper*, *1078*, 345.

Heinrich, C.A., Pettke, T., Halter, W.E., Aigner-Torres, M., Audétat, A., Gunther, D., Hattendorf, B., Bleiner, D., Guillong, M., and Horn, I. (2003). Quantitative multi element analysis of minerals, fluid and melt inclusions by laser ablation-inductively coupled plasma-mass spectrometry. *Geochimica et Cosmochimica Acta*, *67*, 3473–3497.

Imai, A., Ohno, S. (2005). Primary ore mineral assemblage and fluid inclusion study of the Batu Hijau porphyry Cu-Au deposit, Sumbawa, Indonesia. *Resource Geology*, *55* (3), 239–248.

Kesler, S.E., Chryssoulis, S.L., and Simon, G. (2002). Gold in porphyry copper deposits: Its abundance and fate. *Ore Geology Reviews*, *21*, 103–124.

Meldrum, S.J., Aquino, R.S., Gonzales, R.I., Burke, R.J., Suyadi, A., Irianto, B. and Clarke, D.S. (1994). The Batu Hijau porphyry copper-gold deposit, Sumbawa Island, Indonesia, *in* van Leeuwen, T.M., Hedenquist, J.W., James, L.P., and Dow, J.A.S., eds., *Mineral deposits in Indonesia, Discoveries of the Past 25 Years. Journal of Geochemical Exploration*, *50*, 203–220.

PT Newmont Nusa Tenggara. (1998). Geological *review of the Batu Hijau porphyry copper-gold deposit, Sumbawa, Indonesia*. Nusa Tenggara Barat, Indonesia: Mitchell P.A., Proffett J.M., Dilles J.H.

Roedder, E. (1984). *Fluid Inclusions*. Mineralogical Society of America, *Reviews in Mineralogy*, Vol. 12, 644 pp.

Rickers, K., Thomas, R., Heinrich, W. (2006). The behavior of trace elements during the chemical evolution of the H2O-, B-, and F-Rich granite–pegmatite–hydrothermal system at Ehrenfriedersdorf, Germany: a SXRF study of melt and fluid inclusions. *Mineralium Deposita*, *41*, 229-245.

Sillitoe, R.H., and Bonham, H.F. (1990). Sediment-hosted gold deposits: distal products of magmatic-hydrothermal systems. *Geology*, *18*, 157–161.

Simon, G., Kesler, S.E., Essense, E.J., and Chryssoulis, S.L. (2000). Gold in porphyry copper deposits: Experimental determination of the distribution of gold in the Cu-Fe-S system at 400° to 700°C. *Economic Geology*, *95*, 259–270.

Sterner, M. (1992). Homogenization of fluid inclusions to the vapor phase: The apparent homogenization phenomenon. *Economic Geology*, *87*, 1616–1623.

Ulrich, T., Günther, D., Heinrich, C.A. (2001). The evolution of a porphyry Cu –Au deposit based on LA-ICP-MS analyses of fluid inclusions: Bajo de la Alumbrera, Argentina. *Economic Geology*, *96*, 1743– 1774.

CV

Graduate College
University of Nevada, Las Vegas

Jordan Armstrong

Local Address:
        927 Sequoia Ruby Ct.
        Henderson, NV 89052

Home Address:
        1312 Deerhurst Dr.
        Raleigh, NC 27614

Degrees:
        Bachelor of Science, Geology, 2008
        Auburn University

        Master of Science, Geoscience, 2012 (Anticipated)
        University of Nevada, Las Vegas

Special Honors and Awards:
        University of Nevada, Las Vegas:
        Bernada E. French Scholarship, 2009
        Eleanor Edwards & Max Olswang Scholarship for Geology, 2009
        UNLV College of Sciences Scholarship, 2009, 2010

        Auburn University:
        Geology Alumni Scholarship, 2008
        College of Science and Mathematics Dean's List, 2007

Grants:
        Society of Economic Geologists/Newmont Mining Corp. Grant, 2009
        Newmont Mining Co. Research Grant, 2009

Organizations:
        Geological Society of America (GSA)
        Society of Economic Geologists (SEG)

Conference Presentations:
        Armstrong, J., Cline, J., Deciphering the Evolution of Ore Fluids at the Batu
        Hijau Copper-Gold Porphyry Deposit, Sumbawa, Indonesia. Poster session
        presented at: Geological Society of America Annual Meeting & Exposition;
        2010 Oct 31 – Nov 3; Denver, CO.

Armstrong, J., Cline, J., Deciphering the Evolution of Ore Fluids at the Batu Hijau Copper-Gold Porphyry Deposit, Sumbawa, Indonesia. Poster session presented at: Pan-American Current Research on Fluid Inclusions (PACROFI X); 2010 Jun 7 – 10; Las Vegas, NV.

Teaching Experience:
    Graduate Teaching Assistant, University of Nevada, Las Vegas, 2009-2011
        Physical Geography, Historical Geology
    Undergraduate Teaching Assistant, Auburn University, 2008
        Historical Geology